

**Electrophoretic deposition of semiconducting polymer metal /
oxide nanocomposites and characterization of the resulting films**

Dissertation

zur Erlangung des akademischen Grades

Doctor rerum naturalium

(Dr. rer. nat.)

vorgelegt

der Fakultät für Mathematik und Naturwissenschaften

der Technischen Universität Dresden

von

M.Sc Vu Quoc Trung

geboren am 11. September 1972 in Hanam – Vietnam

**Gutachter: Prof. Dr. W. Plieth
Prof. Dr. B. Voit
Prof. Dr. S. Nespurek**

Eingereicht: 12.11.2005

Tag der Verteidigung: 13.01.2006

Acknowledgement

Foremost, I would like to thank Prof. Dr. rer. nat. habil. Waldfried Plieth for giving me a good opportunity to study in the world of the conducting polymers and of the semiconductor electrochemistry. He is a strict but very kind teacher. He trains me to become a competent researcher with the independent thinking.

I would like to thank Dr.rer.nat.habil. Ursula Rammelt and Dr. Jiri Pflieger for their valuable discussions and suggestions. They are willing to provide me all supports to undergo this study.

Many words are talked to thank Dr. Niels Hebestreit and Dr. Martin Pavlik for introducing me to conducting polymers and methods for characterization. They teach me how to use the devices in the laboratory and help me to overcome the scientific problems. They are my best friends and collaborators.

I appreciate the help of Mrs. Ellen Kern for SEM, Mrs. I. Poitz for TGA measurements, Dr. C. Bellmann and Mrs. Cascapi for zeta potential measurements, Dipl.-Chem. Andreas Anders for Raman spectra, Dipl.-Phys. A. Lenk for TEM measurements.

My sincere thanks to Dr. rer. nat. habil Andreas Bund, Miss Adriana Ispas and Mr. Ashok Kumar N. for helping me to set up QCM system and for teaching me how it works.

I would like to acknowledge all my members of the work group and of the Institute of Physical Chemistry and Electrochemistry (especially Matthias Intelmann and Dr. Hartmut Dietz). They have given me happiness and pleasure in the last three years. I will remember them forever.

I deeply appreciate all the teachers in the European Graduate School “Advanced polymeric materials” (720), who teach me about the advanced polymeric materials.

This work is financially supported by DFG (Deutsche Forschung Germeinshaft) and the Fonds der chemischen Industrie.

Content

Abbreviation	6
Introduction and aim of the work	8
Part I Theoretical background of conducting polymers and their composites	9
1.1. Intrinsically conducting polymers.....	9
1.1.1 Brief overview	9
1.1.2 Basic properties of conducting polymers.....	10
1.1.2.1 Charge storage and band structure.....	10
1.1.2.2 Charge transport.....	13
1.1.2.3 Stability.....	13
1.1.2.4 Processing possibility.....	14
1.1.2.5 Application.....	15
1.2. Conducting polymer nanocomposites.....	17
1.2.1 Introduction.....	17
1.2.2 Chemical process	17
1.2.2.1 Nanocomposite particles with core-shell structure.....	17
1.2.2.2 Nanocomposite layers prepared by chemical oxidation	19
1.2.3 Electrochemical preparation	20
1.2.3.1 Electropolymerization of conducting polymer on metal oxide layer.....	20
1.2.3.2 Codeposition of conducting polymer and oxide particles.....	21
1.2.4 Physical preparation.....	22
1.2.5 Other processes	24
Part II Theoretical background of electrophoretic deposition (EPD)	25
2.1 Introduction.....	25
2.2 Mechanism of electrophoretic deposition.....	28
2.3 Kinetics of electrophoretic deposition	32
2.4 Application of electrophoretic deposition.....	36
2.4.1 Coatings	36
2.4.2 Fibre reinforced ceramic matrix composites.....	37
2.4.3 Laminated and graded composites.....	37
2.4.4 Nanomaterials and nanostructures	38

Part III Theoretical background of semiconductor electrochemistry	39
3.1 Introduction.....	39
3.2 Fundamentals of semiconductor electrochemistry.....	40
3.2.1 Energy bands in solids and charge carrier generation	40
3.2.2 Fermi level and effect of applied potential	43
3.2.3 Photoeffect at the semiconductor electrolyte interface	45
3.2.4 Determination of flatband potential	48
3.2.4.1 Mott-Schottky plot.....	48
3.2.4.2 Photocurrent onset potential	49
Part IV Experimental procedures	51
4.1 Reagents and solvents	51
4.1.1 Reagents.....	51
4.1.2 Solvents.....	51
4.1.3 Other chemicals	51
4.2 Preparation of nanocomposites	51
4.3 Morphology and chemical structure of nanocomposites	52
4.4 Dark conductivity and thermogrametrical measurements	52
4.5 Properties of suspension	53
4.6 Electrophoretic deposition	53
4.7 Characterization of resulting films.....	55
4.7.1 UV-VIS spectra.....	55
4.7.2 Photocurrent measurements	55
4.7.3 Photoelectrical and electrical characteristics	56
4.7.4 Cyclic voltammetry.....	56
4.7.5 Electrochemical impedance spectroscopy	56
Part V Results and discussion	60
5.1 Morphological and chemical characterization of nanocomposites	60
5.1.1 Morphology of nanocomposite particles	60
5.1.2 Chemical characterization of nanocomposites.....	62
5.2 Electrophoretic deposition	64
5.2.1 Properties of suspension	64
5.2.1.1 Conductivity of suspension.....	64

5.2.1.2 Stability of suspension	64
5.2.2 Electrophoretic deposition	65
5.2.3 Kinetics of electrophoretic deposition	66
5.2.4 Mechanism of electrophoretic deposition	72
5.3 Characterization of PTh/TiO ₂ nanocomposite films prepared by EPD	78
5.3.1 UV-VIS spectra.....	78
5.3.2 Photocurrent measurements	79
5.3.3 Cyclic voltammetry.....	82
5.3.4 Electrochemical impedance spectroscopy	84
5.4 Characterization of PMT/TiO ₂ nanocomposite films prepared by EPD.....	86
5.4.1 Photocurrent measurements	86
5.4.2 Current - voltage curves of solid cells	93
5.4.3 Cyclic voltammetry.....	97
5.4.4 Electrochemical impedance spectroscopy	98
5.5 Characterization of PTh/ZnO nanocomposite films prepared by EPD.....	100
5.5.1 Morphology of composite particles	100
5.5.2 UV-VIS spectra	100
5.5.3 Photocurrent measurements	101
5.5.4 Cyclic voltammetry	102
5.5.5 Electrochemical impedance spectroscopy	103
5.6 Characterization of PTh/Al ₂ O ₃ nanocomposite films prepared by EPD	104
5.6.1 UV-VIS spectra.....	104
5.6.2 Photocurrent measurements	105
5.6.3 Cyclic voltammetry	106
5.6.4 Electrochemical impedance spectroscopy	108
5.7 Electrophoretic deposition of poly (3-octylthiophene).....	108
Conclusion and future work	111
References.....	114

Abbreviation

C:	Concentration
C_{sc}:	Space charge capacitance
CV:	Cyclic voltammetry
D:	Separation of the particles
d₀:	Distance between the electrodes
d_{D(t)}:	Deposit thickness
DLVO:	Derjaguin – Landau – Verwey – Overbeek
E_{fb}:	Flatband potential
EIS:	Electrochemical impedance spectroscopy
EPD:	Electrophoretic deposition
F:	Energy conversion efficiency
FF:	Energy conversion efficiency
H:	Hamaker constant
H-PURET:	Poly (2-(3-thienyl) ethanol hydroxyl carbonyl - methyl urethane)
I₀:	Flux entering the semiconductor
J_p:	Photocurrent density
J_{sc}:	Short circuit current
L:	Diffusion length for minority carriers
MEH-PPV:	Polyphenylenevinylene
N3:	Cis-bis(isothiocyanato)bis(2,2'-bipyridyl-4,4'-dicarboxylato) ruthenium(II) (RuL ₂ (NCS) ₂)
N_D:	Donor density
P3AT:	Poly (3-alkyl) thiophene
P3HT:	Poly (3-hexylthiophene)
P3OT:	Poly (3-octylthiophene)
P3UBT:	Poly (3-undecyl-2,2'-thiophene)
P4UBT:	Poly (4-undecyl-2,2'-bithiophene)
PA:	Polyacetylene
PANI:	Polyaniline
PBT:	Polybithiophene
PEDOT:	Polyethylenedioxythiophene

PITN:	Polyisothianaphtalene
PMT:	Polymethylthiophene
P₀:	Power of incident light
PPP:	Polyparaphenylene
PPV:	Polyparaphenylenevinylene
PPy:	Polypyrrole
PTAA:	Poly (3-thiophene acetic acid)
PTh:	Polythiophene
S:	Surface area
SEM:	Scanning electron microscopy
t:	Time
TBA:	Tetrabutylammonium
TGA:	Thermogravimetric analysis
V_a:	Van der Waals attractive force
W₀:	Initial solid weight in the suspension
W_d:	Width of depletion layer
XRD:	X-ray diffraction
Y:	Yield of deposition
α:	Absorption coefficient
μ:	Electrophoretic mobility

Introduction and aim of the work

Conjugated polymers, showing the property of electrical conductivity, are referred to as conducting polymers. Conducting polymers have significantly different physical and chemical properties. They can be prepared in a neutral state and in an oxidized state. By reduction or oxidation one state can be switched into the other one. The anticipated range of applications is very large (e.g., light emitting diodes, batteries, sensors, photorefractive devices, electro- and photochromic devices and materials, microwave absorbing materials, second and third order nonlinear optical materials and devices, etc.). For the discovery and the development of the field of the conducting polymers, the Nobel Prize for chemistry in 2000 was awarded to A. J. Heeger, A. G. McDiarmid and H. Shirakawa.

Polythiophenes are among the most intensively investigated conjugated polymers that combine the electronic and optical properties of semiconductors with the processing advantages and mechanical plasticity of the conventional polymers. Depending on their oxidation state (doping level), these versatile materials behave either as metallic conductors (oxidized) or as semiconductors (neutral). When doped to metallic level, conjugated polymers become highly conducting and may find applications in batteries, electrochromic or smart windows, electromagnetic shields, antistatic coatings and various types of sensors. On the other hand, when in semiconducting form they exhibit similar electrical and optical properties as inorganic semiconductors. In this state, conjugated polymers can be used as light emitting diodes, field effect transistors and photodetectors or in photovoltaic cells.

Inorganic nanoparticles of different nature and size can be combined with the conducting polymers, giving nanocomposites of core shell structure with interesting physical properties and application potentials. Nanocomposites with core-shell structure based on metal oxide cores and conducting polymer shells are rather easy to prepare even in large quantities.

In this thesis, the electrochemical and photoelectrochemical properties of such nanocomposites have been studied. For these investigations films of nanocomposites were prepared by an electrophoretic deposition process. The deposition process was studied in greater detail and kinetic details were determined. For these investigations for the first time the high voltage electrophoretic deposition process was combined with a quartz microbalance. A mechanism was proposed. Then the films were characterized by various electrochemical and photoelectrochemical methods.

Part I Theoretical background of conducting polymers and their composites

1.1. Intrinsically conducting polymers

1.1.1 Brief overview

Until about thirty years ago all carbon based polymers were rigidly regarded as insulators. The idea that plastics could be made to conduct electricity would have been considered to be absurd. Indeed, plastics have been extensively used by the electric industry because of their insulation property. They were applied as inactive packaging and insulating materials. This narrow view was rapidly changing as a new class of polymers known as intrinsically conducting polymers was discovered. In 1958, polyacetylene was first synthesized by Shirakawa *et al.* as black powder [1, 2]. This was found to be a semiconductor with a conductivity between $7 \cdot 10^{-9}$ - $7 \cdot 10^5$ S.m⁻¹, depending on how the polymer was processed and manipulated. This compound remained a scientific curiosity until 1976, when MacDiarmid, attempted to synthesize polyacetylene, and a silvery thin film was produced as a result of a mistake [2, 3]. It was found that 1000 times too much of the Ziegler-Natta catalyst, Ti(O-*n*-But)₄-Et₃Al, had been used. When the film was investigated it was found to be semiconducting, with a similar level of conductivity as black powders. But, investigations, initially aimed to produce thin films of graphite, showed that exposure of the film to halogens increased its conductivity a billion times. Undoped, the polymer was silvery, insoluble and intractable, with a conductivity similar to that of semiconductors. When it was weakly oxidized by compounds such as iodine it turned into a golden film and its conductivity increased to about 10⁴ Sm⁻¹. In the following years other polymers with similar properties were found. Polyheterocycles were much more air stable than polyacetylene, but their conductivities were not as high as polyacetylene, typically about 10⁵ S.m⁻¹. Fig.1.1 shows the conductivity range of the conducting polymers in comparison with that of other conventional materials [2].

By adding various side groups to the polymer backbone, a variety of derivatives was prepared. Physical, chemical and electrochemical properties were manipulated, leading to different possible applications of these conducting polymers. Fig.1.2 shows some examples of conducting polymers. All have a conjugated structure leading to its special electronic properties.

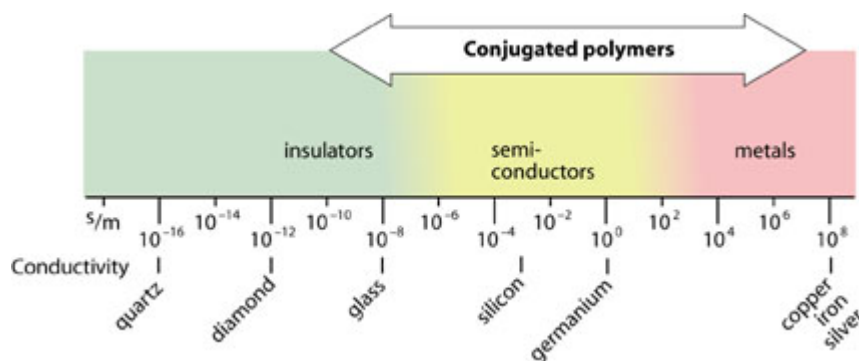


Fig.1.1 Conductivity of conducting polymers in comparison with conventional materials[2]

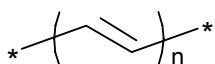
1.1.2 Basic properties of conducting polymers

1.1.2.1 Charge storage and band structure

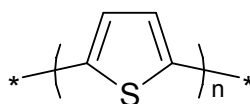
An early explanation of the conduction mechanism is based on the band theory. A half filled valence band would be formed from a continuous delocalised π -system. However, it turns out that the polymer can more efficiently lower its energy by bond alteration with splitting of the band into a filled valence band and an empty conduction band. The polymer is transformed into a conductor by doping with either an electron donor or an electron acceptor. This is similar to the doping of silicon either with arsenic or boron. However, while the doping of silicon produces a donor energy level close to the conduction band or acceptor level close to the valence band, this is not the case for conducting polymers. The evidence for this is low concentration of free spins, as determined by electron spin spectroscopy. Initially the free spin concentration increases with the concentration of the dopant. At larger concentrations, however, the concentration of free spins passes through a maximum value. To understand this it is necessary to examine the way in which charge is stored along the polymer chain and its effect.

The polymer may store charge in two ways. In an oxidation process it could either lose an electron from the valence band or it could localize the charge over a small section of the chain. Localizing the charge causes a local distortion due to a change in geometry, which costs the polymer some energy. However, the generation of this local geometry decreases the ionization energy of the polymer chain and increases its electron affinity making it more able to accommodate the newly formed charges. This method increases the energy of the polymer less than it would if the charge was delocalized and, hence, takes place in preference of charge delocalization. A similar way occurs for a reductive process.

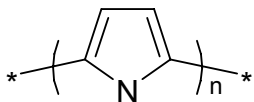
Polyacetylene (PA)



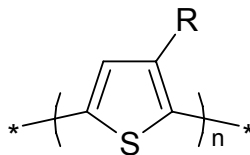
Polythiophene (PTh)



Polypyrrole (PPy)



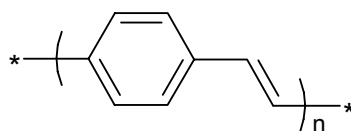
Poly (3-alkyl) thiophene (P3AT)



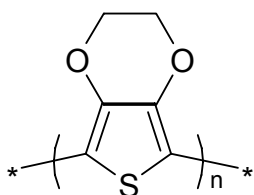
Polyparaphenylene (PPP)



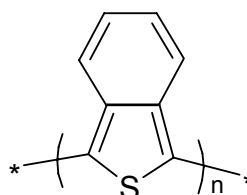
Polyparaphenylenevinylene (PPV)



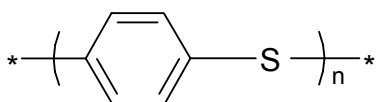
Polyethylenedioxythiophene (PEDOT)



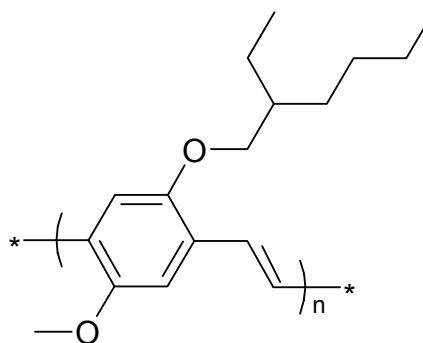
Polyisothianaphtalene (PITN)



Polyparaphenylene sulfide (PPV)



Alkoxy-substituted poly phenylenevinylene (MEH-PPV)



Polyaniline (PANI)

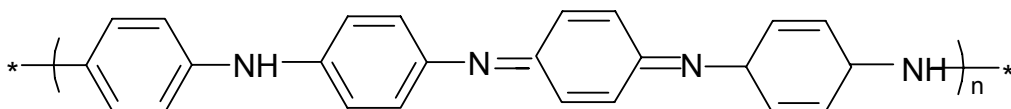


Fig.1.2 Molecular structures of a few conducting polymers [3]

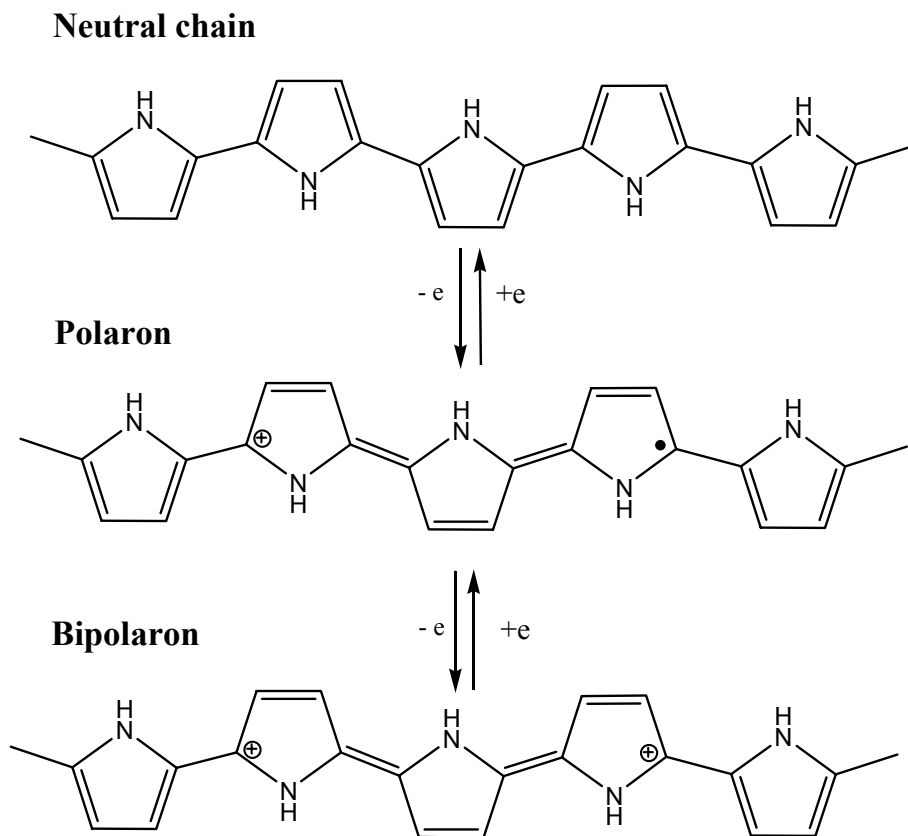


Fig.1.3 Redox scheme of polypyrrole [1]

Typical dopants used are the following anions: AsF_6^- , BF_4^- , ClO_4^- , $\text{CH}_3\text{C}_6\text{H}_4\text{SO}_3^-$, CF_3SO_3^- , PF_6^- , Cl^- , $[-\text{CH}_2-\text{CH}(\text{C}_6\text{H}_4\text{SO}_3^-)-]_n$. The doping of polypyrrole (PPy) proceeds in the following way. An electron is removed from the system of the backbone producing a free radical and a spinless positive charge. The radical and cation are coupled to each other via local resonance of the charge and the radical. A sequence of quinoid-like rings is used to describe the resonance structure of the radical cation. The distortion produced is of higher energy than the remaining portion of the chain. The creation and separation of these defects cost a considerable amount of energy. This limits the number of quinoid-like rings. In the case of PPy it is believed that the lattice distortion extends over four pyrrole rings. This combination of a charge site and a radical is called a polaron. This could be either a radical cation or a radical anion. This creates a new localized electronic state in the gap, with the lower energy state being occupied by a single unpaired electron. The polaron state of PPy is symmetrically located about 0.5 eV from the band gap edge. Upon further oxidation the free radical is removed, creating a new spinless defect called a bipolaron. This is of lower energy than the creation of two distinct polarons. At higher doping levels it becomes possible that two polarons combine to form a bipolaron. Thus at higher doping levels the polarons are replaced by bipolarons. The bipolarons are located symmetrically about 0.77

eV from the band edges for PPy. This eventually, with continued doping, forms into a continuous bipolaron band. Their band width increases as newly formed bipolarons are made at the expense of the distance to the band edges. For a very heavy doped polymer it is conceivable that the upper and the lower bipolaron band will merge with the conduction and the valence bands respectively to produce partially filled bands and metallic-like conductivity. This process is shown in Fig.1.3 and 1.4.

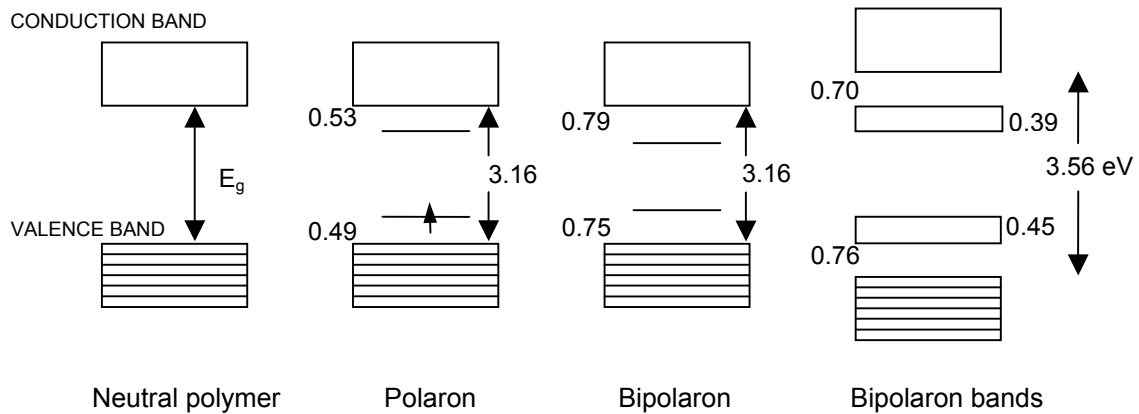


Fig.1.4 Band structure of polypyrrole for neutral, polaron and bipolaron states [1]

1.1.2.2 Charge transport [1, 4]

Although polarons and bipolarons are known to be the main source of charge carriers, the precise mechanism of the conductivity is not yet fully understood. The problem lies in attempting to trace the path of the charge carriers through the polymer. All of these polymers are highly disordered, containing a mixture of crystalline and amorphous regions. It is necessary to consider the transport along and between the polymer chains and also the complex boundaries established by the multiple numbers of phases. This has been studied by examining the dependence of conductivity on doping, temperature, magnetism and the frequency of the current used. These tests show that a variety of conduction mechanisms are possible. The main step is the movement of charge carriers between highly conducting domains. Charge transfer between these conducting domains can occur by thermally activated hopping or tunnelling. This is consistent with conductivity being proportional to temperature.

1.1.2.3 Stability [5]

There are two distinct types of stability. Extrinsic stability is related to vulnerability to external environmental agents such as oxygen, water, peroxides. However, many

conducting polymers degrade over time even in dry, oxygen free environment. This intrinsic instability is thermodynamic in origin. It is likely to be caused by irreversible chemical reactions between charged sites of the polymer and either the dopant counter ion or the π -system of an adjacent neutral chain, which produces an sp^3 carbon, breaking the conjugation. Intrinsic instability can also come from a thermally driven mechanism which causes the polymer to lose its dopant. This happens when the charged sites become unstable due to conformational changes in the polymer backbone. This has been observed in some alkyl substituted polythiophenes.

1.1.2.4 Processing possibility [1, 5]

Conjugated polymers can be synthesized by oxidation of monomers, either chemically or electrochemically. The primarily formed radical cation reacts to dimers, trimers and finally to a conjugated polymer backbone. The main problem with conducting polymers is that they are intractable, insoluble and unmeltable. There are strategies to overcome this problem, either to modify the polymer so that it becomes soluble or to manufacture the polymer in its desired shape and form.

One method is the synthesis of copolymers or derivatives of a parent conjugated polymer with more desirable properties. What is done is to try to modify the structure of the polymer to increase its processibility without compromising its conductivity or its optical properties. All attempts to do this on polyacetylene have failed as they always significantly reduced its conductivity. However, such attempts on polythiophenes and polypyrroles proved more fruitfully. The hydrogen on carbon atoms β in the thiophene and pyrrole ring was replaced with an alkyl group with at least four carbon atoms. The resulting polymer, in doped form, has a comparable conductivity to its parent polymer but it is meltable and soluble. A water soluble version of these polymers has been produced by placing carboxylic acid groups or sulphonic acid groups on the alkyl chains.

Another method is to grow the polymer into its desired shape and form. An insulating polymer impregnated with a catalyst system is fabricated into its desired form. This is then exposed to the monomer. The monomer is then polymerized on the surface of the insulating substrate producing a thin film or a fibre. This film is then doped in the usual manner. A variation of this technique is the electrochemical polymerization of conducting polymers on an electrode surface.

A special method is to prepare colloidal dispersions of conducting polymers [5]. For example, PPy and PANI are usually synthesized using chemical oxidants [e.g., FeCl₃ or (NH₄)₂S₂O₈] in either acidic aqueous media or certain nonaqueous solvents such as ethers, esters, alcohols or acetonitrile. Initially the monomer and oxidant species are dissolved separately in homogeneous solutions. Mixing the solutions the system becomes heterogeneous owing to precipitation of insoluble, microscopic conducting polymer particles. Such particles are usually stabilized with respect to aggregation by either a steric or a charge stabilization mechanism. Steric stabilization involves the use of suitable polymeric stabilizers that absorb onto the conducting polymer particles to form a thick solvate layer. This outer layer of absorbed polymers provides a steric barrier to particle aggregation [5].

1.1.2.5 Application

The conjugated polymers are highly sensitive to chemical and electrochemical oxidation or reduction. These processes change the electrical and optical properties of the polymers. By controlling this oxidation and reduction, it is possible to control these properties. These reactions are often reversible so that it is possible to systematically control the electrical and optical properties with a great deal of precision. It is even possible to switch from a conducting form to insulating form. According to these behaviours, there are two main groups of application for conducting polymers. The first group utilizes their conductivity as their main properties. The second group utilizes their electroactivity. They are shown in the table 1.1.

Tab.1.1 Some applications of conducting polymers

Group 1 (Conductivity)	Group 2 (Electroactivity)
Electrostatic materials [6] Conducting adhesives [7] Electromagnetic shielding [6] Ink jet printed material [8] Antistatic clothing [9] Piezoceramic [9]	Active electronics (diodes, transistors) [1, 4] Molecular electronics [10] Rechargeable batteries and solid electrolyte [11] Chemical, biochemical and thermal sensors [12] Ion exchange membrane [13] Electromechanical actuators [14] “Smart” structures [15]

Much research is needed before many of the above applications will become a reality. The stability and processibility both need to be improved if they are to be used in the market place. The cost of such polymers must also be substantially lowered. However, one must consider that, although conventional polymers were synthesized and studied in laboratories around the world, they did not become widespread until years of research and development had been done. In a way, conducting polymers are at the same stage of development as the insulating polymers were many years ago. Regardless of the practical applications eventually developed, they certainly will challenge researchers in the years to come with new and unexpected phenomena. Only time can tell whether the impact of the novel plastics will be as large as the insulating polymers.

1.2. Conducting polymer nanocomposites

1.2.1 Introduction

Nanoclusters are ultrafine particles of nanometer dimensions whose properties are size dependent and are different from those of the bulk counterparts. Nanocomposites are formed from suitable combinations of two or more materials in nanoparticles, usually in a core / shell structure, resulting in materials having new physical properties.

Normal conducting polymers are generally insoluble in common solvents. Such inherent intractability has prevented the conducting polymers from combining with the foreign materials in conventional blending techniques. But it is possible to combine conducting polymers with e.g. oxide particles by synthesizing a thin film of conducting polymer on the surface of the particle. This will be described in the following chapter.

1.2.2 Chemical process

1.2.2.1 Nanocomposite particles with core-shell structure

Coating inorganic particles by conducting polymers has become the most popular and interesting aspect of nanocomposite synthesis. Recently, a variety of different metal and metal oxide particles have been encapsulated by conducting polymers giving a number of nanocomposites [16, 17, 18]. For the first time this encapsulation was carried out by Armes *et. al* when they incorporated silica particles (1 μ m) into the core of PANI and PPy [19]. The composites were characterized by thermogravimetric analysis (TGA), scanning electron microscopy (SEM), four-point probe conductivity measurements, Fourier transform infra-red microscopy (F-IR) and Rutherford back-scattering spectrometry. Unlike the PPy-silica system, the PANI composite, in doped form, could be redispersed in concentrated H₂SO₄ while in undoped form it was dispersible in DMF [19]. Further experiments with PPy, PANI and PEDOT and smaller SiO₂ (<1 μ m) colloids were described in [20, 21, 22, 23, 24, 25, 26]. In these experiments conducting polymers were prepared via chemical processes by (NH₄)₂S₂O₈ [20, 21, 23, 26] or FeCl₃ [21, 24, 25]. The particle size and the morphology of the nanocomposite particles were investigated [20, 23 and 26]. For the PPy-silica nanocomposites, there is a strong correlation between the silica content of these materials and their BET surface area [21]. Nanocomposites with iron oxide cores were described in Ref. [27, 28, 29, 30, 31, 32, 33, 34]. These studies focused on the magnetic properties of nanocomposites, e.g. of Fe₃O₄. The room temperature conductivity

of PPy/Fe₃O₄ was higher than that of pure PPy, reaching a maximum at about 11.36 S.cm⁻¹ [34]. The saturated magnetization ($M_s = 6.89 - 16.98 \text{ emu.g}^{-1}$) increased linearly with the Fe content in the composites [34], but the coercive force was very low ($H_c = 5-12 \text{ Oe}$) [34]. It was possible to prepare soft magnetic materials. Semiconducting oxide particles (such as TiO₂ and BaTiO₃) were also used as the cores of conducting polymer / nanocomposites [35, 36, 37, 38, 39]. All these nanocomposites were prepared by chemical processes in the colloidal suspensions. The thermal decomposition properties and chemical structures of these materials were studied through TGA measurements [35, 38, 39], F-IR, Raman [38, 39] and UV spectra [35, 37]. The charge transport mechanism and the current-voltage characteristics of such materials was investigated by Somani *et al.* [36, 37, 40]. I/V characteristics showed the typical Schottky diode type behaviours, indicating that the charge was accumulated at the interface between conducting polymers and semiconducting oxide particles [36, 37, 40]. Other core materials were Al₂O₃ and clay [41, 42, 43, 44].

So far it was difficult to prepare composite nanoparticle layers on conductive substrates to investigate the electrochemical and photoelectrochemical properties. Ramachandra and Lerner prepared PPy/clay composite layers on platinum electrode by casting and studied the electrochemical behaviour of the layers by cyclic voltammetry (CV) and chronopotentiometry [44]. The negative shift of the PPy oxidation potential, in comparison with that of pure PPy prepared by chemical polymerization, was explained as an influence of the clay. Hoffmann *et al.* prepared PTh/TiO₂ composite layers on platinum plates by rubbing pressed pellets [45]. The composite layers were characterized by CV and photoelectrochemical measurements. Electrochemical impedance spectroscopy (EIS) was used to study the electrochemical behaviour of composites. Oxidation potential, flatband potential, bandgap energy, etc of PTh were determined. A behaviour similar to a p-type semiconductor with a charge carrier density of $N_D = 1.66 \times 10^{19} \text{ cm}^{-3}$ was observed in contact with the n-type semiconductor TiO₂ [45].

Gurunatha *et al.* prepared PANI/TiO₂ by chemical oxidation from aniline monomers and TiCl₄ [46]. The properties of the composites were characterized by X-ray diffraction (XRD), UV-VIS spectra, TGA/DTA and FTIR. The composite was used as a cathode material for rechargeable batteries with a zinc container as the anode, cellulose acetate as the separator and polyvinyl sulfate and carboxy methyl cellulose as the solid polymer electrolyte. A cylindrical AA type rechargeable battery was fabricated with the following performance data: The open circuit voltage was 1.4 V, the current was 250 mA to 1.0 A for

50 recharge cycles, the power density was 350 A h/kg and power efficiency was 70 % [46] (Fig.1.5).

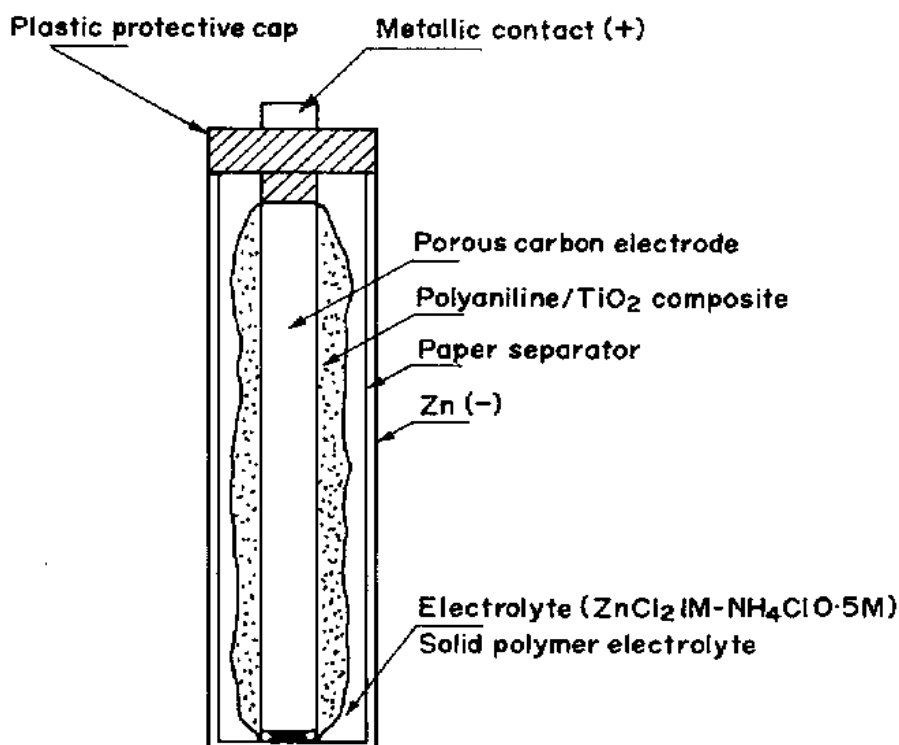


Fig.1.5 Battery cell fabricated by using PANI/TiO₂ composite as the cathode material [46]

1.2.2.2 Nanocomposite layers prepared by chemical oxidation

Nanocomposite layers could be prepared on oxide surfaces by oxidation of a solution of monomers. An extremely adhesive polybithiophene (PBT) film was grown on TiO₂ in a new, two-step procedure using a silyl substituted thiophene derivative as a surface coupling agent and a subsequent chemical polymerization process [47]. The results of impedance and photocurrent measurements were summarized in a band model [47]. In dye sensitized solar cells, PPy or PEDOT were used as the hole transport phase in place of liquid electrolytes [48, 49]. Combination of the polymers with ruthenium dyes which have pyrrole or thiophene units in the ligand system improved the photovoltaic performance of the solar cells [49]. The use of a carbon-based counter electrode and treatment of the polymer phase with an ionic liquid also improved the cell performance of the solar cells. These effects were attributed to the enhancement of charge transport properties of the components [49].

1.2.3 Electrochemical preparation

There are two main ways to prepare conducting polymer nanocomposites via an electrochemical process.

1.2.3.1 Electropolymerization of conducting polymer on metal oxide layer

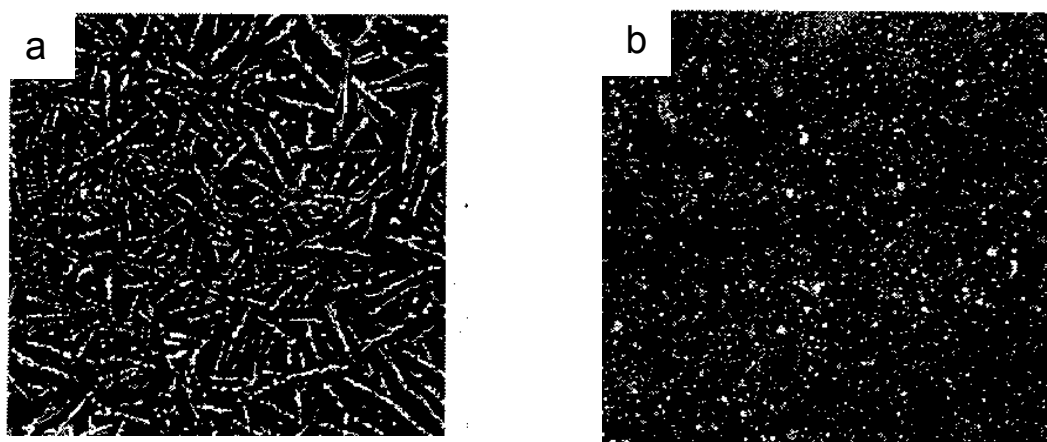


Fig.1.6 SEM photographs of PPy films with different thickness (d) on the microporous of TiO_2 : a) $d = 300$ nm and b) $d = 600$ nm [53]

A conducting polymer was electropolymerized on a TiO_2 oxide layer prepared previously on the Ti electrode. In Ref. [50], PPy was deposited on thin chemically pre-oxidized Ti layer, producing a mechanically strong, shiny polymer film with extremely good adhesion. In Ref. [51], PMT was deposited on thin electrochemically pre-oxidized Ti layer using a nitrogen fixation system consisting of titanium oxide (TiO_x) and PMT producing ammonium salt crystals ($\text{NH}_4^+\text{ClO}_4^-$) and ammonia when exposed to white light in air at 20°C and 40% relative humidity. The fixation yield was strongly depending on the thickness of the PMT layer, the potential at which the TiO_x was prepared, and the kind of the conducting polymer material [51]. Conducting polymers could also be deposited on metal oxide layers previously prepared by other techniques such as sol gel method [52], spin coating [53] and casting [54]. Polybithiophene (PBTh) was deposited on a TiO_2 layer prepared by the sol gel method to fabricate an ITO/ TiO_2 /PBT/Au cell and the photovoltaic effect was observed from this cell. A PBT/ TiO_2 heterojunction was used as a rectifying contact [52]. A PPy/ TiO_2 diode was prepared by electrochemical deposition of PPy on microporous TiO_2 film [53]. A suitable thickness of the PPy films was of great importance in enhancing the rectifying ratio of PPy/ TiO_2 diode [53]. Different PPy films with different thicknesses had different morphologies, as illustrated in Fig.1.6. A nanostructured ZnO film was prepared from colloidal suspensions in ethanol [54]. Then PPy was deposited on

the dye-sensitized ZnO layer to fabricate a solar cell with a nanostructured ZnO/dye/PPy film electrode. A fill factor of 0.75 and a high overall light to electricity conversion efficiency of 1.3% was obtained with this solar cell [54].

1.2.3.2 Codeposition of conducting polymers and oxide particles

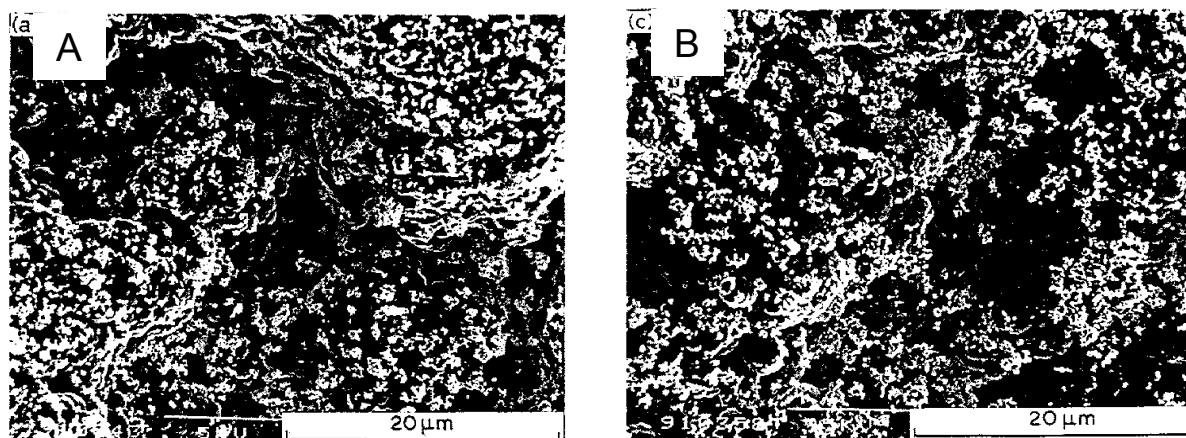


Fig.1.7 SEM photographs of PPy/TiO₂ composite layers of different thickness (d)
A) d = 3 μm and B) d = 30 μm prepared by codeposition [57]

Conducting polymer nanocomposites could be prepared by electropolymerization of conducting polymers from a solvent containing the monomers and oxide particles. During polymerization, the oxide particles were codeposited at the electrode to give nanocomposites. Yoneyama and his co-workers electrodeposited PPy/TiO₂ composites [55]. The mechanism of codeposition was explained by negative surface charge of TiO₂ particles being transported to the anode and incorporated in the growing PPy film. Beck *et al.* prepared PPy/TiO₂ and PPy/WO₃ nanocomposites [56, 57]. In his studies, the anodic codeposition of PPy and oxide particles was carried out in an electrolyte containing 0.1 M pyrrole and 0.1 M LiClO₄ or 0.1 M NBu₄BF₄. The dependence of oxide mass in the composite and the concentration of oxide particle in the dispersion was investigated. Beck confirmed Yoneyama's mechanism for the codeposition process [56, 57]. By SEM it was observed that mainly agglomerates were present on the surface of the composite (Fig.1.7). In the case of TiO₂, the photoelectrochemical response in 0.5 M KCl (H₂O) electrolyte was studied [56]. A Na⁺-montmorillonite clay/PPy composite was prepared by an electrochemical polymerization method on a gold substrate [58]. The results indicated instantaneous two-dimensional nucleation and growth distinguishable from the nucleation and growth of pure PPy [58]. Codeposition of conducting polymers and oxide particles was not only investigated on platinum electrode but also on iron and steel surfaces for corrosion

protection. Many metal oxides were used for this purpose TiO_2 , Fe_3O_4 , Fe_2O_3 , V_2O_5 and MnO_2 [59, 60]. In these experiments, oxalate electrolytes were used. Corrosion tests were performed by weight loss and salt spray methods [60]. The results indicated that the nanoparticles inhibited the corrosion process.

1.2.4 Physical preparation

Films of soluble conducting polymers can be prepared by spin-coating, dip-coating, casting or simply by drop-coating on the photosensitive layers (such as TiO_2 , ZnO , CdSe). Examples are described in Refs. [61, 62, 63, 64, 65, 66, 67, 68, 69, 70, 71, 72, 73]. Mainly photocells were prepared and cis-bis(isothiocyanato)bis(2,2'-bipyridyl-4,4'-dicarboxylato) ruthenium(II) ($\text{RuL}_2(\text{NCS})_2$ or N3) with or without tetrabutylammonium (TBA) salt was used as light sensitizer. Fig.1.8 shows the structure of a solar cell using conducting polymer as a hole transport material.

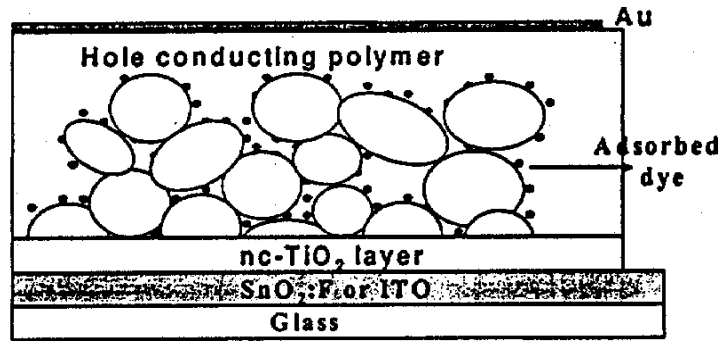


Fig.1.8 Schematic construction of a solar cell [66]

The photovoltaic devices are tested by linear sweep voltammetry. The characteristic I/V curve is shown in Fig.1.9. A photovoltaic cell is characterized by the short circuit current (J_{sc}), open circuit voltage (V_{oc}), fill factor (FF) and energy conversion efficiency (F) [74, 75]. The open circuit voltage is measured for zero current. The short circuit current is measured for zero voltage. The fill factor is given by:

$$FF = \frac{I_{\max} V_{\max}}{J_{sc} V_{oc}} \quad (1.1)$$

The absolute values of I_{\max} and V_{\max} depend on the shape of the current – potential curve under illumination and must be selected so that the rectangle is maximized [74, 75]. The energy conversion is given by:

$$F = \frac{I_{\max} V_{\max}}{P_o} = \frac{J_{sc} V_{oc} FF}{P_o} \quad (1.2)$$

Tab.1.2 Characterization of some solar cells using conducting polymers

Polymer	Dye	$J_{sc}(\mu A)$	$V_{oc}(V)$	FF	F(%)	Literature
P4UBT	N3	72	0.68	0.34	-	[72]
P3UBT	N3	62	0.65	0.44	-	[72]
P4UBT	-	35	0.78	0.39	-	[72]
P3UBT	-	29	0.69	0.39	-	[72]
MEH-PPV	-	320	0.92	0.52	-	[70]
P3HT	-	200	0.32	-	0.15	[76]
PTAA	-	5700	0.35	-	0.18	[76]
H-PURET	-	8000	0.46	-	1.5	[76]
PURET	-	4500	0.46	-	1.4	[76]
P3UBT	-	100	0.92	0.30	-	[68]
MEH-PPV	-	300	0.4	0.30	0.05	[67]
P3OT	N3/TBA	450	0.65	0.44	0.16	[66]
P3OT	-	230	0.70	0.37	0.08	[66]
P3OT	-	250	0.72	0.35	0.06	[77]
P3UBT	-	223	0.78	0.40	0.07	[64]
P3UBT	N3	539	0.53	0.37	0.11	[64]
P3BT	-	39	0.51	0.68	-	[63]
P3OT	N3/TBA	27	0.57	0.43	-	[62]
P3OT	-	9	0.56	0.36	-	[62]

In which P_0 is the power of the incident light. Some characteristic data of solar cells using TiO_2 and conducting polymers are presented in Tab.1.2. The overall energy conversion efficiency (F) of these solar cells is still low in comparison to solar cells using dye sensitized TiO_2 [78]. The best cell shows an energy conversion efficiency of 1.5 % with a rather high current density of 8 mA.cm⁻² [76].

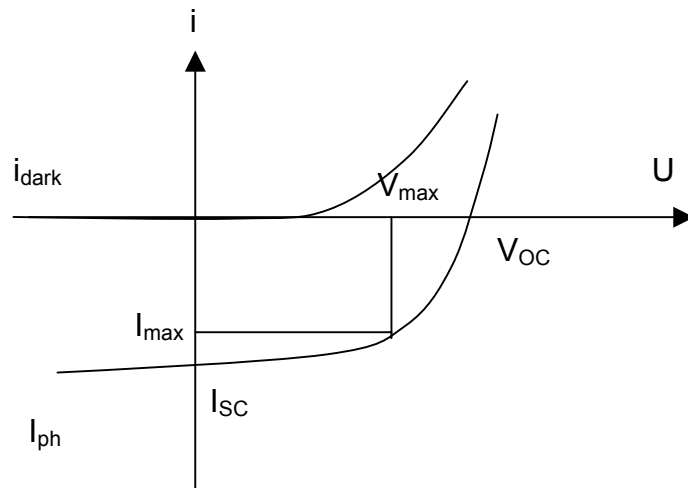


Fig.1.9 Current – voltage plot of a photovoltaic device

1.2.5 Other processes

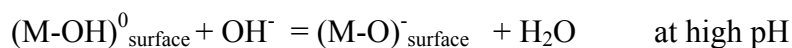
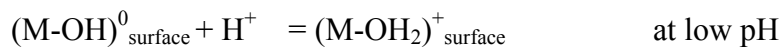
There are other methods to prepare conducting polymer composites. These processes are usually applied for PANI and PPy. PPy composites were prepared by oxidation of monomers on the surface of transition metal oxide particles as the catalysts for several hours [79, 80, 81, 82, 83]. Temperatures used for polymerization were 50-100⁰C. PPy/TiO₂ composites were produced by UV irradiation of a mixture of TiO₂ particles and pyrrole monomers in oxygen-saturated water [84]. Polymerization occurred on an irradiated surface of n-TiO₂ in aqueous solutions of pyrrole when the electrode potential was set between - 0.6 and + 1.5 V_{SCE} [85]. Some conducting polymers used for fabrication of photoelectrochemical cells were prepared by this way [86, 87].

Part II Theoretical background of electrophoretic deposition (EPD)

2.1 Introduction

The phenomenon of electrophoresis has been known since the beginning of the 19th century and was applied mainly in the traditional ceramic technology [88, 89, 90, 91]. A dc electric field is applied across a colloidal suspension of charged particles depositing a film of particles on the oppositely charged electrode. Electrophoretic deposition (EPD) is essentially a two-step process: electrophoretic transport and deposition. In the first step, charged particles in a liquid are forced to move toward an electrode by applying an electric field to the suspension. In the second step, the particles collect and are deposited the electrode having opposite surface charge. A post-EPD processing step is usually required, which includes a suitable heat-treatment (firing or sintering) in order to further densify the deposits and to eliminate porosity. The advantages of EPD are that [90]: (i) the deposition rate is high, (ii) coatings can be made in any shape, (iii) the film is dense and uniform, (iv) the thickness of the film can be controlled by the deposition condition and (v) the process is simple and easy to scale up. EPD needs a stable suspension with particles charged so as to respond to an applied electric field. This stability of the suspension can be obtained by the following processes [89, 91, 92, 93]:

(a) Selective adsorption of ions onto the solid particle from the liquid. This is commonly observed on oxide surfaces with adsorbed carboxylic acid or amine groups. Oxide surfaces can be considered to consist of a large number of amphoteric hydroxyl groups that can undergo dissociation to produce either H⁺ or OH⁻ ions:



Adsorption of ions from the electrolyte on the particle surface is another charging process. Carbon black, for example, can become negatively charged by adsorption of anionic surfactants [89]. Al³⁺ can be adsorbed on SiC particles [92].

(b) Dissociation of ions from the solid phase into the liquid. An example of this mechanism is the AgI / water system wherein either Ag⁺ or I⁻ adsorb on the AgI to establish equilibrium (in equilibrium, the electrochemical potentials of Ag⁺ and I⁻ ions are the same at the AgI surface and in the bulk aqueous solution).

(c) Adsorption of dipoles at the particle surface.

(d) Electron transfer between the solid phase and the liquid phase due to differences in the work function.

Counter ions from the liquid form a charge cloud around a charged particle masking their surface charge (Fig.2.1). This ionic atmosphere is called the ‘diffuse-double layer’ or ‘lyosphere’. When an electric field is applied, these ions and the particle move in opposite directions. However, the ions are also attracted by the particle, and as a result, a fraction of these ions surrounding the particle will not move in the opposite direction but move along with the particle. Hence, the speed of a particle is not determined by the surface charge but by the net charge enclosed in the liquid sphere, which moves along with the particle. The potential at the surface of shear is called the zeta potential or electrokinetic potential. It is experimentally accessible.

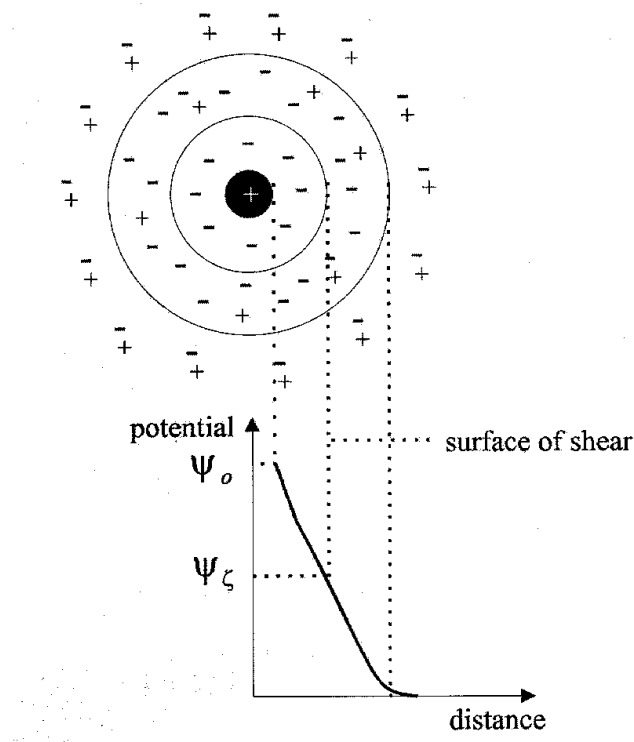


Fig.2.1 The double layer surrounding a charged particle and evolution of the electric potential from the surface potential, Ψ_0 , to zero far from the particle. The potential at the surface of shear, the limit between the liquid moving with the particle and the liquid, which does not move with the particle, is termed the zeta potential, Ψ_ζ , and is the main parameter determining the electrokinetic behavior of the particle [91]

The DLVO (Derjaguin–Landau–Verwey–Overbeek) theory describes colloidal suspension stability using attractive - and repulsive - energy concepts [89, 93]. When two particles approach each other, their double layers overlap and they experience a repulsive force. The

origin of the repulsive force between two similarly charged particles is osmotic, not electrostatic [89, 93]. The force at any point between the particles consists of two components, i.e. an electrostatic component, which is always attractive and an osmotic pressure component, always repulsive. In the double layer, the repulsive osmotic pressure between counter ions forces them away from the particle surfaces and from each other. Electrostatic forces are attractive. Since the former dominate, the net force is repulsive.

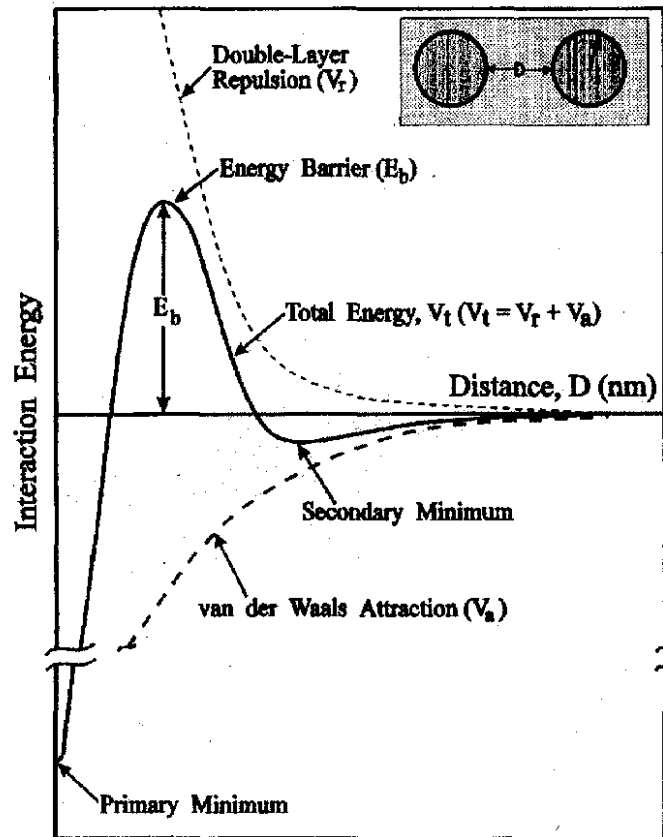


Fig.2.2 Schematic of the interaction energy as a function of separation between two particles in suspension [89, 93]

A van der Waals attraction always exists between particles and is given by [89, 93]:

$$V_a = -\frac{H.r_1r_2}{6D(r_1 + r_2)} \quad (2.1)$$

where V_a is the van der Waals attractive force, H is the Hamaker constant, D is the separation of the particles and r_1 and r_2 are their radii. Since this attractive relationship follows a power law, it dominates at small separations. A primary minimum is therefore observed at the position of the particle – particle contact ($D = 0$, Fig.2.2). As separation

increases, the double layer repulsion dominates. Consequently the total – interaction – energy curve exhibits a peak of height E_b . This is the energy – barrier to particle coagulation. A secondary minimum develops at large distances when the attractive van der Waals energy term dominates. If particles approach closer than the primary energy barrier, they adhere irreversibly. The secondary minimum also can result in coagulation, but adhesion is weak and reversible.

In an electric field, the equilibrium speed of the particle is determined by four forces acting on the particle [94, 95]. The first, which accelerates the particle, is the force caused by the interaction of the surface charge with the electric field. All other forces slow the particle. They are viscous drag from the liquid, the force exerted by the electric field on the counter ions in the double layer (retardation) and, when a particle moves, the distortion in the double layer caused by a displacement between the center of the negative and positive charge (relaxation).

2.2. Mechanism of electrophoretic deposition

Although EPD is an old process, the mechanism of EPD is still not entirely clear.

The first attempt to explain the phenomenon of EPD was made by Hamaker and Verwey [96]. They proposed, EPD is based on the accumulation of particles on the electrode. On standing, an EPD suspension was observed to produce a strongly adhering sediment. Therefore, the phenomena of EPD and sedimentation were suggested to be identical in nature. The primary function of the applied electric field in EPD was to move the particles toward the electrode where deposition takes place. They pointed out that successful EPD needs stable suspension. Koelmans and Overbeek [97, 98] studied the EPD in polar organic media and pointed out that Hamaker's mechanism exclusively considered the accumulation of particles on the electrode and ignored the parallel transportation of ions. As a result, Hamaker ignored the concomitant increase of ionic concentration and electrode reaction on the depositing electrode. They calculated the electrolyte concentration near the depositing electrode and showed it is comparable with that required to coagulate the powder and form a deposit. They proposed an electrochemical mechanism of deposit formation. The basic of their mechanism is the DLVO theory. They proposed the deposit forms due to particle flocculation via the increased electrolyte concentration and the reduced zeta potential near the depositing electrode. Grillon *et al.* [99] suggested that particles undergo charge neutralization when they touch the depositing electrode or deposit. Shimbo *et al.* [100]

proposed secondary processes on the electrode produced hydroxides, which could adsorb on the particles and polymerize, holding them together in the deposit. Mizuguchi *et al.* [101] studied EPD of a variety of oxide powders (such as Al_2O_3 , MgO , ZnO , etc.) and metallic powders (such as W, Mo, Al, etc.) and pointed out that anodic deposition was possible in the presence of sulfuric acid and nitrocellulose. They combined the particle neutralization and Shimbo's polymerization mechanism. They proposed discharge of sulfate ions on the particle surface at the anode, bringing the particles closer to the anode surface so that the nitrocellulose chains present on the particle surface could form the necessary bridges and cause deposition. Some authors [102, 103] deposited a monolayer of gold and silver particles by EPD. This result shows that the accumulation of particles is not following Hamaker's theory.

Sakar *et al.* [89, 93, 104] used a dialysis membrane to separate the working electrode from the suspension to study the mechanism of EPD. Liquid, (the same as the suspension liquid), was filled into the cavity between the cathode and the membrane to provide an ionic path. A dc field was applied and the particles moved and stopped at the membrane. The current continued to pass, however, thus ions permeated the membrane to complete the electrical path during EPD. A dense deposit formed on the membrane, so they suggested that particle / electrode reactions are not involved in EPD. Particle neutralization on the electrode could be excluded. Also, dialysis membrane deposition occurred at any location between anode and cathode. Sakar concluded that local increase of electrolyte concentration around the depositing electrode (Koelmans' theory) could also be excluded and pointed out that a mechanism involving hydroxide formation and polymerization (Shimbo's theory) was unlikely because deposition could occur on the anode or cathode depending on the particle nature and even noble metals, carbon, etc., could be deposited. They gave an alternate explanation based on extension of the DLVO theory. They considered that an overall-positively charged oxide particle / lyosphere system (for instance, $[(\text{M}-\text{OH}_2)^+\text{X}^-]$) was moving toward the depositing electrode in an EPD cell (for example, the cathode; Fig.2.3). Fluid dynamics and the applied field could distort the double layer shell, thinning ahead and widening behind the particle. Cations in the liquid could also move to the cathode with the positively-charged particles. The counter-ions in the extended tails would be neutralized. As result of this reaction, the double layer around the tail of the particle would become so thin so that the next incoming particle (which has a thin heading double layer) could approach close enough for coagulation / deposition [89, 93]. Fig.2.3 shows

schematically the mechanism of coagulation / deposition via lysosphere distortion and thinning following Sakar's theory.

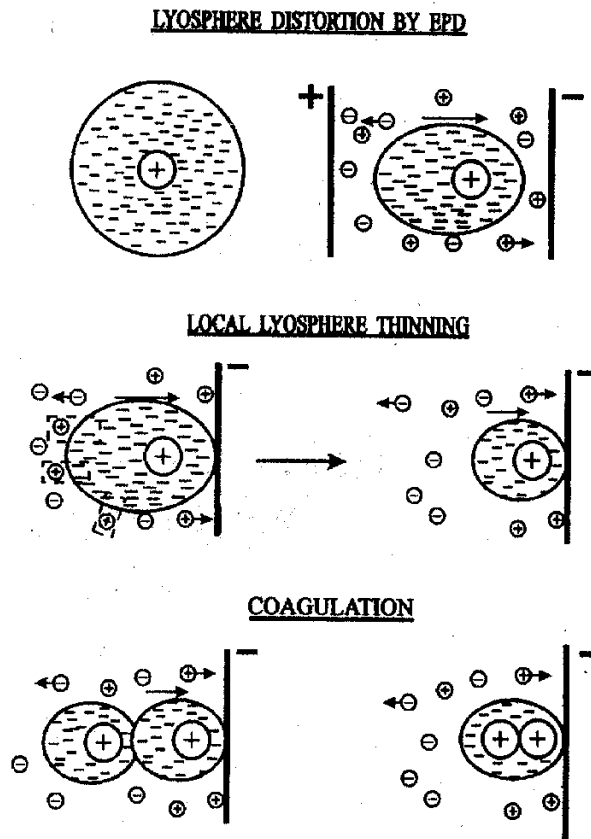
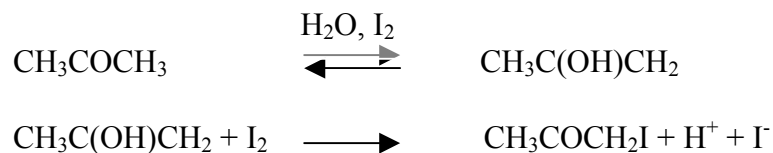


Fig.2.3 Schematic representation of the deposition mechanism by lysosphere distortion and thinning [89, 93]

A type of suspension is a powder charged positively by adsorption of protons or metal ions on the particle surface. Koura *et al.* [105] prepared a suspension containing H₂O, I₂, oxide particles in acetone for EPD. The charging of metal oxide particles was connected with H⁺ ions produced in the bath by the keto-enol reaction of acetone:



The amount of H⁺ ions adsorbed on an oxide particle was calculated by the Gouy – Chapman theory. The current – time dependence was found to satisfy the Cottrell equation. The following EPD mechanism was proposed: The charge transfer occurs on the cathode surface. The rate – determining step of the depositing reaction arise is the diffusion of H⁺ ions desorbed through small holes in the oxide film (Fig.2.4).

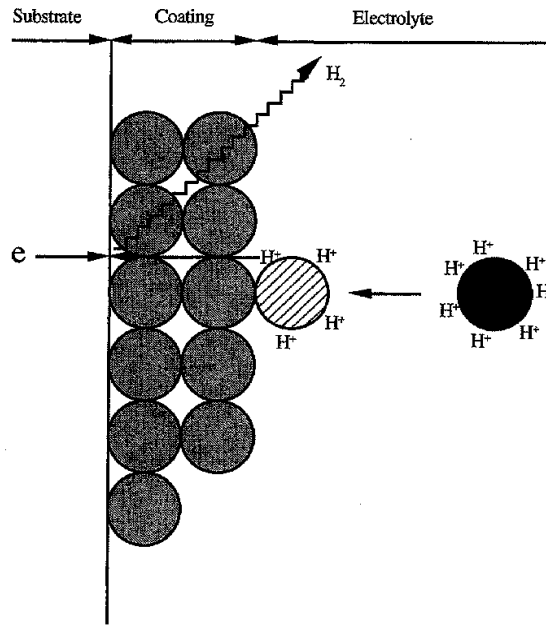
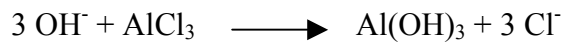
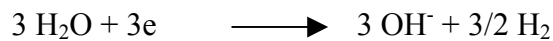


Fig.2.4. Schematic model for the EPD mechanism of the oxide particle charged by adsorbed H^+ [105]

The influence of metal cation added to the suspension (e.g. $Mg(NO_3)_2$, $La(NO_3)_3$, $Y(NO_3)_3$, $MgCl_2$, or $AlCl_3$) were studied in Ref. [92, 104, 106, 107]. Bouyer and Foissy [92] deposited cathodically SiC particles in ethanol using $AlCl_3$ as a charge promoter, water as an electrolyte additive and polyvinylbutyral (PVB) as a suspension stabilizer. A maximum deposition yield was measured with an $AlCl_3$ concentration of $3 \cdot 10^{-4}$ M, corresponding to the limit of strong adsorption of Al^{3+} on SiC particles. EPD was associated with formation of $Al(OH)_3$ found on the cathode.



For a comparison of electrical charge and yield of deposition the authors assumed that the electrochemical processes at the electrode were involved in the EPD process.

The fact that in many reports on EPD little attention is given to the deposition mechanism clearly shows that even if a full understanding of the mechanism is lacking, EPD is already successfully used. However, a better understanding would reduce experimental work required to determine the optimal parameters of EPD.

2.3. Kinetics of electrophoretic deposition

The kinetics of EPD has been the subject of several investigations. In 1940, Hamaker [108] observed that the deposited weight of EPD varies linearly with the amount of charge passed. From the observations for constant voltage depositions, Hamaker proposed that deposited weight is proportional to the concentration of the suspension, time of deposition, surface area of deposit and electric field. The proportionality constant is equal to the electrophoretic mobility of the particle when every particle reaching the electrode is deposited.

$$\frac{dW}{dt} = f \cdot \mu \cdot U \cdot S \cdot C \quad (2.2)$$

where W is the deposited weight, t is the deposition time, μ is the electrophoretic mobility, S is the surface area, C is the electrolyte concentration, U is the applied potential and f is a correction factor ($f \leq 1$). This equation is now accepted as the basic kinetic equation of EPD. Sussman and Ward [109], studying the EPD of glass particles, gave two kinetic equations: one for constant current and one for constant voltage. In 1991, Hitara *et al.* [110] developed a kinetic equation based on Faraday's law. This equation is valid for constant current. All authors in Ref. [108, 109, 110] ignored the change of solid concentration in the suspension during deposition.

In 1994, Zhang *et al.* [111] derived a kinetic equation:

$$\frac{dW}{dt} = k \cdot C_0 \cdot \exp(-k \cdot t) \quad (2.3)$$

k is the "kinetic" parameter and given by the equation:

$$k = \frac{S \cdot \epsilon \cdot \zeta}{4\pi \cdot \eta} (U - \Delta U) \quad (2.4)$$

where, C_0 is the initial concentration of suspension, S is the surface area of the electrode, ϵ is the dielectric constant of liquid, ζ is zeta potential of the colloidal particles, η is the viscosity of solvent, U is the initial electric field and ΔU is its change with a time, t . For the case of a constant solid concentration and constant electric field, equation (2.3) becomes:

$$W_t = C_0 [1 - \exp(-kt)] \quad (2.5)$$

When deposition time is short, $\exp(-kt)$ is equal to $(1-kt)$, and equation (2.5) changes into:

$$W_t = C_0.k.t \quad (2.6)$$

The Zhang's equation (2.6) is valid for short deposition time and for constant concentration of a suspension [111].

In 2001, Will *et al.* [112] developed a similar kinetic EPD model. From Hamaker's theory, they formulated the following equation:

$$W_t = \int_0^t f.S.\mu.C_t.E_t.dt = f.S.\mu \int_0^t C_t.E_t.dt \quad (2.7)$$

During the deposition process the particle concentration in the suspension C_t decreases. The time dependence of the particle concentration is given by [112]:

$$C_t = C_0(1 - \frac{W_t}{W_\infty}) \quad (2.8)$$

With W_∞ is the deposited weight for $t \rightarrow \infty$

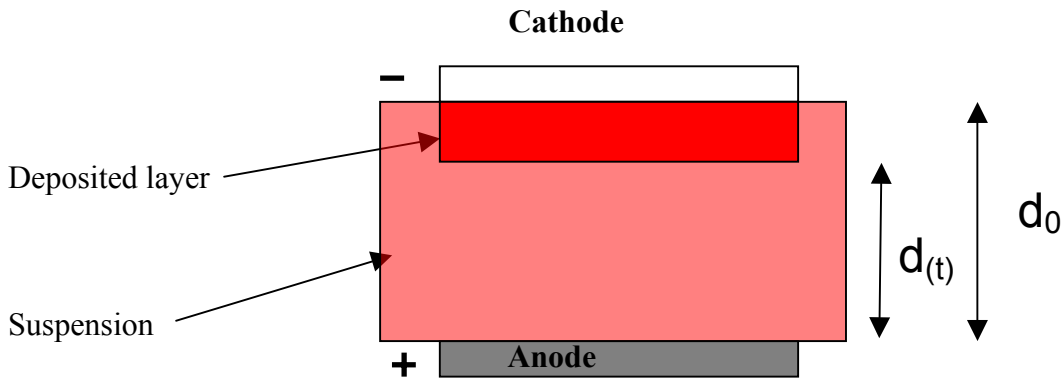


Fig.2.5 Arrangement of the EPD electrodes with respect to the suspension and the deposited layer [112]

In the case of constant voltage U_0 between the electrodes, the electric field strength E_t in the suspension will decrease because of the formation of the deposit. The resulting decrease of the total resistance of the system can be described by introducing a time-dependent, larger effective distance d_t between the electrodes with the same resistance as the suspension:

$$E_t = \frac{U_0}{d_t} \quad (2.9)$$

with
$$E_0 = \frac{U_0}{d_0} \quad (2.10)$$

where, d_0 is the geometrical distance between the electrodes. The time dependence of the effective distance can easily be determined from the following equation [112]:

$$d_t = d_0 + d_{D(t)} \left(\frac{\varepsilon_D}{\varepsilon_S} - 1 \right) \quad (2.11)$$

where, $d_{D(t)}$ is the deposit thickness and ε_D , ε_S are the dielectric constants of the deposit and of the suspension, respectively. By means of the density ρ_D of the deposit, the thickness $d_{D(t)}$ can be related to the deposited mass [112]:

$$d_{D(t)} = \frac{W_t}{\rho_D \cdot S} \quad (2.12)$$

W_t is the deposited mass at time t and S is the electrode surface area. The effective distance can now be written by:

$$d_t = d_0 + k'' \cdot W_t \quad (2.13)$$

where the constant k'' is given by:

$$k'' = \frac{\frac{\varepsilon_D}{\varepsilon_S} - 1}{\rho_D \cdot S} \quad (2.14)$$

Therefore, the equation (2.9) becomes:

$$E_t = \frac{U_0}{d_0 + k'' \cdot W_t} \quad (2.15)$$

The deposition equation can be described by combining Eq. (2.7), (2.8) with Eq. (2.15):

$$W_t = f \cdot S \cdot \mu \cdot C_0 \cdot U_0 \int_0^t \left(1 - \frac{W_t}{W_\infty} \right) \left(\frac{1}{d_0 + k'' \cdot W_t} \right) dt \quad (2.16)$$

This equation can be simplified, when the experimental setup allows one to neglect the change of the concentration during deposition ($C_t = C_0$ or $W_t / W_\infty \approx 0$) [112]:

$$W_t = f \cdot S \cdot \mu \cdot C_0 \cdot U_0 \int_0^t \frac{1}{d_0 + k'' \cdot W_t} dt \quad (2.17)$$

By integration of this equation, Will *et al.* derived the time dependence of the deposited mass for constant voltage U_0 and constant concentration C_0 [112]:

$$W_t = \frac{d_0}{k''} + \sqrt{\frac{d_0^2}{(k'')^2} + \left(\frac{2f.S.\mu.C_0.U_0}{k''}\right)t} \quad (2.18)$$

The deposited layer thickness $d_{D(t)}$ can be expressed by combining this solution with (2.12). Using the results and hypothesis of Hamaker, Will *et al.* gave the following relation between the total charge passed during deposition and the deposited mass W_t [112]:

$$Q_t = \int_0^t I_t \cdot dt = \rho_Q a_s W_t \quad (2.19)$$

where, I_t is the time-dependent electrical current, ρ_Q is the surface charge density on the particles and a_s is the total surface area of the particles deposited.

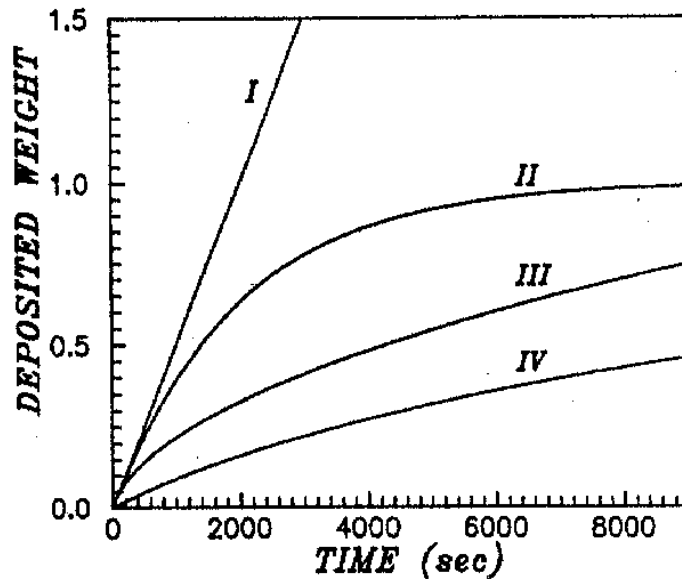


Fig.2.6 Deposited weight as a function of time for four different deposition conditions (I: constant current and constant concentration, II: constant current but variable concentration, III: constant voltage and constant concentration and IV: constant voltage but variable concentration) [89]

Sakar [89] proposed that the observation that deposited weight is linear with the charge passed occurs in the case of the concentration of suspension not influencing the deposition rate. Therefore, curves (I) and (III) (Fig.2.6) show this behavior throughout the deposition. Curves (II) and (IV) show this behavior in the initial stage of deposition. He pointed out that although Hamaker did not use constant concentration, he observed this behavior because he was monitoring the early stage of curve (IV) [89, 113]. Deposited weight in EPD is directly proportional to the particle concentration and velocity, which, in turn, are directly proportional to the voltage drop / unit length of the suspension. Therefore, the deposited weight at constant concentration is linear with the charge passed [89].

2.4. Application of electrophoretic deposition

In general, EPD can be used with any fine powder of nanoparticles (< 30 μm) or colloidal particles. Examples can be found, including metals, polymers, carbides, oxides, borides and glasses (Tab.2.1). The potentials of EPD for the realization of unique microstructures and novel (and complex) shapes and dimensions are appreciated by material scientists and technologists.

Tab.2.1 Some applications of the electrophoretic deposition

Material	Example
Oxides	Al_2O_3 [114, 115, 116, 117, 118, 119, 120, 121], TiO_2 [101, 105, 106, 122, 123, 124], MgO [101, 105, 106, 125, 126], ZnO [101, 127], PbO [105, 106], MoO_3 [106], WO_3 [105], CuO [105], Ag_2O [105], Y_2O_3 [105], Cr_2O_3 [105], ZrO_2 [112, 128], SiO_2 [101]
Metals	Au [102, 103, 129], Ag [103], Ni [101, 106, 118], Al [101, 106], Cu [106], Fe [106], Zn [101, 106], Sn [106], Mo [101], Ru [101], W [101], diamond [130]
Carbides, Sulfides, Borides	SiC [92, 131], WC [101], LaB_6 [101], MgB_2 [132], CdS [101, 133]
Phosphors	[101, 134, 135]
Other inorganic materials	LiCoO_2 [136], BaTiO_3 [137, 138], Clay [139], Zeolite [140], Glass [141], Cordierite [142], Hydroxyapatite [143, 144], $\text{La}_{0.8}\text{Sr}_{0.2}\text{Ga}_{0.875}\text{Mg}_{0.125}\text{O}_{3-x}$ [145]
Organic materials	Polymethylmethacrylate [146], Polyetheretherketone [147], polystyrene [148], polyimide [149, 150], poly(3-octadecylthiophene) [151, 152], poly(<i>p</i> -phenylene vinylene) [153], Fullerene [153, 154]

2.4.1 Coatings

EPD of coatings has already gained a world – wide acceptance in industry e.g. automotive or appliance plants [88 - 91]. For example, the construction and operation of an 800 bodies-per-hour cathaphoretic coating plant by a German car builder was described recently [91]. Current interest in the fabrication of wear and abrasion resistant coatings is focused on the developing of metal / ceramic and ceramic / ceramic composite coatings [88- 91]. EDP,

usually in combination with galvanic deposition of metals, is being used for the production of metal / ceramic composite coatings [155]. The availability of ceramic nanopowders in numerous compositions enables the use of EPD to prepare dielectric, magnetic, semiconducting and superconducting ceramic thick films for a variety of applications in electronic industry. Some recent significant developments include the fabrication of BaTiO₃ thick films for sensor or actuator applications [156], LiCoO₂ electrodes for rechargeable lithium batteries [136], Al₂O₃ or Pd-doped Al₂O₃ layers on SnO₂ for gas sensors [34], phosphor screens for information displays [134], photocatalytic titania coatings [123], MgO thick films for electronics [125, 126] and CdS films for solar cells [133]. Furthermore, the fabrication of superconducting MgB₂ films on different substrates was described [132]. Another area of application of EPD was in the biomedical field [143, 144].

2.4.2 Fibre reinforced ceramic matrix composites

The use of EPD for coating carbon and metallic fibres with alumina and titania nanopowders was described by Boccaccini *et al.* [157]. The coating of carbon fibres with hydroxyapatite was demonstrated by Zhitomirsky [158]. Lead zirconate titanate (PZT) films were deposited on Pt wires by Su *et al.* [159]. Membranes and porous materials have also been prepared by EPD techniques, including hydroxyapatite [143] and alumina [114].

EPD is a simple and cost – saving method for fabricating fibre reinforced ceramic matrix composites. In this application, EPD is used to infiltrate nanosized ceramic particles into two- or three- dimensional fibre architectures [90]. A recent comprehensive review article shows the great variety of conducting and non-conducting fibre and matrix combinations that have been explored, including SiC, carbon, and oxide ceramic fibre architectures and silica, borosilicate glass, alumina, zirconia, hydroxyapatite, SiC and Si₃N₄ [159]. Most recent work has been devoted to Ni-coated carbon fibre reinforced alumina [160], metal fibre reinforced cordierite matrix composites [142], borosilicate glass [161] and polyetherimide / carbon fibre composites [150].

2.4.3 Laminated and graded composites

EPD has been used to fabricate ceramic laminated composites and graded materials [91]. Put *et al.* manufactured graded WC-Co composites using a suspension of WC powder in acetone with variable Co powder content [120]. EPD was used to synthesize Al₂O₃ /

MoSi₂, Al₂O₃/Ni, Al₂O₃/YSZ and YSZ/Ni functionally graded materials [93]. Current efforts are devoted to the development of EPD fabrication approaches for laminated ceramic composites, in particular in the system ZrO₂/Al₂O₃, due to high fracture resistance of these structures [162].

2.4.4 Nanomaterials and nanostructures

EPD has been used to fabricate the layers of nanosized and nanostructured materials on different substrates [103, 116, 127, 129, 153, and 154].

Although the development of EPD techniques in this area is in the initial stage, results so far are encouraging and indicate great potentials for future R & D efforts.

Part III Theoretical background of semiconductor electrochemistry

3.1 Introduction

Semiconductor electrochemistry is an established branch of electrochemistry. Although many early reports existed of electrodes that exhibited semiconductor behaviour, the first paper on a well-defined semiconductor appeared in 1955 [163]. In this and subsequent papers the behaviour of germanium when it was polarized in aqueous electrolytes was described. In 1971 and 1972, Fujishima and Honda [163] reported that the water could be electrolyzed to oxygen and hydrogen in a simple cell using a platinum and a TiO₂ electrode. The electrolysis was supported by irradiation of the TiO₂ electrode with ultraviolet light and therefore the light energy was being converted to electrical energy. That report, combined with the public awareness of limited world energy resources, led to an explosion of papers on semiconductor liquid junction solar cells [163].

The early phases of solar energy conversion concentrated on the water splitting reaction using wide bandgap metal oxides (TiO₂, SrTiO₃, Fe₂O₃, SnO₂, In₂O₃ and WO₃). However, it was soon discovered that no semiconductor possessed all of the required properties for efficient photoelectrolysis, namely [163]: (i) an optimum bandgap of 1.5 to 2.0 eV, (ii) a conductor band edge more negative than the water reduction potential combined with a valence band edge more positive than the oxidation potential, (iii) rapid charge transfer kinetics to the electrolyte and (iv) extreme resistance to corrosion of the semiconductor surface.

Attention was turned to the regenerative semiconductor liquid junction solar cells. In these devices a reversible redox couple was oxidized at the semiconductor and reduced at metal electrode (n-type semiconductor) or vice versa (p-type semiconductor). Therefore, sunlight was converted to electrical energy with no net chemical change in the solar cell. The non-metal oxide semiconductors (Si, Ge, CdX, GaP, GaAs, InP) were tested in an effort to balance solar conversion efficiency with electrode stability [163]. Corrosion continued to be a problem. Major strategies for corrosion protection include [163]: (i) adsorbing or bonding of redox species to the semiconductor surface in order to collect the corrosion initiating minority carriers efficiently, (ii) changing from aqueous to nonaqueous electrolytes and (iii) isolating the semiconductor surface from the electrolyte with a metal or conducting polymer.

Although many books [74, 163, 164, 165, 166] are available on semiconductor electrochemistry in this chapter a brief description of the background of semiconductor electrochemistry will be given.

3.2. Fundamentals of semiconductor electrochemistry

3.2.1 Energy bands in solids and charge carrier generation

The properties of semiconductor electrodes and their differences from those of metallic electrodes can be understood by looking upon the electronic structures of these materials. Due to the large number of atoms interacting with each other, the electronic structure of these materials is typically discussed in terms of energy bands, which are built-up from the atomic orbitals of the individual atoms (Fig.3.1). As a result of the huge number of orbitals, the difference in energy between adjacent molecular orbitals is so small that the band can be effectively considered a continuum of energy levels. The highest and the lowest energy levels of a band are called the band edges. The energy bands of interest are the highest occupied (called valance band) and the lowest unoccupied (called conduction band). The energy gap between these bands determines the properties of the material.

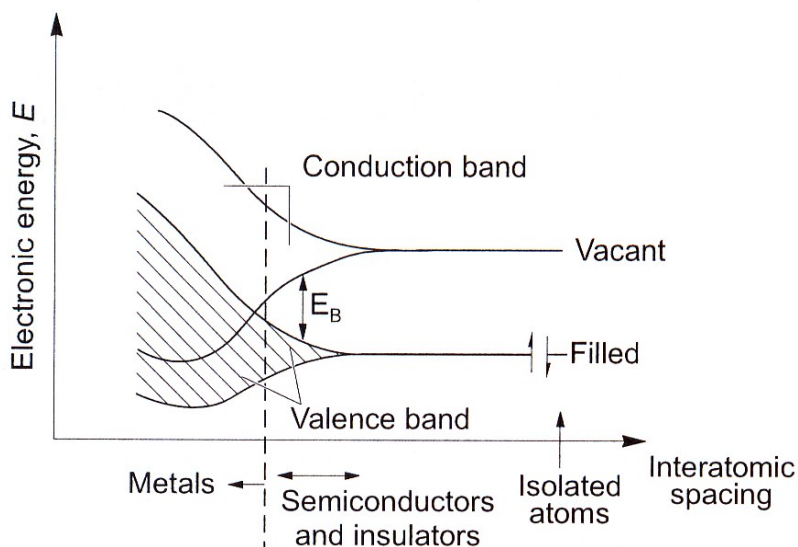


Fig.3.1 Generation of bands in solids from atomic orbitals of isolated atoms [167]

Conductivity of a solid material requires that the electrons occupy partially filled orbitals. This is achieved for metals, the conduction and valence band overlap (Fig.3.1). For nonmetallic materials valence and conduction band are separated by a bandgap. For insulators, the band gap is so large, that no electron can be excited from the valence band to the conduction band. However, for intrinsic semiconductors, the band gap is small and

electrons can be excited to the conduction band, leaving a positively charged position in the valence band which is referred to as a hole. Holes and electrons are mobile, and carry the current.

In intrinsic semiconductors, electrons can be excited to the conduction band either thermally or photochemically. Two charge carriers are generated: the electron in the conduction band and the hole, a positive vacancy in the valence band (Fig.3.2). Both are mobile within their respective energy bands. The concentration of electrons $[n]$ and holes $[p]$ depends on the absolute temperature and the band gap energy:

$$[n][p] = \text{const.} \exp(-E_g / kT) \quad (3.1)$$

When thermal generation is the only mechanism of charge carrier generation, as in an intrinsic semiconductor, then $[n] = [p]$. The total charge carrier concentration (and conductivity) drops rapidly with increasing E_g for a given temperature. At room temperature (25°C), kT is 0.0257 eV. Consequently, intrinsic semiconductors with bandgap energies greater than 0.5 eV are poor conductors.

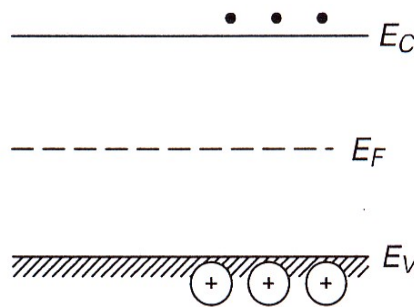


Fig.3.2 Schematic diagram of the energy levels of intrinsic semiconductor

For photoexcitation, a photon of light with energy greater than the band gap energy can excite an electron from the valence band to the conduction band. The newly created hole and the excited electron eventually recombine but they can be separated by means of electric field. The band gap energy controls the light absorption of the semiconductor. In terms of wavelength, light with wavelengths shorter than a threshold wavelength (λ_g) is absorbed to generate charge carriers, while light with longer wavelengths passes unimpeded through the semiconductor. Because λ is usually given in nm and the bandgap energy in eV the condition for adsorption is:

$$\lambda \leq 1240/E_g \quad (3.2)$$

A more subtle aspect of the light absorbing properties of semiconductors is the direct versus the indirect bandgap. In a direct bandgap semiconductor, a photon with energy just equal to the direct bandgap energy is absorbed with the creation of a hole and an electron. In an indirect bandgap semiconductor, the equivalent absorption process generates a hole, an electron and a phonon (a quantized lattice vibration with a fixed energy, in analogy to a photon). In many semiconductors the indirect transition lies at a lower energy than the direct one. The practical consequence is that the absorption coefficient rises less steeply with increasing photon energy for an indirect bandgap transition than for a direct one:

$$\alpha = \frac{A(h\nu - E_g)^{m/2}}{h\nu} \quad (3.3)$$

Where α is the absorption coefficient, $m = 1$ for a direct bandgap transition and $m = 4$ for an indirect one. Therefore, direct bandgap semiconductors are more efficient at absorbing sunlight near the electrode / electrolyte interface, an important property for thin film semiconductor liquid junction solar cells.

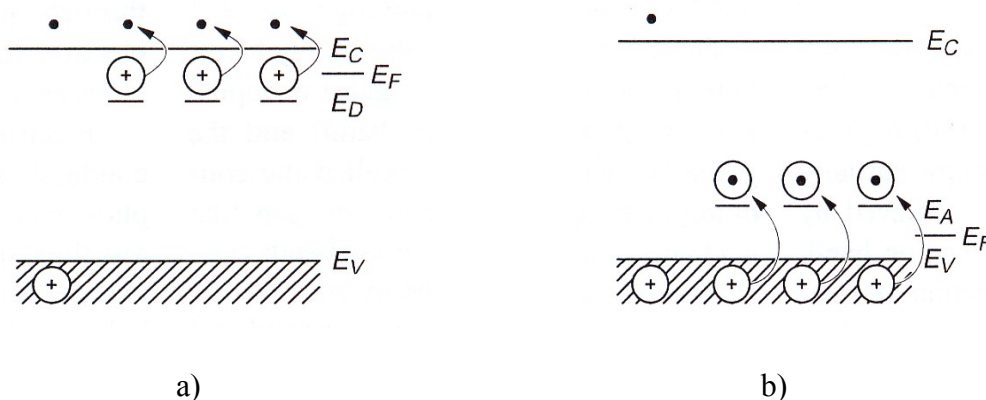


Fig.3.3 Schematic diagram of the energy levels of n-type semiconductor (a) and p-type semiconductor (b) [163]

However, there is another way for generating charge carriers (electrons or holes) in a semiconductor, called doping. Doping provides a means of enhancing conductivities of the wide bandgap semiconductors. Doping involves the addition of impurities to the semiconductor. A simple example is that the addition of a group V element or a group III element into a group IV element. The addition of P into Si adds occupied energy levels in the band gap close to the lower edge of the conduction band, thereby allowing the small excitation of the electrons into the conduction band (Fig.3.3a). Otherwise, the addition of B introduces vacant energy levels into the band gap close to the upper edge of the conduction band, which allows promotion of electrons from the valence band into these levels

(Fig.3.3b). This leads to the formation of holes in the valence band. Doped semiconductors, in which the main charge carriers are electrons, are referred to as n-type semiconductors (Fig.3.3a). Whereas, those in which holes are the majority charge carriers are called as p-type semiconductors (Fig.3.3b).

3.2.2 Fermi level and effect of applied potential

Another important concept in discussion of solid state materials is the Fermi level. The Fermi level is an extremely important parameter for metal and semiconductor electrochemistry because it is the property which is controlled by the externally applied potential. Thermodynamically, the Fermi level is the electrochemical potential of the electrons in the solid. An equivalent definition arises from the distribution of electrons among energy levels in a solid: the Fermi level is the energy at which the probability of occupation by an electron is $\frac{1}{2}$. For intrinsic semiconductors, the Fermi level lies at the mid-point of the band gap (Fig.3.2). Doping changes the distribution of electrons in the solid and hence changes the Fermi level. For an n-type semiconductor, the Fermi level lies just below the conduction band (Fig.3.3a), whereas for a p-type semiconductor, it lies just above the valence band (Fig.3.3b). In addition, the Fermi level of the semiconductor electrode varies with the applied potential. For example, moving to more negative potentials will shift up the Fermi level.

What happens at the interface of a semiconductor electrode and an electrolyte solution? In order for the equilibrium of two phases, their electrochemical potential must be the same. The electrochemical potential of the solution is the redox potential of the electrolyte solution and that of the semiconductor is determined by the Fermi level. If the redox potential of the solution and the Fermi level is different, a transfer of charge between the semiconductor and the solution is required in order to equilibrate these two phases. The excess charge in the semiconductor is not located at the surface as for a metallic electrode. It extends into the electrode for a significant distance (100-10,000 Å). This region is called as the space charge region and has an associated electrical field. Hence, there are two double layers to consider: the interfacial (electrode/electrolyte) double layer and the space charge double layer.

For an n-type semiconductor, at open circuit, the Fermi level is typically above the redox potential of the electrolyte; therefore, electrons will be transferred from the electrode into the solution. Hence, there is a positive charge associated with the space charge region and

this is reflected in an upward bending of the band edges (Fig.3.4a). The majority charge carrier of the semiconductor has been removed from this region so that this region is also referred to as the depletion region. For a p-type semiconductor, the Fermi level is usually below the redox potential of the electrolyte solution and the electrons move from the solution to the electrode to obtain the equilibrium. This generates a negative charge in the space charge region, which causes a downward bending of the band edges (Fig.3.4b). The density of holes in the space charge region is lowered so that this region is called again a depletion layer.

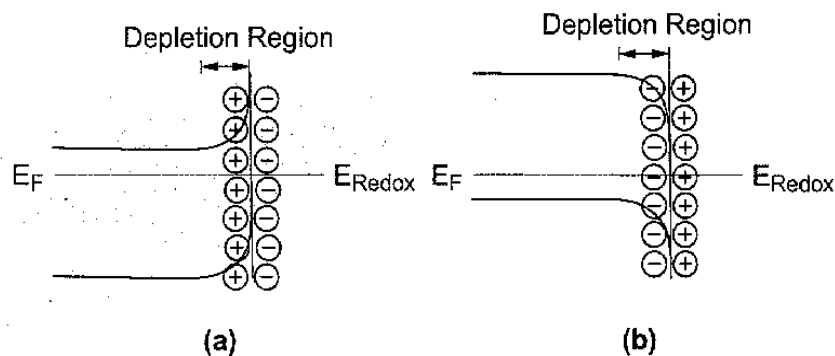


Fig.3.4 Band bending for an n-type semiconductor (a) and a p-type semiconductor (b) in equilibrium with an electrolyte

As for metallic electrodes, changing the potential applied to the electrode shifts the Fermi level. The band edges in the interior of semiconductor (outside the depletion region) also shift with the applied potential in the same manner as the Fermi level. However, the energy of the band edges at the interface are not affected by changes in the applied potential. Therefore, the change in the energies of the band edges on going from the interior of the semiconductor to the interface, and hence the change in the magnitude and direction of band bending, varies with the applied potential. There are three different situations to be discussed:

- i) At a certain potential, the Fermi energy lies at the same energy as the redox potential of the solution. There is no net transfer of charge, and hence there is no band bending. This potential is therefore called the flatband potential, E_{FB} (Fig.3.5b).
- ii) Depletion regions arise at potentials positive of the flatband potential for an n-type semiconductor and at potentials negative of the flatband potential for a p-type semiconductor (Fig.3.5a).

iii) At potentials negative of the flatband potential for an n-type semiconductor, there is an excess of the majority charge carriers (electrons) in the space charge region, which is referred to as an accumulation region. An accumulation region arises in a p-type semiconductor at potentials more positive than the flatband potential (Fig.3.5c).

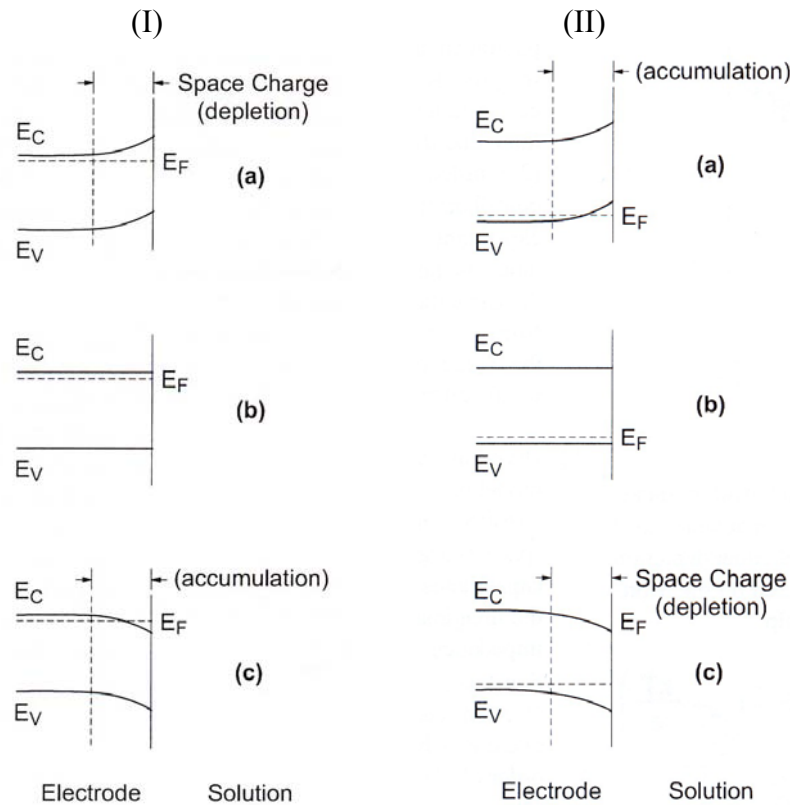


Fig.3.5 Effect of varying the applied potential on the band edges in the interior of an n-type semiconductor (I) and a p-type one (II): a) $E > E_{FB}$, b) $E = E_{FB}$, c) $E < E_{FB}$ [163]

The charge transfer ability of a semiconductor electrode depends on whether there is an accumulation layer or a depletion layer. If there is an accumulation, the behaviour of a semiconductor electrode is similar to that of a metallic electrode because there is an excess of the majority of charge carriers available for charge transfer. In contrast, if there is a depletion layer, then there are few charge carriers available for charge transfer and electron reaction occurs slowly.

3.2.3 Photoeffect at the semiconductor electrolyte interface

If the semiconductor electrode is exposed to radiation of sufficient energy, electrons can be promoted to the conduction band. If this process occurs in the interior of the semiconductor, there is recombination of the promoted electrons and the resulting holes with the production of heat. However, if it occurs in the space charge region, the electric

field in this region will cause the separation of the charge. For an n-type semiconductor at positive potentials, the band bending at the interface causes the holes to move towards the interface and the electrons to move to the interior of the semiconductor. The hole is a high energy species that can extract an electron from the solution. Therefore, the n-type semiconductor electrode acts as a photoanode. Using similar reasoning, it can be shown that p-type semiconductors are photocathodes.

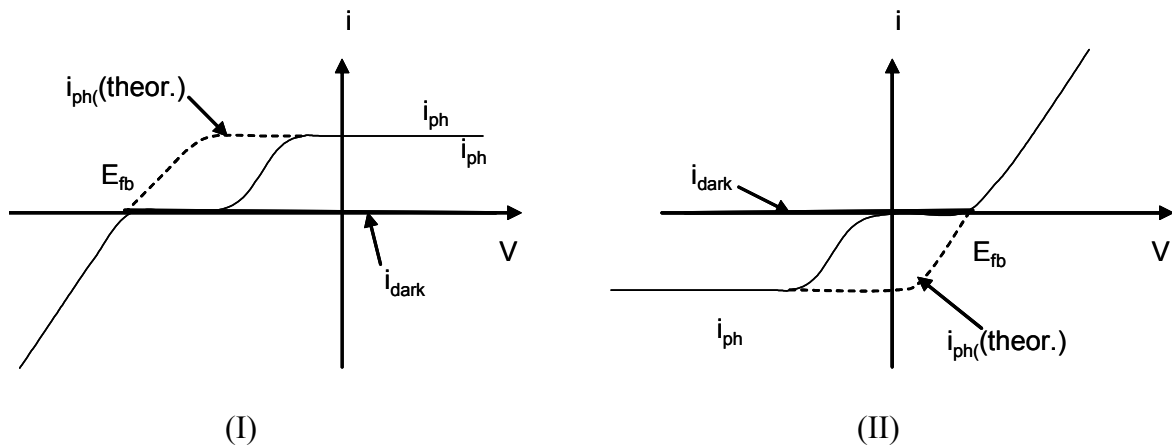


Fig.3.6 Current- potential characteristics for an n-type semiconductor (I) and a p-type semiconductor (II) in the dark and under irradiation [168]

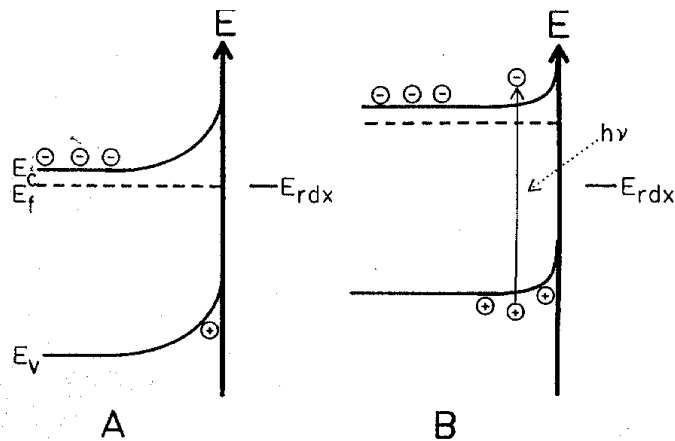


Fig.3.7 Photoeffect at an n-type semiconductor/electrolyte interface [163]:
 A) The semiconductor is equilibrated with a redox couple in the dark
 B) Under irradiation, the electrode potential shifts negative

When an n-type semiconductor electrode is biased sufficiently positive of E_{fb} , the dark currents are very low, due to the blocking effect of the depletion layer. Upon irradiation of the semiconductor through the electrolyte with the wavelength of the light $\lambda < \lambda_g$, anodic photocurrents appear (Fig.3.6). These photocurrents arise from the flux of the holes (minority carriers) arriving at the electrode surface. After light absorption generates an

electron-hole pair in the depletion layer, the electric field in the depletion layer separates the two charge carriers, with the electron moving toward the bulk of the electrode and the hole migrating toward the surface (Fig.3.7). Electron-hole pairs generated beyond the depletion layer also partially diffuse in the electric field and become separated. The holes have an oxidizing power roughly equivalent to the potential of the valence band edge and are capable of oxidizing molecules whose formal redox potential is below E_v . In the wide bandgap material (e.g. TiO_2), the electrolyte (H_2O) is oxidized. The electron in the conduction band flows via an external circuit to another electrode where reduction takes place.

The shape of the photocurrent voltammograms depends on the energy distribution of the incident photons, the absorption of the semiconductor, the diffusion distance of the excited holes and electrons and the recombination rates. The simplest situation arises when the incident photons are absorbed in the depletion layer. Then the excited charge carriers are separated with minimum recombination. In the absence of mass transfer limitations imposed by the supply of hole acceptors, photocurrent quantum efficiencies (electrons obtained per photons absorbed) approach unity. As long as the depletion layer thickness exceeds the depth of charge carrier generation, then photocurrent quantum efficiencies are independent of the applied potential therefore the photocurrent approaches to plateau as in Fig.3.6. When the applied potential approaches E_{fb} , the space charge layer thickness decreases. Recombination rates increase because the holes and electrons are no longer being separated by the electric field. The photocurrent drops sharply and merges with the dark current near E_{fb} . At potential negative of E_{fb} the electrode is no longer blocking so the dark current increases dramatically.

A number of theories have been formulated to account for the shape of the photocurrent voltammograms. A relatively simple equation has been derived assuming the absence of any recombination in the space charge layer [163]:

$$J_p = eI_0 \left[\frac{1 - \exp(-\alpha W_d)}{(1 + \alpha L)} \right] \quad (3.4)$$

J_p is the photocurrent density, I_0 is the flux entering the semiconductor, α is the absorption coefficient; W_d the width of depletion layer and L is the diffusion length for minority carriers. In Eq.3.4, the width of depletion layer is calculated by the following equation [163]:

$$W_d = \sqrt{\frac{2\epsilon\epsilon_0(E - E_{fb})}{eN_D}} \quad (3.5)$$

Butler [163] showed how to manipulate the linear plot for the estimation of E_{fb} , E_g . The key is to choose photon energies that are strongly absorbed by the semiconductor (i.e. λ near λ_g). Then the light penetrates to a depth considerable greater than the depletion layer. With $\alpha W \ll 1$ and $\alpha L \ll 1$, Eq. (3.4) can be transformed into [163]:

$$J_p = \frac{eI_0 \cdot A(L + W)(h\nu - E_g)^{m/2}}{h\nu} \quad (3.6)$$

A plot of $\log[(J_p \cdot h\nu)/(eI_0)]$ vs. $\log(h\nu - E_g)$ at constant potential yields a straight line whose slope should be either $\frac{1}{2}$ ($m = 1$, direct bandgap) or 2 ($m = 4$, indirect bandgap). Alternatively, a plot of $[(J_p \cdot h\nu)/(eI_0)]^{2/m}$ vs. $h\nu$ has an ordinate intercept of E_g . Hence, bulk optical properties of new semiconductor electrode materials can be characterized by photoelectrochemical measurements.

3.2.4 Determination of flatband potential

The flatband potential is one of the most important experimental parameters to be determined for a semiconductor electrode. The position of the band edges on the electrochemical scale, the direction of the band bending and in favourable cases the magnitude of the band bending are related to E_{fb} . There are two methods for determining E_{fb} .

3.2.4.1 Mott-Schottky plot

One of the most common methods is the Mott-Schottky plot. It is based on the capacitance associated with the space charge layer. Each of the regions around the electrode / electrolyte interface (the diffuse layer, the Helmholtz layer and the space charge layer) are planes of charge separated by distance and hence have associated capacitances. The three capacitances are in series so the smallest one dominates the total capacitance. In concentrated electrolytes the diffuse capacitance is so large that it can be completely ignored. The Helmholtz capacitance is in the range of $10 - 100 \mu\text{F}/\text{cm}^2$. Thus when the measured capacitance is small relative to this number, then it can be assigned to the space charge layer (C_{SC}). In the depletion region, the space charge capacitance varies with the

width of the space charge layer, which in turn is a function of the potential relative to E_{fb} . The Mott-Schottky equation incorporates these factors in a convenient linear form [163]:

$$\frac{1}{C_{SC}^2} = \frac{2}{e \cdot \epsilon_0 \cdot \epsilon \cdot N_D} \left(E - E_{fb} - \frac{kT}{e} \right) \quad (3.7)$$

where C_{SC} is the capacitance of the space charge region, ϵ is the dielectric constant of the semiconductor, ϵ_0 is the permittivity of free space, N_D is the donor density and E is the applied potential. The donor density can be calculated from the slope, and the flatband potential can be determined by extrapolation to $C = 0$. The capacitance values are obtained by impedance measurements. The equivalent circuit used in this model is a series combination of a resistance and a capacitance (the space charge capacitance). The capacitance is calculated from the imaginary component of the impedance (Z'') using the relationship $Z'' = 1/(2\pi \cdot f \cdot C)$. The resistance is the electrolyte resistance. The model is adequate provided there is a negligible charge transfer and otherwise the complete impedance spectrum must be evaluated the frequency is high enough (on the order of kHz).

3.2.4.2 Photocurrent onset potential

As shown in Fig.3.5, the photocurrent merges with the dark current near E_{fb} . The photocurrent onset potential, V_{on} , is often considered as the flatband potential. At the flatband potential the space charge layer width goes to zero. Eq.3.4 predicts a non-zero photocurrent at E_{fb} as photogenerated minority carriers diffuse to the electrode surface in the absence of an electric field. However, recombination always suppresses the photocurrent, especially in the vicinity of E_{fb} . Thus V_{on} tends to be positive of E_{fb} for n-type semiconductors and negative of E_{fb} for p-type semiconductors. Butler [163] described an extrapolation procedure based on Eq.3.4. The incident photon energy is tuned to a value near E_g where the absorption coefficient is small. Then photocurrent becomes proportional to the thickness of the space charge layer (Eq.3.5). Combining these results yields:

$$J_p^2 = (2q \cdot \epsilon \cdot \epsilon_0 \cdot I_0^2 \cdot \alpha^2 / N_d) (E - E_{fb}) \quad (3.8)$$

A plot of the square of the photocurrent vs. the applied potential produces a straight line with intercept E_{fb} .

The behaviour discussed above applies only to an idealized semiconductor / electrolyte interface. In real systems, there are a number of factors that can give rise to anomalous

behaviour. The main cause of non-ideal behaviour is photodecomposition of the electrode. That is oxidation of the electrode itself by holes in the depletion region. This can be avoided by the addition of appropriate electroactive species to the solution that competes with the auto-oxidation or by the stabilization of the electrode surface by chemical modification.

Part IV Experimental procedures

4.1 Reagents and solvents

4.1.1 Reagents

- Monomers: Thiophene (99 + %) and methylthiophene (98%) were purchased from Aldrich and were distilled before use.

- Oxides: TiO₂ (P25, 21 nm), Al₂O₃(C) (13 nm) and SiO₂ (Aerosil 380, 7 nm) were obtained from Degussa. Al₂O₃(D) and ZnO (several to hundred nanometers determined by scanning electron microscopy) were supplied from Chemiewerk Greiz-Dörlau and Merck, respectively. All oxides were heated at 80⁰C for several hours before use.

- Oxidant: FeCl₃ (free of water) purchased from Fluka was used as received.

4.1.2 Solvents

- Chloroform (water-free, LiChrosolv) and acetonitrile (99.9 + %) were supplied from Merck and Fischer, respectively.

- Ethanol (3.4 % water) and isopropanol (95 %) were obtained from Berkel AHK. Glycerol (98 %), butanol (99 %), ethylacetate (90 %) and methanol (95 %) were purchased from Merck, Acros, Biesterfeld and Bielac, respectively. All solvents were used as received.

4.1.3 Other chemicals

- Poly (3-octylthiophene) (98 %) was obtained from Aldrich.

- Supporting electrolyte: LiClO₄ (98 + %) was purchased from Fluka.

4.2 Preparation of nanocomposites

Composites were prepared following a procedure described in Ref. [169]. About 20 g oxide powder (dried at above 100⁰C for 2 - 4 hours) was dispersed with 200 µl thiophene in 200 - 400 ml CHCl₃ depending on the type of oxide. A second dispersion was made of 2.0 – 3.0 g FeCl₃ in 50 ml CHCl₃. The FeCl₃ dispersion was added to the oxide particle dispersion under stirring. The colour of the mixture of the two dispersions was changed from grey to black. Oxidized PTh shells covered the oxide particles. After stirring, the particles were filtered and dried. The iron chloride was extracted with methanol for several hours. During

this procedure, the colour of the composite changed from grey blue (PTh in oxidized state) to red (PTh in reduced state). The composite was dried at 60-80⁰C for 2–3 hours. The PTh content was around 1 % (by weight) in all prepared composites as determined by thermogravimetric analysis. The preparation of nanocomposites is schematically shown in Fig.4.1.

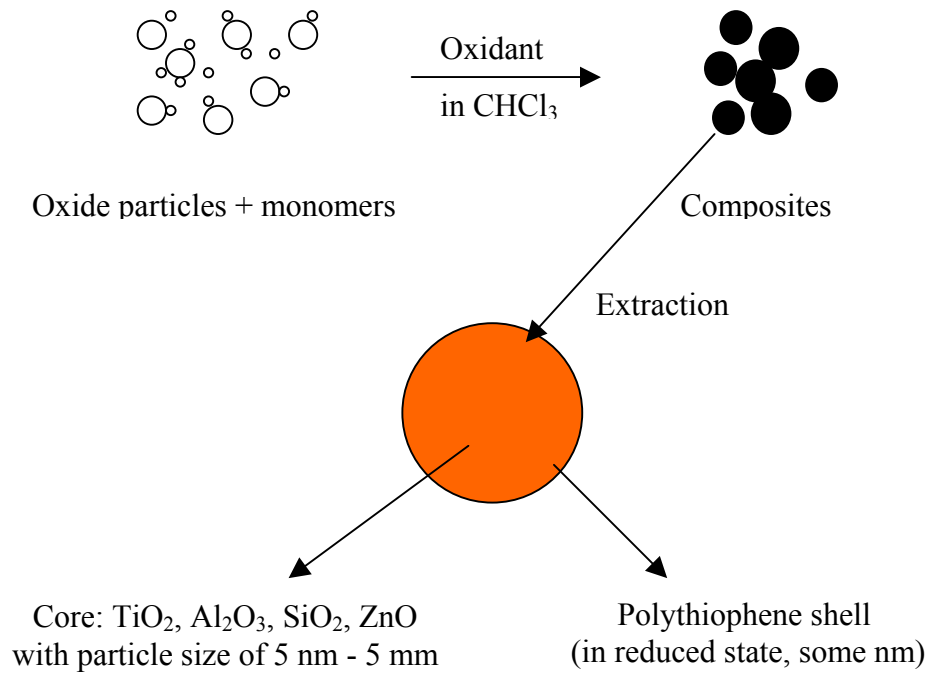


Fig.4.1 Preparation of nanocomposites

4.3 Morphology and chemical characterization of nanocomposites

The morphology of the obtained composite particles was studied by scanning electron microscopy, SEM and transition electron microscopy, TEM. The SEM picture was measured by the Zeiss DSM 982 Gemini and TEM pictures were measured with the Philips CM 200. In addition, the surface of the deposited layers was controlled by optical microscopy (Reichert, Austria).

The chemical characterization of the composites was made by Raman spectroscopy, recorded on the DILOR LabRAM 010 system equipped with 15 mW He-Ne and CCD detector.

4.4 Dark conductivity and thermogravimetical measurements

The dark conductivity of nanocomposites was measured on press-pellet samples at 300 K using the van der Pauw method with four Au electrodes, vacuum deposited on the

perimeter of the pellets. The amount of conducting polymers in the composites was calculated from the data of the thermogravimetical measurements (performed with a thermobalance, METTLER TG 50).

4.5 Properties of suspension

About 0.5 g of the composite material was homogenized in 100 ml organic solvent by an ultrasonic bath for several minutes to form a suspension. Suspensions of core-shell nanocomposites in methanol, glycerol, propanol and ethylacetate were stable for more than seven days.

Conductivity of suspensions in different conditions was measured by a Konductometer 703 (Knick). The absorption spectra of suspensions were measured by a UV Spectroscope 2000 (Shimadzu) at ambient condition.

For the zeta potential measurements the Zetasizer 2000 (Malvern Instruments) with a combination of electrophoresis and Laser - Doppler - Anemometry was used.

4.6 Electrophoretic deposition

The EPD was carried out in a two-electrode cell using a DC power source (0-150 V, 3 A, Philips-PE 1527). The current was recorded with a multimeter (Keithley 175). The EPD was carried out at ambient condition (room temperature and atmospheric pressure). The dispersion was stirred during deposition. Different substrates (mild steel, aluminium, platinum, ITO glass plates) and different organic solvents (ethanol, ethylacetate and glycerol) were tested.

To study the kinetics of the EPD, a combined experimental arrangement of EPD and a quartz crystal microbalance (QCM) was developed (Fig.4.2). Commercially available 10 MHz AT-cut quartz crystals were used for all experiments. Both sides of the quartz crystal were covered with a gold electrode. The quartz crystals were installed in a Teflon cell so that only an area of 0.22 cm² was exposed to the colloidal suspension. The oscillating frequency was measured with a network analyzer (Guide Technologies GT 200). The ethanol colloidal suspension of PTh/TiO₂ (0.5 g/l) was used for QCM measurement.

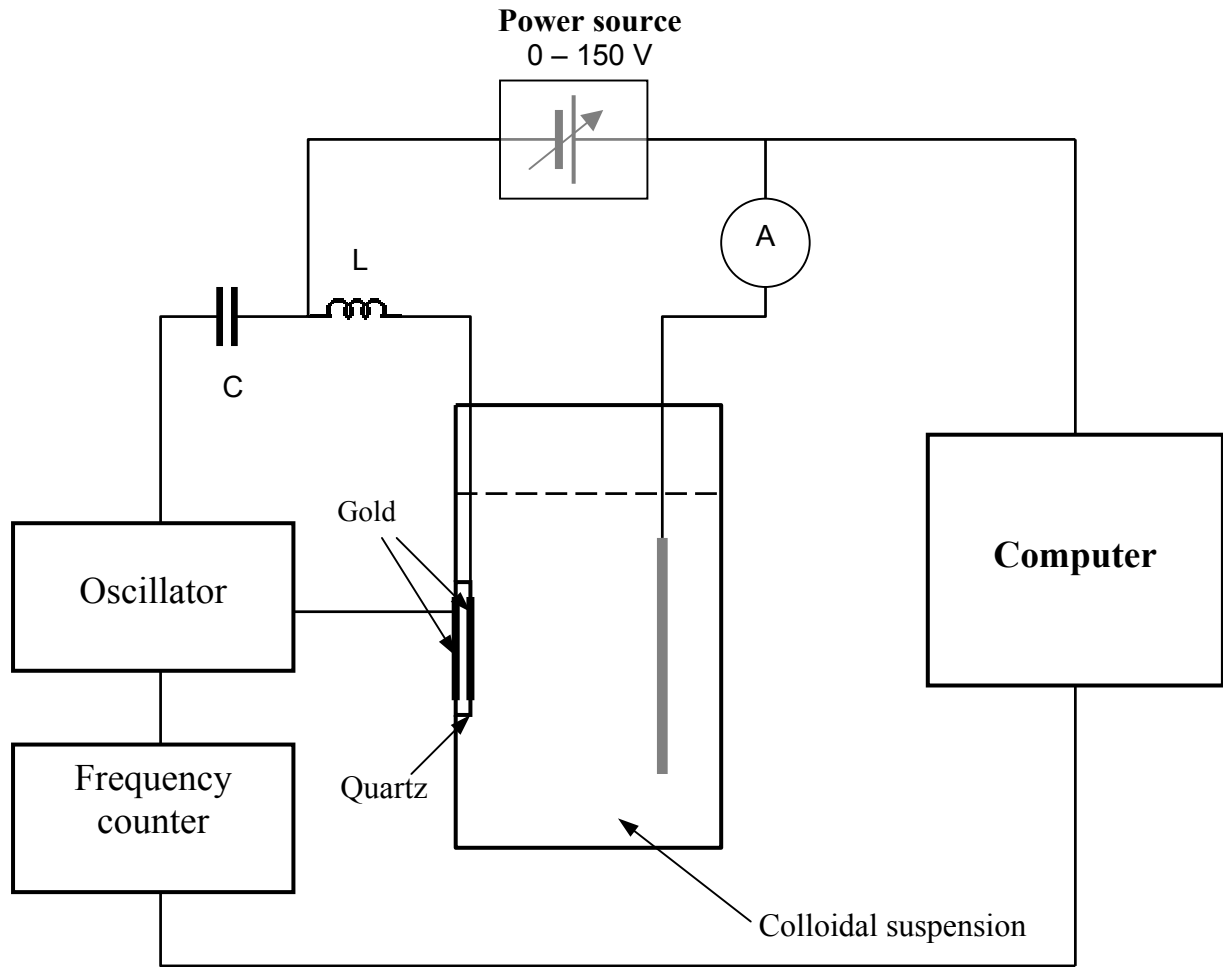


Fig.4.2. Schematic cell arrangement of the EPD combined with QCM

Although QCM is a generally used method to study the electrochemical deposition of various materials [170, 171], until now it has not been applied for in-situ studies of EPD. During EPD, the frequency of the quartz was decreased according to the Sauerbrey equation [170, 172]:

$$\Delta f = -2\Delta m \cdot n \cdot f_0^2 / A(\mu_q \rho_q)^{1/2} \quad (4.1)$$

A is the area of the gold electrode, μ_q is the shear modulus of the quartz, ρ_q is the density of the quartz, Δf is the frequency change, Δm is the mass increment, n is the electron stoichiometry. Summarizing all constants into k one obtains:

$$\Delta f = -k\Delta m \quad (4.2)$$

k is called the sensitivity factor.

4.7 Characterizations of resulting films

4.7.1 UV-VIS spectra

The optical absorption spectra of pressed pellets prepared from composite powders and composite films deposited on ITO substrates were measured using Perkin Elmer 340 spectrophotometer with diffusion reflexion technique.

4.7.2 Photocurrent measurements

Photocurrent measurements of the semiconducting / oxide composites were performed using lock-in technique [173]. The equipment is shown in Fig.4.3.

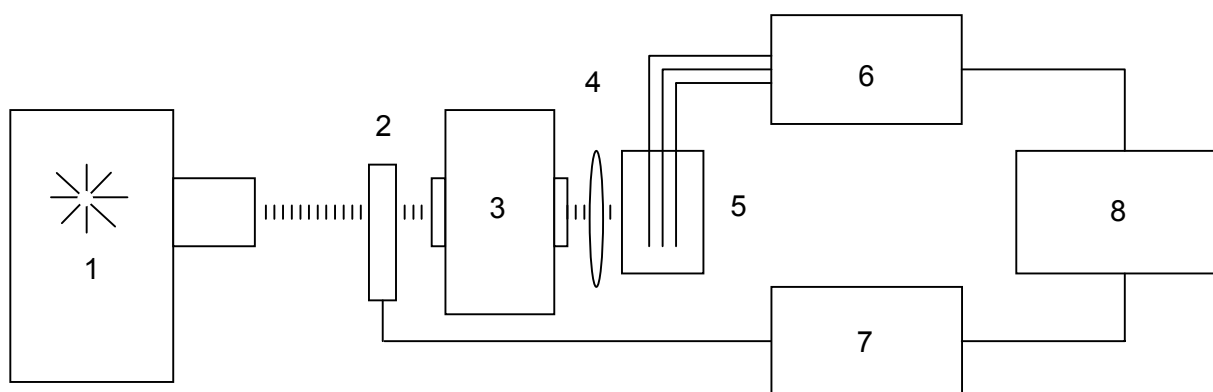


Fig.4.3. Schematic arrangement for photocurrent measurements using lock-in technique
1) Light source 2) Chopper 3) Monochromator 4) Lens
5) Electrochemical cell 6) Potentiostat 7) Lock-in 8) Out-put

The light was chopped by a chopper (2, PAR 197) for a periodic modulation of light intensity. A frequency of 400 Hz was used for the chopper. With a monochromator (3, Zeiss, aperture $a = 0.5$), the light of suitable wavelength (range 250-1000 nm) was selected from a UV lamp (1, Müller-Elektronik, $P = 1000$ W) to illuminate the working electrode. The photocurrent signal with relatively small amplitude (nA- μ A) was registered by a Lock-in amplifier (7) and a phase sensitive rectifier. A quartz glass collecting lens (4) focussed the light. The electrochemical equipment consisted of the potentiostat (6, HEKA D 6734 Potentiostat –Galvanostat). Small and stable basic currents (1 μ A – 10 μ A) could be obtained by deoxygenation of the electrolyte because in case of the cathodic polarisation of the working electrode (producing a depletion layer in the p-type semiconducting polymer), a rather high reduction current is occurred from very small amounts of dissolved oxygen in

the electrolyte. The time constant of the photocurrent measurements was set to 3 s on the lock-in amplifier. The wavelength range was switched in steps of 50 nm, as well as 10 nm or 5 nm in the spectral range of 300-800 nm.

4.7.3 Photoelectrical and electrical characteristics

For the photoelectrical and electrical measurements, the samples were prepared as described in Fig.4.4.

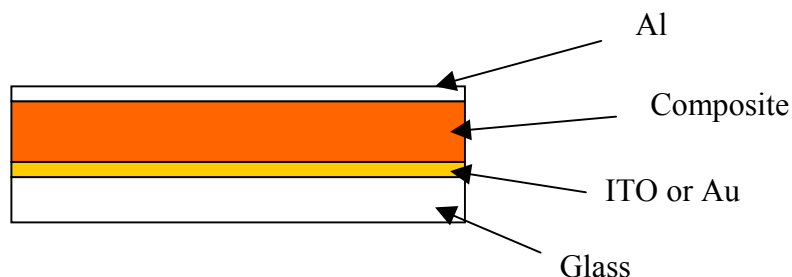


Fig.4.4 Sandwich structure of the sample under study

The photoelectrical measurements (in this case, ITO was used) were made under steady state illumination conditions using a Xenon lamp (Müller-Elektronik, P = 75 W) and a Jobin Yvon H25 monochromator, with the photodiode (EG&G HUV-1100 B) in the reference beam, in the serial connection of the sample, power supply (Keithley 230) and electrometer (Keithley 617). The electrical measurements were made with an electrometer Keithley 236 and a Xenon lamp (Müller-Elektronik, P = 150 W). In this case an Au electrode was used.

4.7.4 Cyclic voltammetry

Cyclic voltammograms (CV) of the deposited composite layers on platinum were made with EG & G potentiostat model 264 A. Platinum sheets were used as counter electrodes. The saturated calomel electrode (SCE) was used as a reference electrode. The CV curves of the composite layers were measured in CH₃CN containing 0.5 M LiClO₄ with a scan rate of 10 mV/s between 0 and 0.9 V_{SCE}.

4.7.5 Electrochemical impedance spectroscopy [174, 175]

When a sinusoidal voltage is applied across the electrode / electrolyte interface

$$E_t = E_m \sin(\omega t + \varphi_E) \quad (4.3)$$

where E_t is the potential at time t , E_m is the amplitude of applied potential, ω is the frequency ($\omega = 2\pi f$, in radians), then the corresponding current is given by:

$$I_t = I_m \sin(\omega t + \varphi_I) \quad (4.4)$$

With a phase shift $\varphi = \varphi_E - \varphi_I$ is observed. For further calculation, E_t and I_t can be written as complex numbers.

$$E_{t,\omega} = E_m \exp[j(\omega t + \varphi_E)] \quad (4.5)$$

$$I_{t,\omega} = I_m \exp[j(\omega t + \varphi_I)] \quad (4.6)$$

From (4.3) and (4.4), impedance Z is defined as:

$$Z(j\omega) = \frac{E_m \sin(\omega t + \varphi_E)}{I_m \sin(\omega t + \varphi_I)} = Z_m \exp(j\varphi) \quad (4.7)$$

It is composed of a real (Z') and an imaginary part (Z''):

$$Z(j\omega) = Z' + jZ'' \quad (4.8)$$

This is illustrated in Fig.4.5.

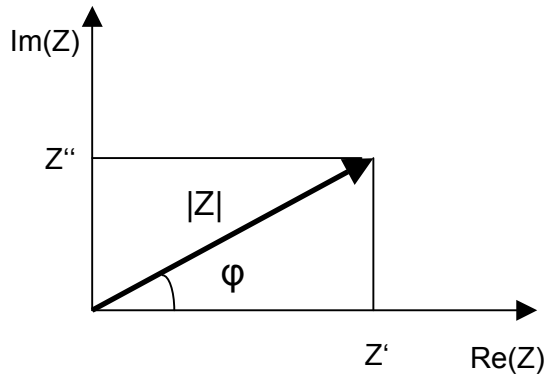


Fig.4.5 Imaginary and real part of impedance
a

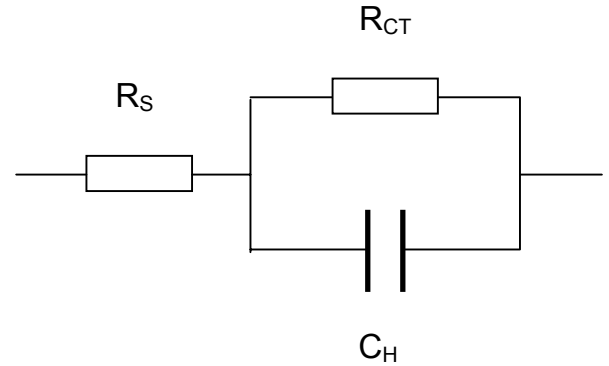


Fig.4.6 Equivalent circuit for simple electrochemical system

In the simplest case the solid – liquid interface can be described by a charge transfer resistance R_{CT} and a capacitance in parallel (Helmholtz capacitance for metal electrodes, C_H and a space charge capacitance for semiconductor electrodes, C_{SC}). A resistance R_s takes into accounts the resistance in the electrolyte or other Ohmic components (Fig.4.6).

$|Z|$ and φ are defined by:

$$|Z| = \sqrt{(Z')^2 + (jZ'')^2} \quad (4.9)$$

$$\tan \varphi = \frac{Z''}{Z'} \quad (4.10)$$

The Bode plot (Fig.4.7) has some advantages over the plot in Fig.4.5. Since frequency appears as one of the axes, it is easy to understand from the plot how the impedance depends on the frequency. The plot uses the logarithm of frequency to allow a very wide frequency range to be plotted. The Bode plot also shows the magnitude ($|Z|$) on a log axis so that it is easy to plot wide impedance ranges on the same set of axes.

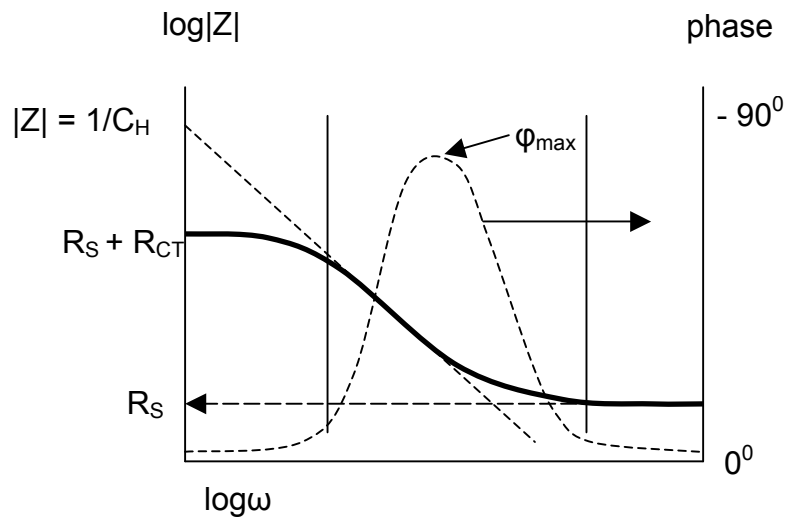


Fig.4.7 Bode plot for a simple electrochemical system

The $\log |Z|$ vs. $\log \omega$ curve can be used to determine values of R_S and R_{CT} . At the highest frequencies shown in Fig.4.7, the Ohmic resistance dominates the impedance and $\log R_S$ can be read from the high frequency horizontal plateau. At the lowest frequencies, R_{CT} also contributes, and $\log(R_{CT} + R_S)$ can be read from the low frequency horizontal plateau. At intermediate frequencies, this curve should be a straight line with a slope of -1. Extrapolating this line to the $\log |Z|$ axis at $\omega = 1$ ($\log \omega = 0$) yields the value of C_H from the relationship:

$$|Z| = 1/C_H \quad (4.11)$$

The Bode plot also shows the phase angle, φ . At the high and low frequency limits, the phase angle is nearly zero. At the intermediate frequencies, the phase angle increases as the imaginary component of the impedance increases.

Although the simple equivalent circuit can be relatively straightforwardly analyzed, typical electrochemical systems yield more complicated plots. These complexities arise because

the simple equivalent circuits do not fully describe the physical phenomena of an electrochemical system. The simple equivalent circuit models are frequently good approximations of real systems and the data can often be fitted to yield results of reasonable accuracy.

In this study, EIS were recorded with the IMd5 system (Zahner-Elektrik). The composite layers deposited on a platinum plate were used as a working electrode. Platinum was used as a counter-electrode and the saturated calomel electrode (SCE) was used as a reference electrode. Impedance spectra of the deposited composite layer were measured in the potential range between 0 and 1.0 V (*vs.* SCE) in steps of 50 mV. Each measurement took 30 min. The electrolyte was 0.5 M LiClO₄/CH₃CN.

Part V Results and discussion

5.1 Morphology and chemical characterization of nanocomposites

5.1.1 Morphology of nanocomposite particles

The morphology of the obtained composite particles was investigated by SEM and TEM techniques. A SEM micrograph of the surface of a pressed pellet, made from TiO₂ (P25) covered by PTh (in reduced state), is shown in Fig.5.1. The average size of the composite particle was around 30 nm while the average TiO₂ particle size was only 21 nm. This indicates that the surface of the TiO₂ particles was covered by a PTh shell of 4.5 nm thickness. However, the average size was 23-27 nm showing that the coverage was not regular and the composite particles were not fully covered by PTh.

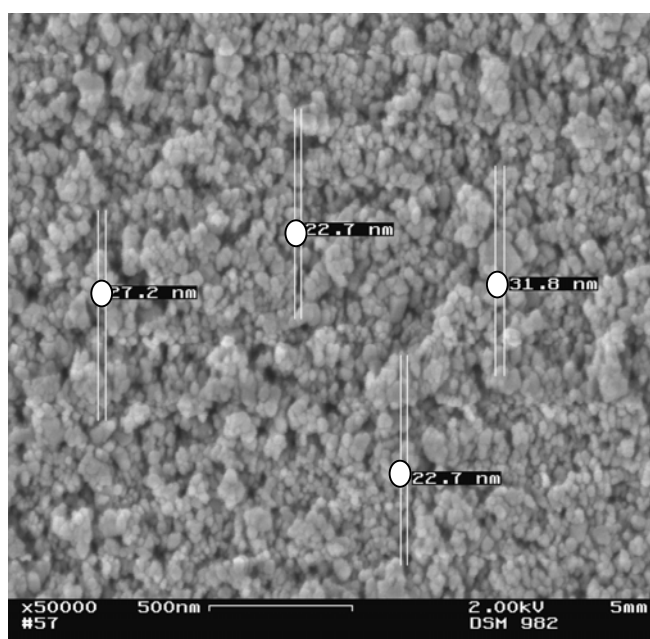


Fig.5.1 SEM-micrograph of pressed PTh/TiO₂ composite pellet, magnification: 30,000

In Fig.5.2, the TEM micrograph of a single nanocomposite particle is presented. The clearly visible diffraction pattern represents the anatase modification of TiO₂. The lighter non-patterned cloud on the left-hand side of the oxide core belongs to the PTh shell. It is several nanometres thick. The structure relatively well corresponds to the theoretical calculation, predicting 4-5 nm thick polymer shells. In reality, the coverage of the oxide is complicated by aggregation of the oxide particles before and during the polymerization, and the composite is to be contaminated by granules of pure polymer formed in the bulk of

the solution. Nonetheless, the TEM observation gave the direct evidence that the covering of TiO_2 via oxidative polymerization of thiophene is in principal possible.

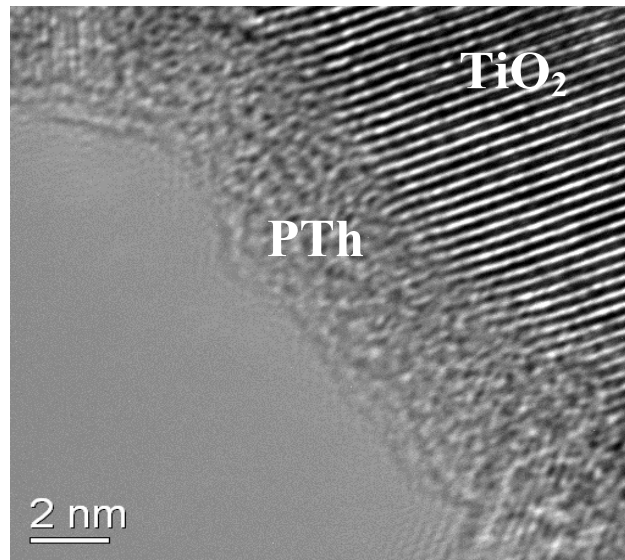


Fig.5.2 TEM-micrograph of TiO_2 covered with reduced PTh, magnification: 1.100.000

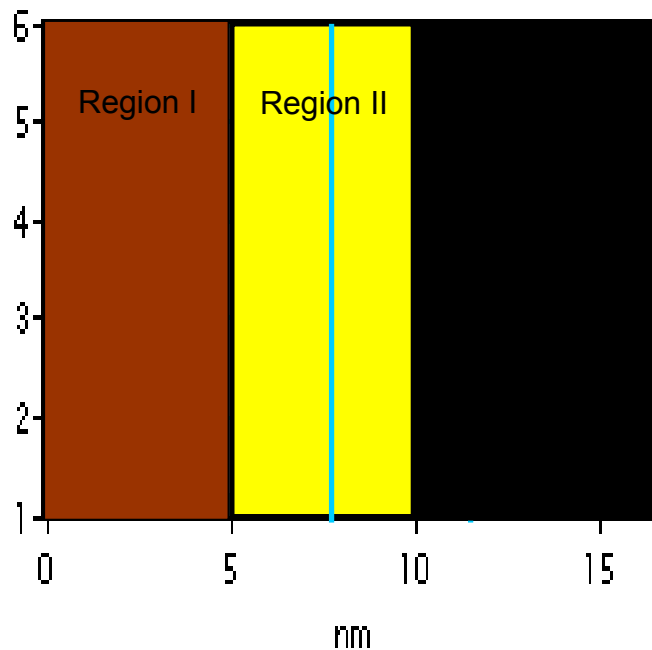


Fig.5.3 Electron density in the PTh/ TiO_2 nanocomposite particle

The holographic technique of the SEM measurements showed the electron density of the TiO_2 nanoparticle and PT shell (Fig.5.3). In this technique, the phase shift of the electron beam was caused by the interaction of the electron within the semiconductors. Therefore, the electron density in the semiconductors could be observed. The region (I) shows the electron density of the PTh shell. The thickness of this region is 5 nm, in agreement with the result presented in Fig.5.2. The region (III) shows the electron density of the TiO_2 core.

Obviously, the electron density of the n-type semiconductor (TiO_2) is higher than that of the p-type semiconductor (PTh). The region (II) shows the p/n heterojunction in the boundary of the TiO_2 core and the PTh shell. The width of the p/n heterojunction was 5 nm (Fig.5.3).

5.1.2 Chemical characterization of the nanocomposites

Fig.5.4 shows Raman spectra of the reduced and oxidized PTh/ TiO_2 composites. The assignments of the Raman bands of PTh in the composites, listed in Tab.5.1 (both oxidized state and reduced state of PTh), are in agreement with previous reports [176, 177]. In the oxidized state, the peak at 1420 cm^{-1} has been attributed to the quinoid units (radical cations). On the other hand, in reduced state this peak disappeared and a new peak at 1455 cm^{-1} was found, attributed to the $\text{C}_\alpha=\text{C}_\beta$ ring stretching of the neutral PTh.

The bipolaron absorption, proposed to be at 1400 cm^{-1} in the oxidized state [176] was not observed while the peak at 1420 cm^{-1} was found, supporting that the oxidized PTh is mainly a radical cation. This is in agreement with the results presented in Ref. [176] and the schematic representation for the state change of PTh (Fig.5.5).

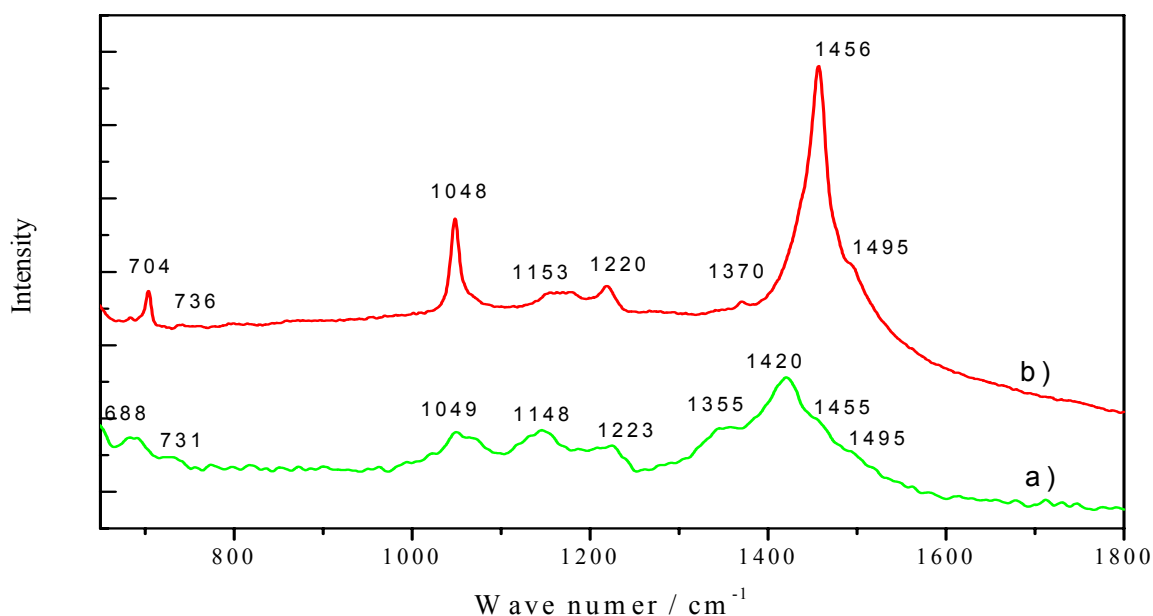


Fig.5.4 Raman spectra of PTh/ TiO_2 composite
a) oxidized state and b) reduced state

The band of $\text{C}_\beta\text{-H}$ bending (in oxidized state) appears at 1049 cm^{-1} . This band showed a little shift to lower frequency [176]. The second band of C-S-C deformation (704 cm^{-1}) in

the reduced PTh shifts positively (vs. 693 cm^{-1} [176]), while that in the oxidized state (688 cm^{-1}) shifts negatively (vs. 693 cm^{-1} [176]). An additional small peak at 1463 cm^{-1} (in the oxidized PTh) could not be attributed.

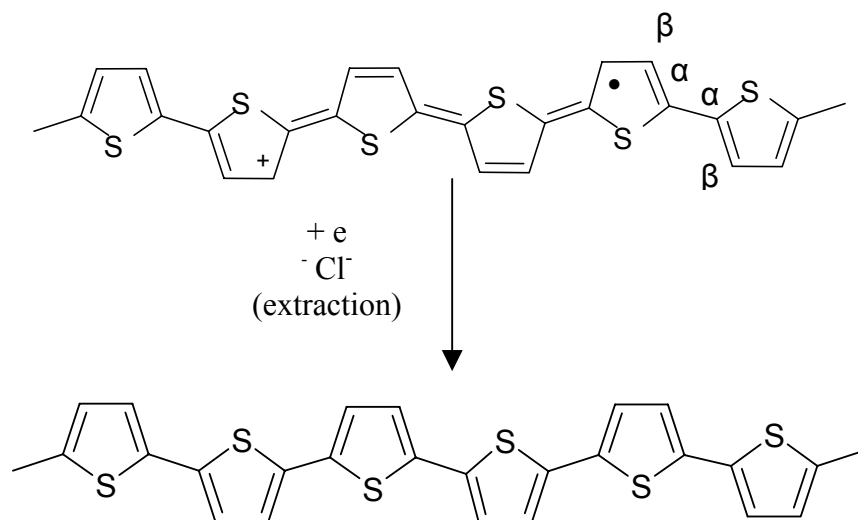


Fig.5.5 Structure of the neutral and oxidized polythiophene during extraction

Tab.5.1 Band assignment of the Raman spectra of PTh in the PTh/TiO₂ composites

Assignments	Reduced polythiophene		Oxidized polythiophene	
	Experimental	Literature	Experimental	Literature
C _α =C _β ring stretching (anti)	1495	1495 (*) 1499 (**)	1495	1495 (*)
C _α =C _β ring stretching	1456	1455 (*) 1458 (**)	1455	1455 (*)
quinoid (radical cations)	-	-	1420	1420 (*)
C _β -C _{β'} ring stretching	1370	1370 (*)	1355	1355 (*)
C _α -C _{α'} stretching	1220	1221 (*)	1223	1223 (*)
C _β -H bending	1048	1045 (*) 1048 (**)	1049	1056 (*)
C _α -C _{α'} stretching (anti)	1153	1153 (*)	1148	1151 (*)
ring deformation	736	736 (*) 707 (**)	731	729 (*)
C-S-C	704	693 (*)	688	693 (*)

(*) Polythiophene prepared by electropolymerization on stainless steel [176]

(**) Polythiophene prepared by chemicalpolymerization on silicon using 11-(3-thienyl) undecyltrichrosilan as adhesion promoter [177]

5.2 Electrophoretic deposition

5.2.1 Properties of suspensions

5.2.1.1 Conductivity of suspensions

As shown in Fig.5.6, the conductivities of suspensions in ethanol (96 %) and in butanol increased when the concentration increased. This increase proved that the composite particles were charge carriers. But this increase was not linear. This was explained by particle coagulation. In the case of butanol, for concentrations higher than 3 g.l⁻¹, the conductivity was constant (Fig.5.6). When the temperature increased the conductivity also increased as shown in Fig.5.6.

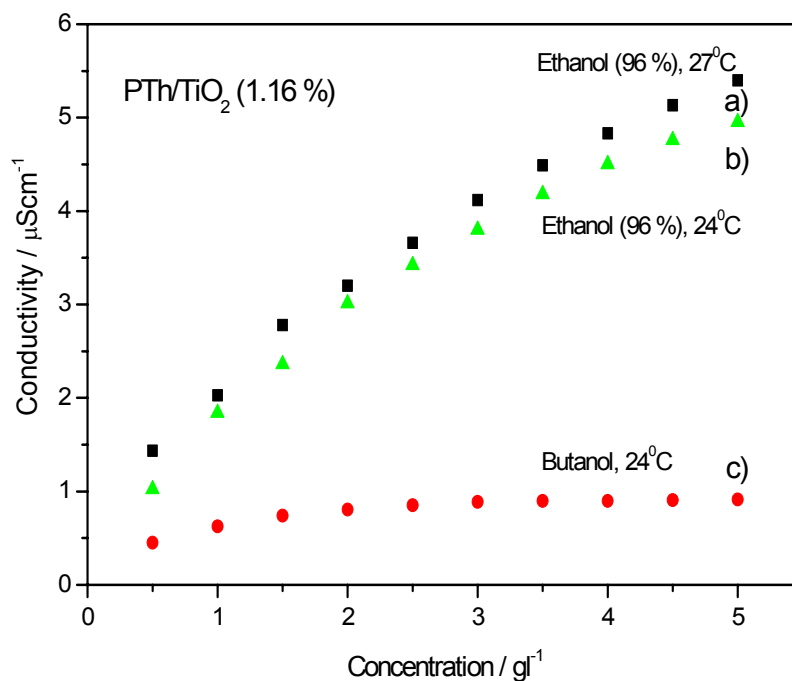


Fig.5.6 Conductivity of the PTh/TiO₂ (1.16 % PTh) suspension vs. concentration

5.2.1.2 Stability of suspensions

In order to study the stability of the suspension, UV-VIS spectra were measured. The absorption of the PTh/TiO₂ (1.16 %) suspension in ethanol (96 %) was measured at 530 nm (corresponding with the absorption maximum of PTh in the suspension). The absorption dependence of the PTh/TiO₂ (1.16 %) suspension on time is shown in Fig.5.7. The absorption of the suspension with high concentration (1 g.l⁻¹) decreased faster than the absorption of the suspension with low concentration (0.25g.l⁻¹). The time dependence of the absorption could be explained by the coagulation phenomena similar to conductivity.

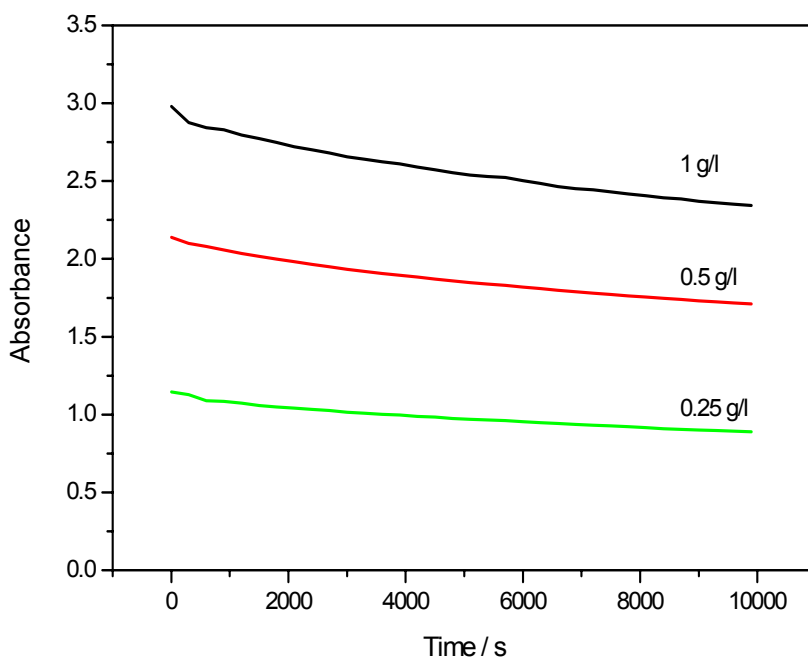


Fig.5.7 Absorption vs. time of the PTh/TiO₂ (1.16 %) suspension in ethanol (96 %) measured at 530 nm

5.2.2 Electrophoretic deposition

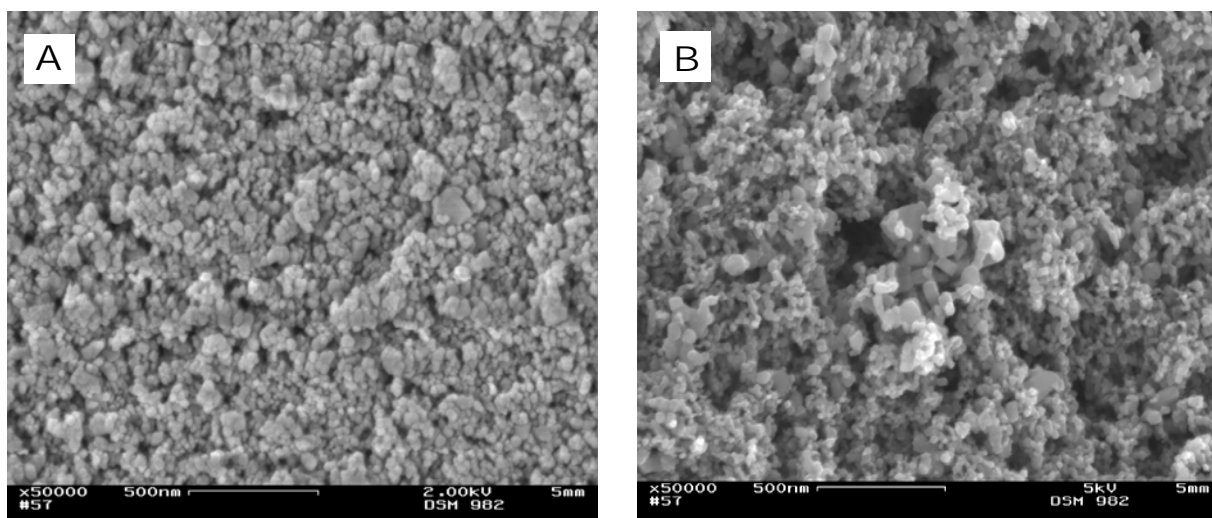


Fig.5.8 SEM-micrographs of PTh/TiO₂ (1.16 %) nanocomposite; magnification: 50,000
A: in a pressed pellet and B: electrophoretically deposited layer

PTh / metal oxide composites could be deposited by EPD on different substrates (platinum, aluminium, ITO, mild steel) from different solvents (absolute ethanol, ethanol 96 %, butanol, isopropanol, water) with current densities of several hundreds $\mu\text{A}\cdot\text{cm}^{-2}$ (at 100 V with a concentration of $5\text{g}\cdot\text{l}^{-1}$). In other solvents (ethylacetate, toluene, glycerol) composites at very low current densities (some $\mu\text{A}\cdot\text{cm}^{-2}$) could not be deposited.

After deposition, the surface structure of the composite layers was investigated by scanning electron microscopy (SEM). SEM micrographs of the pressed pellet and of the EPD layer are shown in Fig.5.8. The pressed layer was denser with almost no pores. The electrophoretically deposited layer possessed “foamy” porous structures. The main characteristics of such a porous layer were high surface area and high light scattering.

5.2.3 Kinetics of electrophoretic deposition

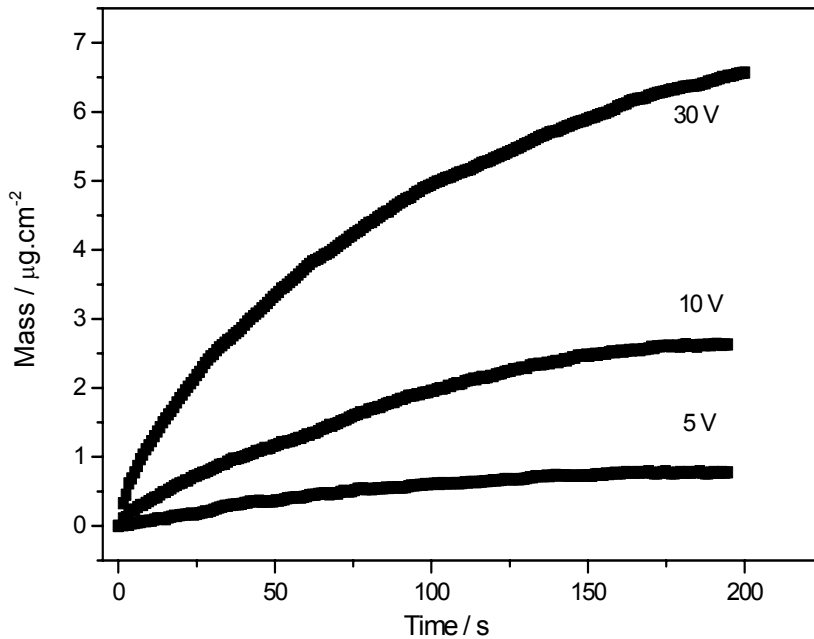


Fig.5.9 Mass-time dependence during EPD of the PTh/TiO₂ (1.16 %) colloidal suspension (0.5 g/l) in ethanol (96 %)

To study the kinetics of the EPD, a combined experimental arrangement of EPD and a quartz crystal microbalance (QCM) was developed. In these experiments, the colloidal concentration of 0.5 g/l was used. As shown in Fig.5.9, the EPD of the PTh/TiO₂ (1.16 %) colloidal suspension in ethanol (96 %) immediately started after dc voltage was applied. In the first period the deposited mass increased very fast, the composite particles formed a first layer on the gold surface. With increasing time, the deposition speed decreased. The totally deposited mass was gradually decreasing. For example, 5.3 µgcm⁻² of the mass increment was obtained for 120 seconds while only 1 µg.cm⁻² of that was deposited for the last 60 seconds (at 30 V). In the first seconds, the mass plot vs. time is linear (Fig.5.10), in agreement with Zhang’s observation (Eq.2.6, Ref. [111]). For longer periods of deposition time the mass was linearly depending on the square root of time, in agreement with Will’s equation (Eq.2.18, Ref. [112]), as shown in Fig.5.11. The deposited particles consisted of the oxide core and the PTh shell and were not conducting. Therefore, the origin of the self-

inhibiting nature of the process could be a linear variation of the field gradient at the surface with increasing film thickness.

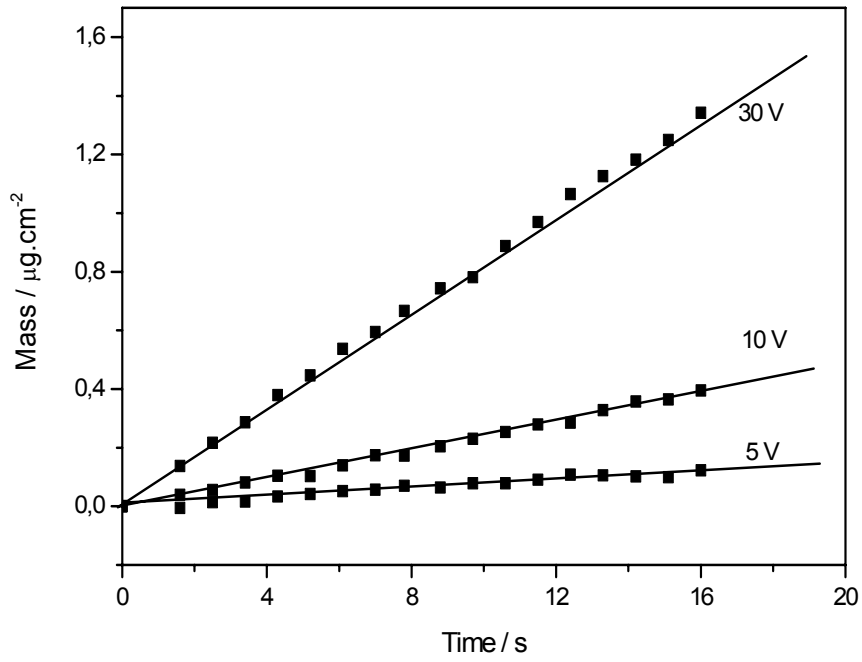


Fig.5.10 Plot of mass vs. time (data received as in Fig.5.9)

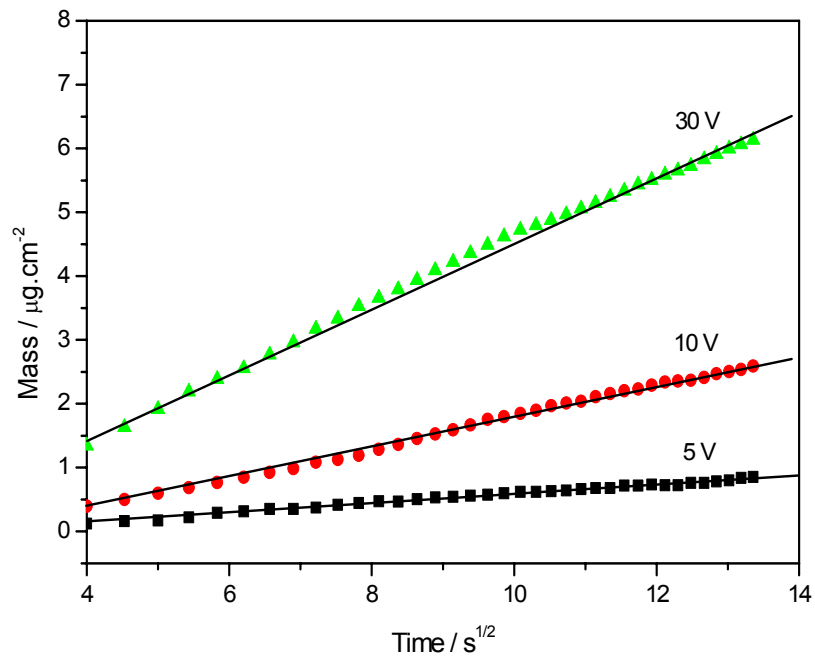


Fig.5.11 Plot of mass vs. $t^{1/2}$ (data received as in Fig.5.9)

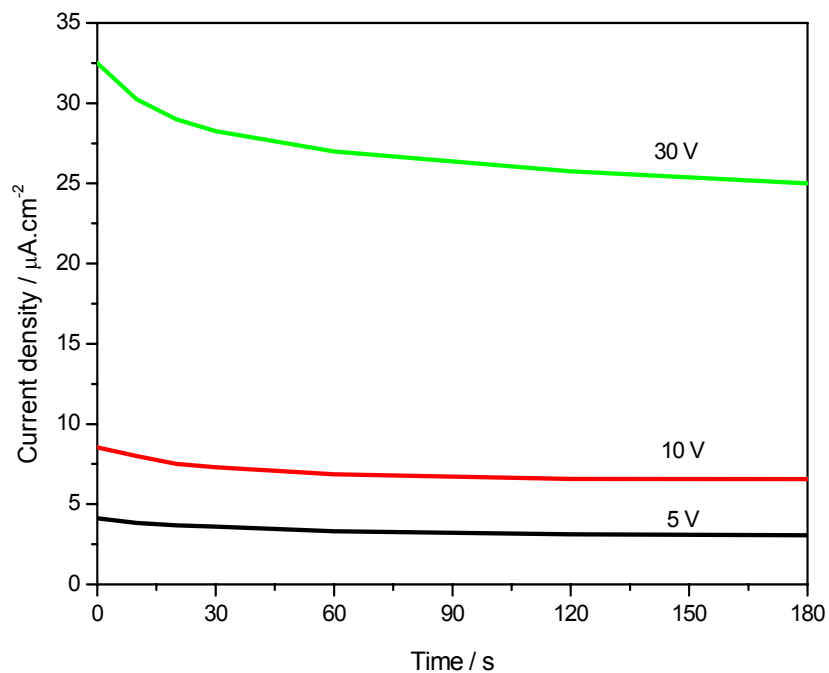


Fig.5.12 Current – time dependence during deposition of the PTh/TiO₂ (1.16 %) colloidal suspension (0.5 g/l) in ethanol (96 %)

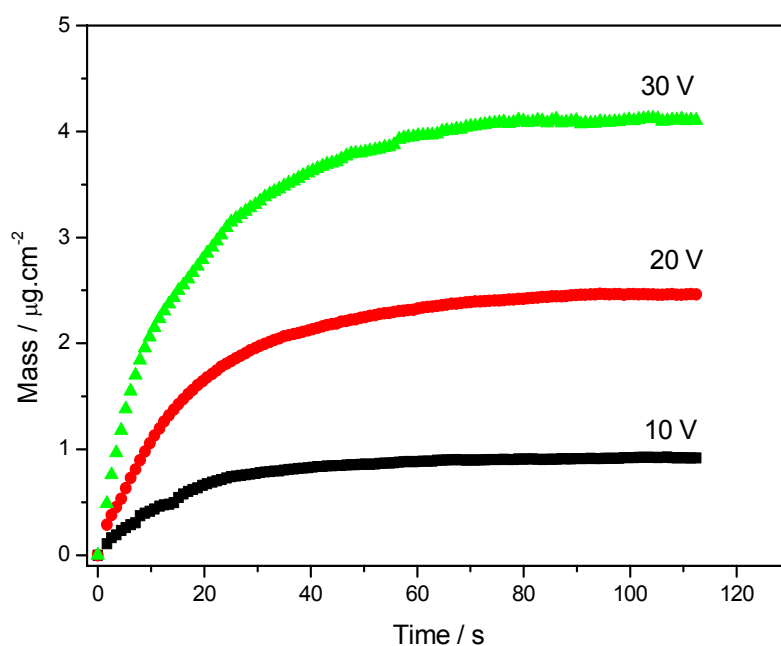


Fig.5.13 Mass-time dependence during EPD of the PTh/TiO₂ (1.16 %) colloidal suspension (0.5 g/l) in butanol

The time dependence of the current during deposition, corresponding with the deposition in Fig.5.9 is presented in Fig.5.12. In the beginning of deposition, the current decreased rapidly with time. The deposition current is proportional to the composite concentration, the electric field and the reciprocal value of the viscosity of the solvent. When a higher dc potential was applied, the current increased and the speed of deposition increased (Fig.5.9

and Fig.5.12). During deposition the growing layer formed an increasing resistance at the electrode, decreasing the electric field in the solution, the driving force for the electrophoretic movement as well as for the coagulation on the surface of the growing composite layer.

In butanol, the EPD of the PTh/TiO₂ (1.16 %) colloidal suspension of the same concentration as in ethanol (96 %) was faster (Fig.5.13). The value of 3.5 g was received after 30 s at 30 V. This could be explained by the differences of the zeta potential of the colloidal particles (ζ), of the viscosity of solvent (η) and of the dielectric constant of solvent (ϵ). According to Hamaker, the rate of deposition can be calculated by the following equation:

$$\frac{dW}{dt} = f \cdot \mu \cdot E \cdot S \cdot C \quad (2.2)$$

In which, μ is the electrophoretic mobility which depends on the zeta potential [178]:

$$\zeta = \frac{3\eta \cdot \mu}{2\epsilon} \quad (5.2)$$

From (2.2) and (5.2), the rate can be calculated as:

$$\frac{dW}{dt} = \frac{2f \cdot E \cdot S \cdot C \cdot \epsilon \cdot \zeta}{3\eta} \quad (5.3)$$

where, f is the correction factor of deposition, S is the surface area of electrode, C is the concentration of the suspension. Parameters measured during EPD of PTh/TiO₂ (1.16%) in ethanol (96 %) and in butanol are shown in Tab. 5.2. Taking these parameters into Eq.5.3, the deposition rate in butanol was higher than that in ethanol (96 %).

Tab.5.2 Parameters of the PTh/TiO₂ (1.16 %) colloidal suspensions in ethanol (96 %) and in butanol

	Ethanol (96%)	Butanol
Zeta potential (mV)	34.7	28.9
Viscosity (mPa.s)	1.2	3.0
Dielectric constant	24.3	17.8

Even in water, the EPD was possible (Fig.5.14). The deposited layers were not smooth and not dense (Fig.5.21a). The mass increase measured with the QCM was discontinuous.

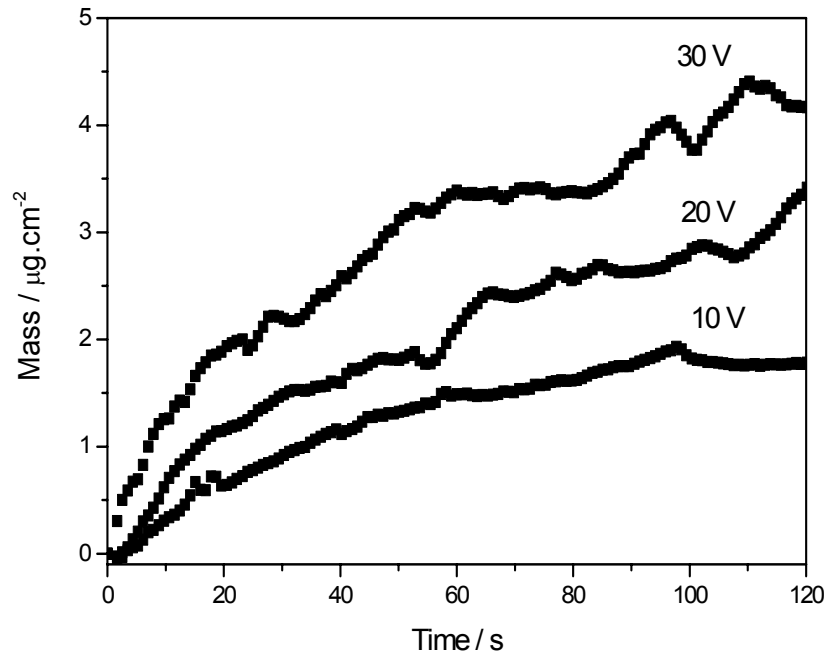


Fig.5.14 Mass-time dependence during EPD of the PTh/TiO₂ (1.16 %) colloidal suspension (0.5 g/l) in water

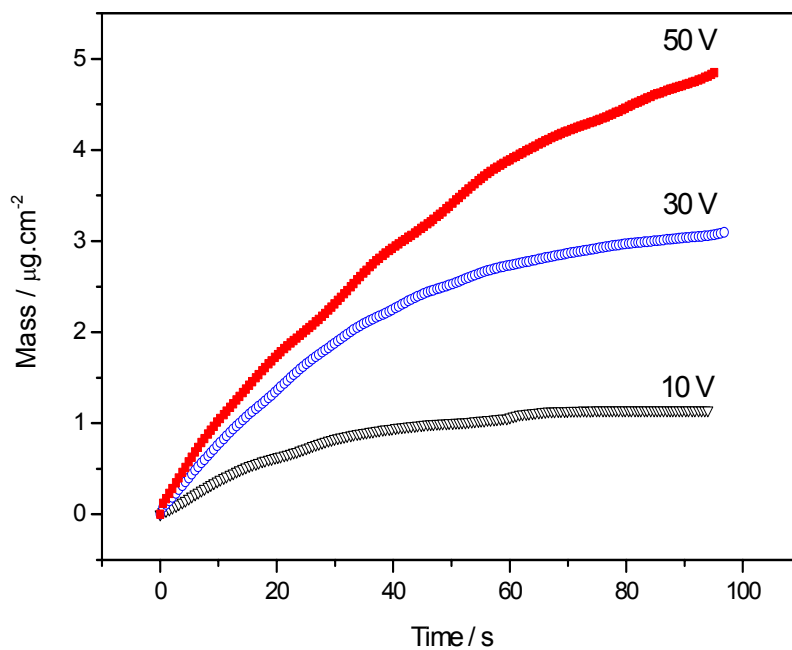


Fig.5.15 Mass-time dependence during EPD of the PMT/TiO₂ (1.2 %) colloidal suspension (0.5 g/l) in ethanol (96 %)

In order to get better insight into the kinetics of the deposition process of the PTh/TiO₂ (1.16 %) system, the PMT/TiO₂ (1.2 %) suspension of 0.5 g/l was investigated in ethanol (96 %). Similar to the results shown in Fig.5.9, the EPD started immediately after dc voltage was applied (Fig.5.15). With increasing time, the deposition speed decreased. The

deposited mass per time interval gradually decreased. Analogous to the PTh/TiO₂ system, for longer periods of time the mass depended linearly on the square root of time, obeying Will's equation (Eq.2.18, Ref. [112]), as shown in Fig.5.16.

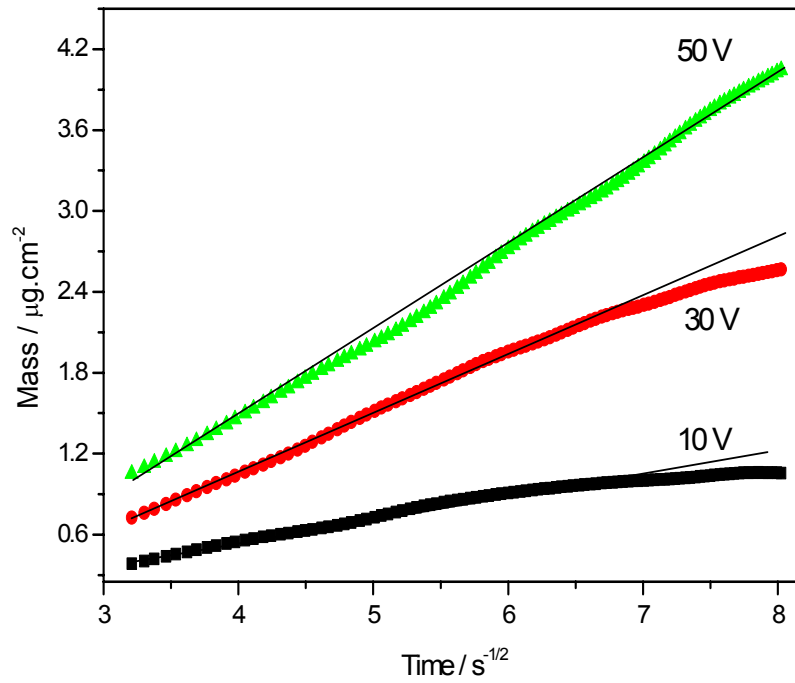


Fig.5.16 Plot of mass vs. $t^{1/2}$ (data received as in Fig.5.15)

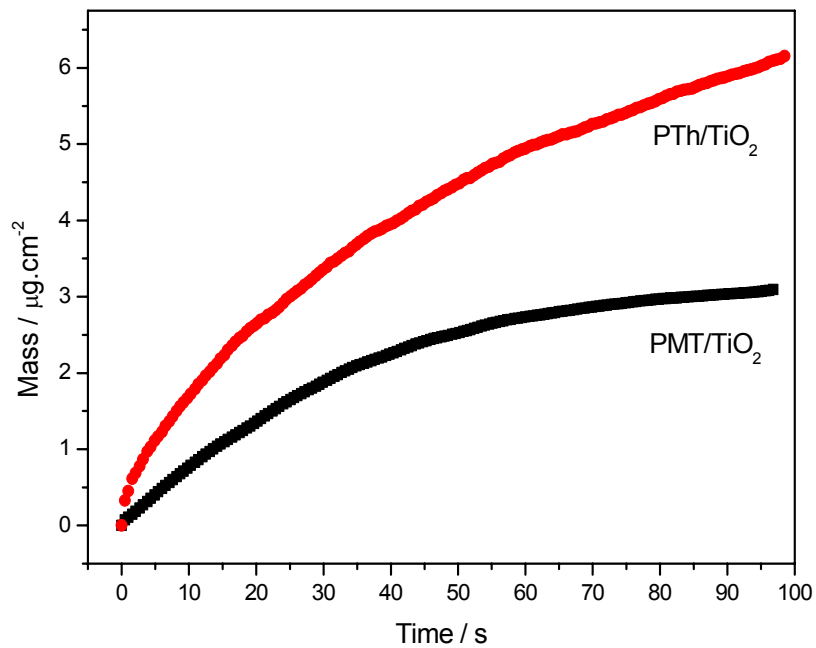


Fig.5.17 Mass-time dependence during EPD of the PMT/TiO₂ (1.2 %) suspension in comparison with that of the PTh/TiO₂ (1.16 %) suspension (Condition: in ethanol 96 %, $C_0 = 0.5$ g/l, at 30 V)

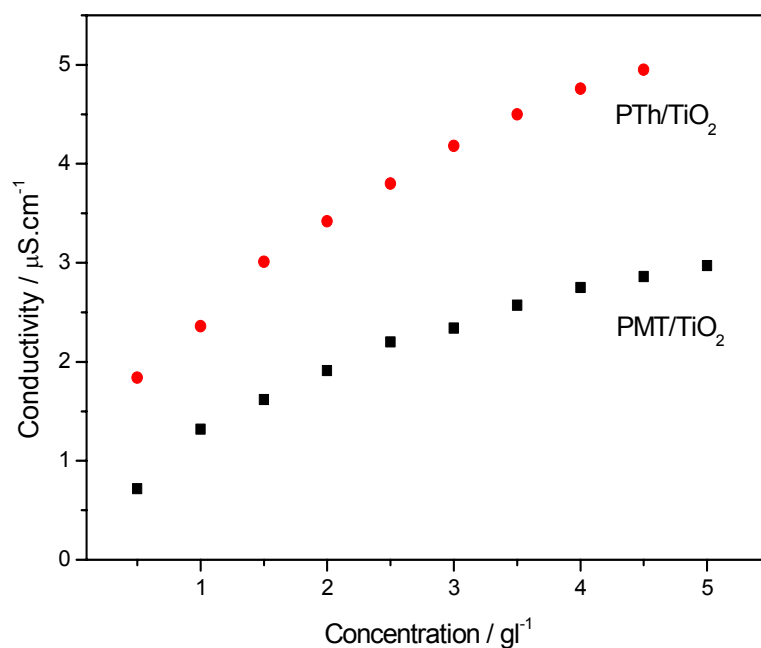


Fig.5.18 Conductivity of PMT/TiO₂ (1.2 %) suspension compared with that of PTh/TiO₂ (1.16 %) suspension (Condition: 24⁰C, in ethanol)

The mass – time dependence during EPD of the PMT/TiO₂ (1.2 %) suspension in comparison with that of the PTh/TiO₂ (1.16 %) suspension is shown in Fig.5.17. Both two experiments were made for the same conditions (in ethanol, C₀ = 0.5 g.l⁻¹, at 30 V). Obviously, the deposition rate of the PTh/TiO₂ system is higher. The deposition would be influenced by the nature of the polymer shell or the zeta potential of the composite particles, for example. Fig.5.18 shows the conductivity – concentration dependence of the PMT/TiO₂ suspension compared with that of the PTh/TiO₂ suspension. It shows that for the same concentration, the conductivity of the PMT/TiO₂ colloidal suspension was always smaller than that of the PTh/TiO₂ system. Conductivity and different zeta potentials might be the origin of the different rates in agreement with Zhang’s equation (Eq.2.6, Ref. [111]).

5.2.4 Mechanism of electrophoretic deposition

As discussed in the part II, the value of zeta potential of particles in the colloidal suspension is a condition for a stable dispersion. The theory of the suspension stability was discussed in Ref. [179, 180]. In nonaqueous dispersions the dissociation / ionization of surface groups (electrostatic stabilization) and adsorption of ionic surfactants (electrosteric stabilization) are possible mechanisms for dispersion stabilities [180]. Oxide surfaces have a large concentration of surface amphoteric hydroxyl groups that can react to yield both

positively or negatively charged particles according to the pH of the medium [180]. E.g., for positive charging in ethanol a three-step mechanism was suggested [180]:

- (i) Adsorption of the ethanol molecules in undissociated forms on the basic surface sites of the oxide particles.
- (ii) Dissociation of these ethanol molecules by H^+ transfer to the basic surface states.
- (iii) Desorption of the EtO^- anions.

This mechanism explains the situation for metal oxide particles as well as for metal oxides not fully covered by thin PTh shells [181]. Counter ions from the solvent form a charge cloud around a charged particle masking their surface charge. This ionic atmosphere is called the diffuse-double layer. When an external electric field is applied, the ions in the diffuse-double layer and the particles move in opposite directions. However, the effective charge of the particle depends on the shear plane between the particle and the diffuse double layer. The potential of the shear plane is called the zeta potential (ζ) or the electrokinetic potential. It is experimentally determined by the measurement of the electrophoretic mobility (μ) [180] and can be obtained from Eq.5.2 [178]:

$$\zeta = \frac{3\eta \cdot \mu}{2\varepsilon} \quad (5.2)$$

where, ε is the dielectric constant and η is the viscosity of the liquid medium. The speed of the particle during EPD is not determined by the surface charge but by the effective charge represented by the zeta-potential. Therefore, the value of the zeta potential is a significant figure for the EPD. Zeta potentials of the PTh/TiO₂, PMT/TiO₂, PTh/Al₂O₃ (D), PTh/Al₂O₃ (C) and PTh/SiO₂ composites in ethanol (96 %) were +34.7, + 32.4, + 54.5, + 41.3 and – 20.2 mV, respectively. The small, negative zeta potential of PTh/SiO₂ particles might be the reason that no deposition was possible.

According to Eq.5.2 and Eq.2.18, the value of zeta potential is connected with the deposited mass. This is shown in Fig.5.17. It describes the EPD process of the PTh/TiO₂ and PMT/TiO₂ systems studied by QCM. Obviously, the higher zeta potential of the colloidal particle is, the higher deposited mass is.

To have more understanding of the EPD mechanism of our systems, the mass – charge dependence is studied (Fig.5.19). It is in agreement with findings from Hamaker (Eq.2.18).

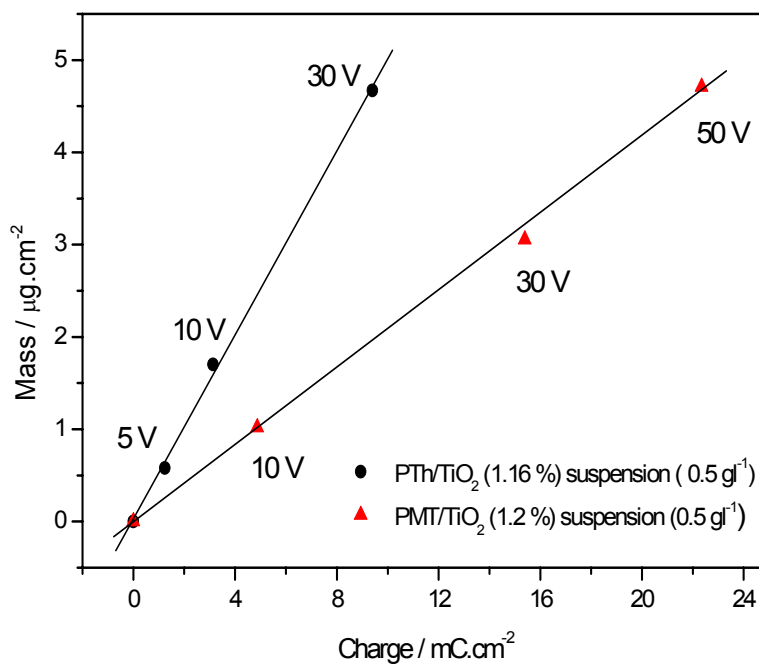


Fig.5.19 Mass – charge dependence during EPD in ethanol (96 %)

The current efficiencies of the deposition at different deposition times were determined (Tab.5.3). As can be seen from Tab.5.3, the current efficiency was decreased from 60 s (1.38 mC/µg) to 180 s (2.87 mC/µg). In addition, when a more concentrated suspension (5.0 g.l⁻¹) was used, the current efficiency calculated for 60 s was 0.66 mC/µg (higher). EPD of a PTh/TiO₂ (1.16 %) suspension of 0.5 g/l in water gave a current efficiency for 60 s of 7.6 mC/µg (lower). From this calculation, the hydrolysis reaction of water in ethanol (96 %) was expected to include in the EPD process. Some experiments were done to understand that assumption. Two suspensions of PTh/TiO₂ (5 g.l⁻¹) in ethanol (96 %) were prepared. In the first suspension, AlCl₃ was added to be 4.10⁻⁴ M. And AlCl₃ was put inside the second suspension to become a concentration of 10⁻³ M. The EPD was carried out with these dispersions at 20 V and in 2 min. The deposited composite layers on the cathode were analyzed by energy dispersive spectroscopy (EDS). The Al(OH)₃ amount of 5.1 % was found when using electrolyte of 10⁻³ M AlCl₃. From electrolyte of 4.10⁻⁴ M AlCl₃, 1.16 % Al(OH)₃ was found in the deposited composite layers. Reactions could be expected at the cathode to produce Al(OH)₃. Water in ethanol was reduced and Al(OH)₃ was formed:



At concentrations of AlCl₃ (10⁻² M), gas bubbles could be seen on the cathode. These experiments showed that the charge connected with the hydrolysis of water in ethanol.

Tab.5.3 Current efficiency of EPD of PTh/TiO₂ (1.16 %) suspension in ethanol (96 %) calculated from QCM results

Potential	Time, 60 s		Time, 90 s		Time, 180 s	
	Q60 (mC)	W60 (μg)	Q90 (mC)	W90 (μg)	Q180 (mC)	W180 (μg)
5 V	0.59	0.43	1.23	0.58	2.41	0.78
10 V	1.86	1.3	3.14	1.67	6.32	2.62
30 V	5.2	3.76	9.4	4.67	19.67	6.36
	H₆₀ = 1.38 mC/μg		H₉₀ = 2.0 mC/μg		H₁₈₀ = 2.87 mC/μg	

In another experiment, the EPD was performed with the PTh/TiO₂ (1.16 %) suspension in absolute ethanol. It lasted 30 min at 100 V with two platinum electrodes. The suspension after deposition was filtered to eliminate composite particles. The solvent (absolute ethanol) was analyzed by Mass Gas Chromatography. No products of oxidation of ethanol could be detected. It means that during EPD the organic solvent was not oxidized.

Tab.5.4 Conductivity of some suspensions

Suspension	Conductivity (μS.cm ⁻¹)
PTh/TiO ₂ (1.16 %) suspension in water	120.00
PTh/TiO ₂ (1.16 %) suspension in ethanol (96 %)	10.14
PTh/TiO ₂ (1.16 %) suspension in absolute ethanol	6.50
PTh/SiO ₂ (~ 1%) suspension in ethanol (96 %)	2.96
PTh/TiO ₂ (1.16 %) suspension in glycerol	1.70

The influence of solvent on EPD was studied with the stainless steel electrodes (4 cm²), at 100 V. The current – time dependence is shown in Fig.5.20. For suspensions (PTh/TiO₂ (1.16 %) in water, PTh/TiO₂ (1.16%) in ethanol (96 %), PTh/TiO₂ (1.16 %) in absolute ethanol, PTh/TiO₂ (1.16 %) in glycerol and PTh/SiO₂ (~ 1 %) in ethanol (96 %)), PTh/TiO₂ could be deposited in water, in ethanol (96 %) and in absolute ethanol. Despite the fact that

the current in absolute ethanol was only around 0.1 mA/cm² (Fig.5.20) deposition occurred. PTh/SiO₂ in ethanol (96 %) could not be deposited maybe because the zeta potential of PTh/SiO₂ particles was small and negative as discussed above.

The PTh/TiO₂ suspension in glycerol gave no deposition. One explanation could be the high viscosity of glycerol. The different currents could be explained by the different conductivities of the suspensions. For the experimental conditions (30⁰C), the conductivities of the studied suspensions are listed in Tab.5.4.

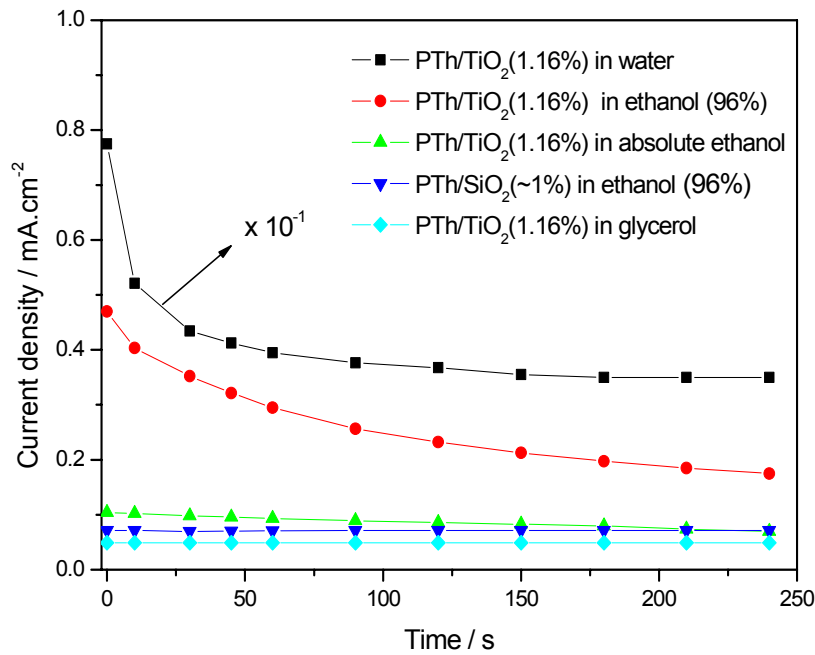
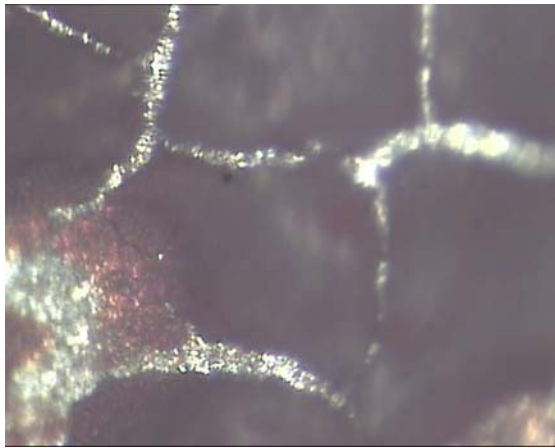
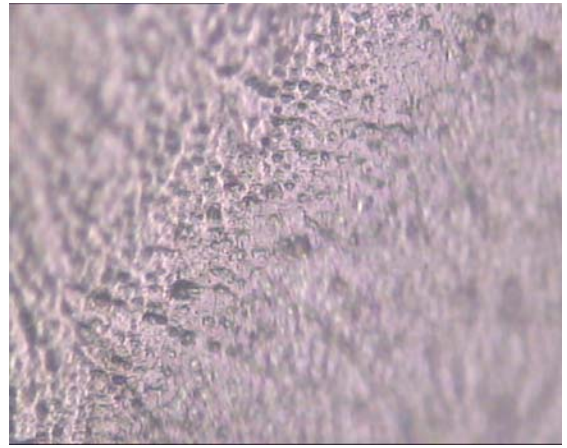


Fig.5.20 Current – time dependence during deposition in different solvents (100 V, concentration 5 g/l, stainless steel electrodes)

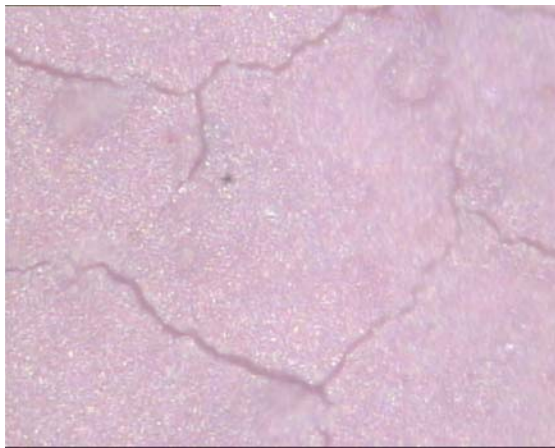
The influence of solvent on the morphology was studied by optical microscope (Fig.5.21). All experiments were carried out for 2 min at 20 V and using platinum as working electrode. In water, after EPD many gas bubbles appeared on the surface of the layer. These bubbles are proposed to be hydrogen produced from hydrolysis of water. When drying, cracks appeared (Fig.5.21 a). In the mixture of ethanol and water (1:1), the surface of the obtained composite layer was rough (Fig.5.21 b). Some small holes appeared on the film. However, after EPD no bubbles could be seen. In ethanol (96 %), the obtained composite layers were very homogeneous, smooth and compact (Fig.5.21 c and d). If the drying process was fast, again cracks appeared (Fig.5.21 c). The layer prepared in butanol was very smooth as deposition in ethanol (Fig.5.21 g). Composite layer prepared in ethanol (96 %) with AlCl₃ (4.10⁻⁴ M) added showed cracks. It was assumed that these cracks were again caused by hydrogen evolution.



a) In water



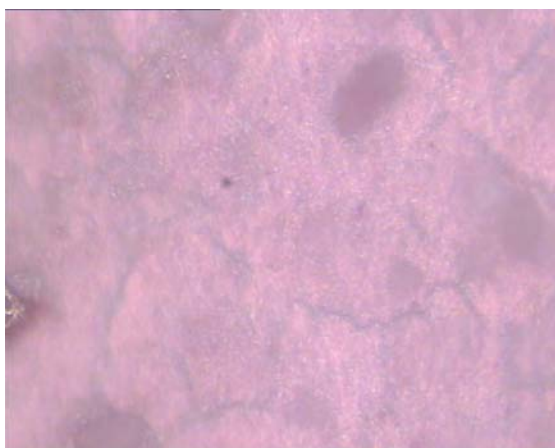
b) In ethanol / water (1:1)



c) In ethanol 96 % (fast drying)



d) In ethanol 96 % (slow drying)



e) In ethanol (96 %) + AlCl_3 ($4 \cdot 10^{-4}$ M)



g) In butanol

Fig.5.21 Optical micrographs of the deposited PTh/ TiO_2 composite layers prepared in different solvents (magnification: 45)

5.3 Characterization of PTh/TiO₂ nanocomposite films prepared by electrophoretic deposition

5.3.1 UV-VIS spectra

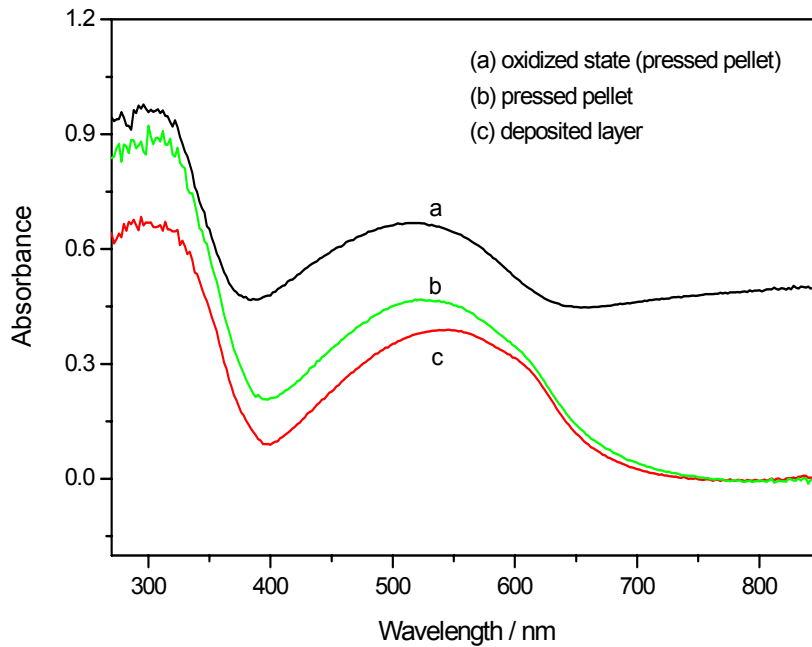


Fig.5.22 UV-VIS spectra of PTh/TiO₂ (1.16 %) nanocomposites

Fig.5.22 shows the optical spectra of PTh/TiO₂ (1.16 %) composites in pressed pellets and electrophoretically deposited composite layers. The absorption maxima occurred around 530 nm, belonging to the absorption maximum of PTh. The optical spectra in the reduced state did not absorb in the near-IR region (> 700 nm). The larger absorption intensity of the pressed pellet (b) in comparison with that of the deposited layer (c) is explained by different film thickness and film structure obtained by the different preparation techniques. The curve (a) presents the UV-VIS spectrum of the oxidized PTh/TiO₂ pressed pellet. Obviously, it shows a wide and strong absorption in the near-IR spectral region which is explained by the polaron absorption.

5.3.2 Photocurrent measurements

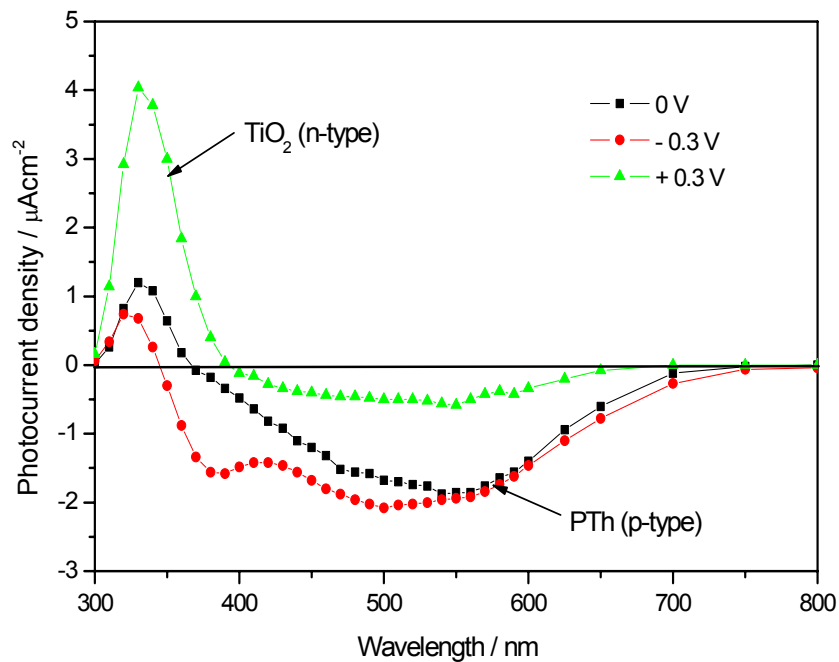


Fig.5.23 Photocurrent spectra of the PTh/ TiO_2 (1.2 %) composite layer deposited on ITO (20 V, 2 min from a suspension of 5 g/l in ethanol 96 %)

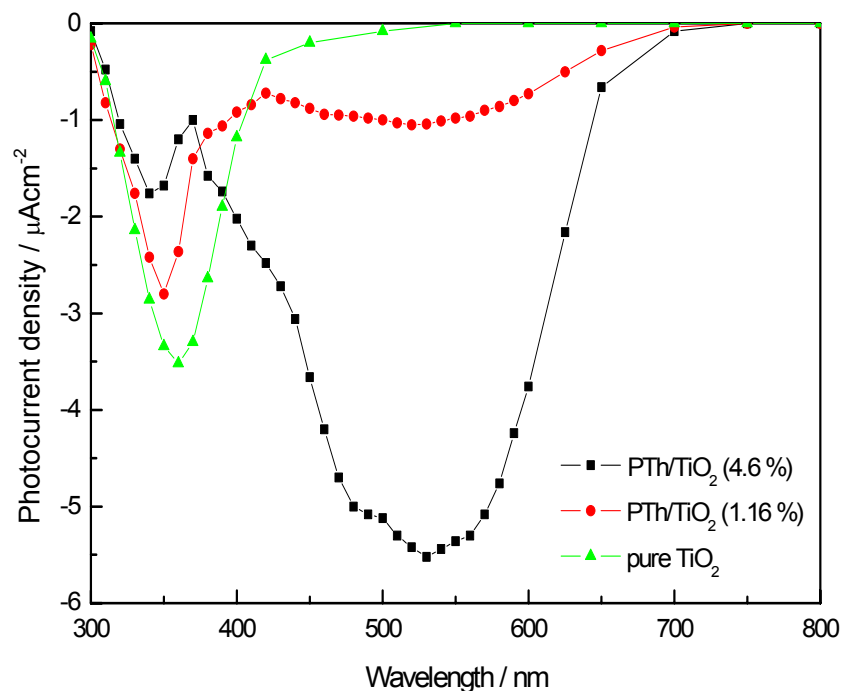


Fig.5.24 Photocurrent spectra of PTh/ TiO_2 composites and of pure TiO_2 layers at $-0.3 \text{ V}_{\text{SCE}}$ (deposited on ITO at 20 V, for 2 min and from suspensions of 5 g/l in ethanol 96 %)

Photocurrents of the reduced form of PTh in the charge depletion region of the PTh/ TiO_2 (1.2%) composite are shown in Fig.5.23. The composites show much higher photocurrents

than previously observed photocurrents with PTh/TiO₂ film electrodes [45]. The previously published photocurrent spectra were measured on films prepared on Pt by rubbing the pressed pellets. The photocurrents in the present paper were measured with films deposited by EPD on transparent electrodes with different film thickness and different film structure. This explains the higher photocurrents.

A stable photocurrent was only obtained after 10-30 min relaxation time. Reversibility of the photocurrent-voltage dependence is achieved if the potential was kept well below the flat-band potential of PTh in order to avoid over-oxidation. Anodic as well as cathodic photocurrents were observed in Fig.5.23, similar to the results in Ref. [45]. The origin of the anodic photocurrent in the film is explained by light absorption in the TiO₂ particles. In the electrolyte it is the oxidation of H₂O (Eq.5.4). The cathodic photocurrent in the film is explained by light absorption by the PTh shell. In the electrolyte it is connected with the reduction of oxygen (Eq.5.5).



When the polarization decreased (from + 0.3 V_{SCE} to -0.3 V_{SCE}) the cathodic photocurrents at about 500 nm increased while the anodic photocurrents at 340 nm decreased. At -0.3 V_{SCE}, an additional negative photocurrent was found at $\lambda = 390 \text{ nm}$ with $i = 1.6 \mu\text{A}\cdot\text{cm}^{-2}$. To determine the origin of this peak, the dependence of the photocurrent on the composition of the material was studied: (i) PTh/TiO₂ nanocomposite with low amount of PTh (1.16 %), (ii) PTh/TiO₂ nanocomposite with high amount of PTh (4.6%) and (iii) pure TiO₂. The layers were deposited on the ITO electrodes at equal conditions in order to get the same thicknesses of the layers. The photocurrent spectra at - 0.3 V_{SCE} of PTh/TiO₂ (4.6 %), PTh/TiO₂ (1.16 %) and pure TiO₂ layer are shown in Fig.5.24. Obviously, the cathodic peak at 340 nm comes from TiO₂. It is observed at negative electrode potentials (- 0.3 V_{SCE}) in the vicinity of the flatband potential of TiO₂ and might be connected with surface states.

From Eq.3.8, the flatband potential (E_{fb}) can be obtained when plotting the photocurrent as a function of applied voltage (E) as shown in Fig.5.25 for 530 nm. The values $E_{\text{fb}} = 0.6 \text{ V}_{\text{SCE}}$ and $E_{\text{fb}} = 0.55 \text{ V}_{\text{SCE}}$ were found for PTh/TiO₂ composites with PTh content 4.6 % and

1.16 %, respectively. Obviously, the photocurrent depends on the TiO₂ content. The origin of this is still not clear.

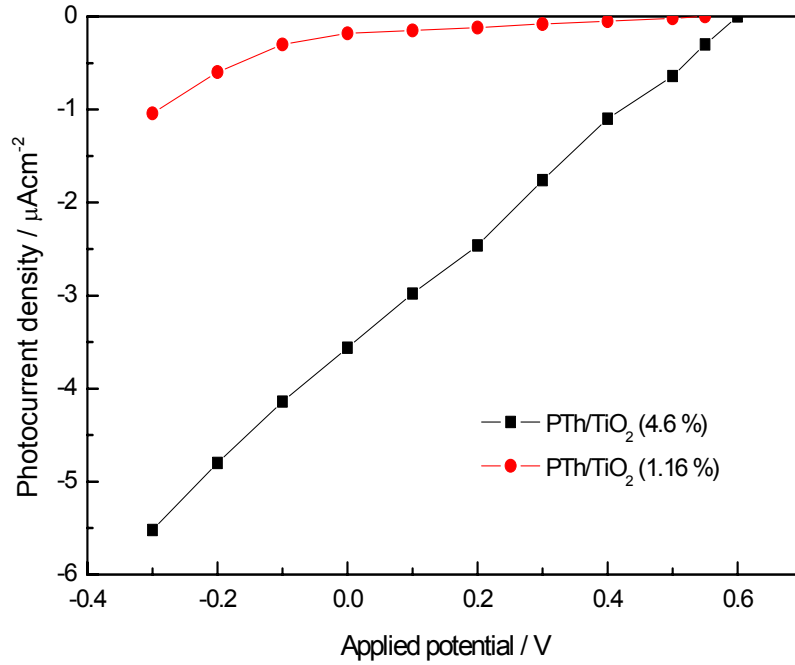


Fig.5.25 Photocurrent-potential dependence, measured at 530 nm

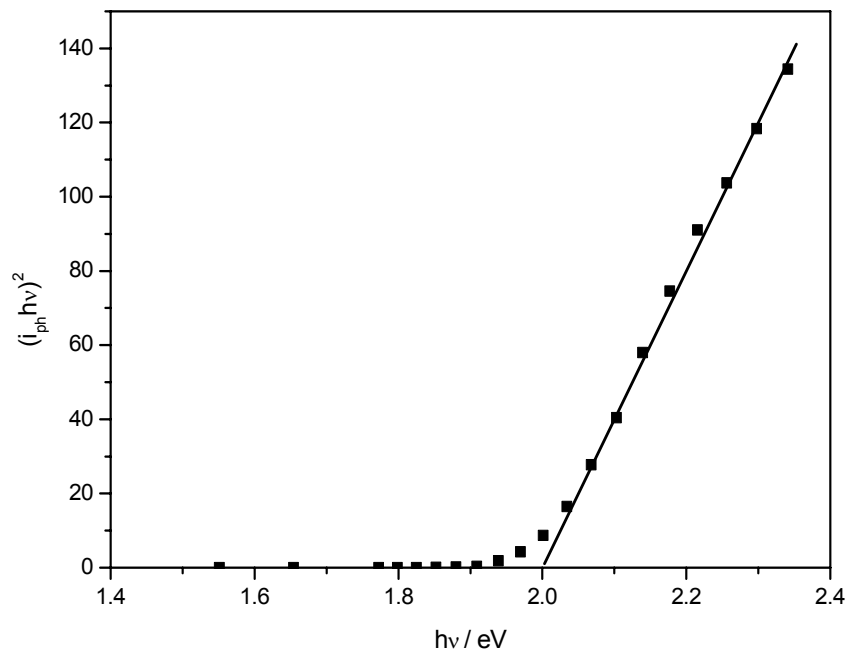


Fig.5.26 $(I_{ph} hv)^2$ vs. $h\nu$ plot of PTh/TiO₂ (4.6%) for determining E_g^{di} of PTh

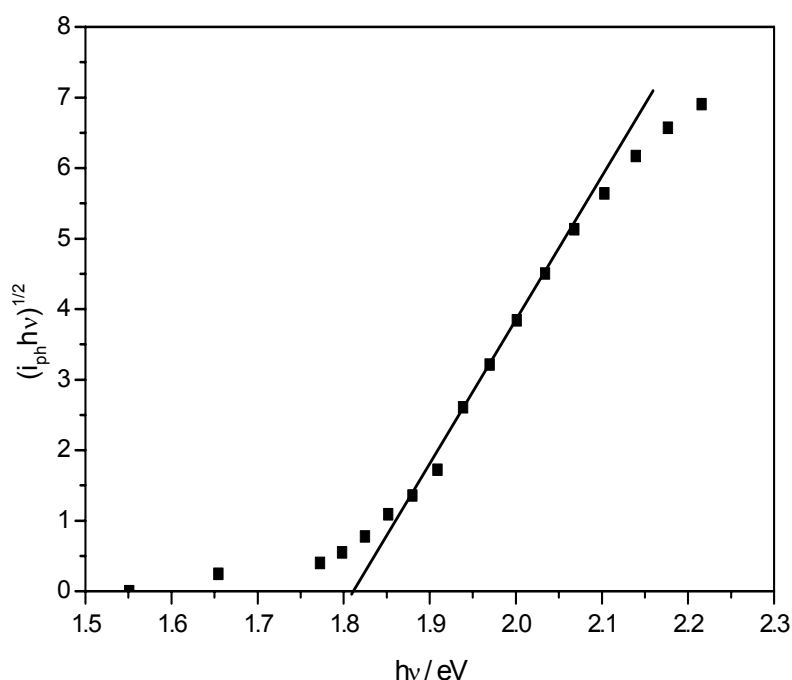


Fig.5.27 $(i_{ph}h\nu)^{1/2}$ vs. $h\nu$ plot of PTh/TiO₂ (4.6%) for determining E_g^{indi} of PTh

The spectrum measured at a fixed potential is a useful tool to determine the bandgap value of a semiconductor and the nature of the electronic transitions. The bandgap energy, E_g can be determined from the linear plot $(i_{ph}h\nu)^2$ vs. $h\nu$ or $(i_{ph}h\nu)^{1/2}$ vs. $h\nu$. These plots are shown in Fig.5.26 and Fig.5.27. The photocurrent spectrum was measured with PTh/TiO₂ (4.6%) composite at $-0.5 V_{SCE}$. The $(i_{ph}h\nu)^2$ vs. plot shows a better fit to the experimental data.. Obviously, the direct electron transition dominates. The curve was extrapolated to the x-axis to determine the bandgap energy. The value $E_g^{di} = 2.0$ eV (for the direct electron transition) corresponds to that obtained from the absorption edge in the optical spectra [181] and shows a good agreement with the values for polymethylthiophene ($E_g = 1.9$ eV, Ref. [182]) and polybithiophene ($E_g = 2.03$ eV, Ref. [177]).

5.3.3 Cyclic voltammetry (CV)

Fig.5.28 shows the CV curves of and PTh/TiO₂ (4.6%) nanocomposite layers deposited on platinum at 100 V. The observed oxidation potential of PTh ($+0.8 V_{SCE}$) is in good agreement with values published in the literature ($+0.76 V_{SCE}$) [9, 10]. The anodic peak current-density decreased only slightly with the cycle number. The reduction potential of PTh was $+0.75 V_{SCE}$. The TiO₂ core showed no electrochemical activity. The onset oxidation potential of PTh was $+0.6 V_{SCE}$. It was determined by an extrapolation of the linear part of the CV curve to zero current.

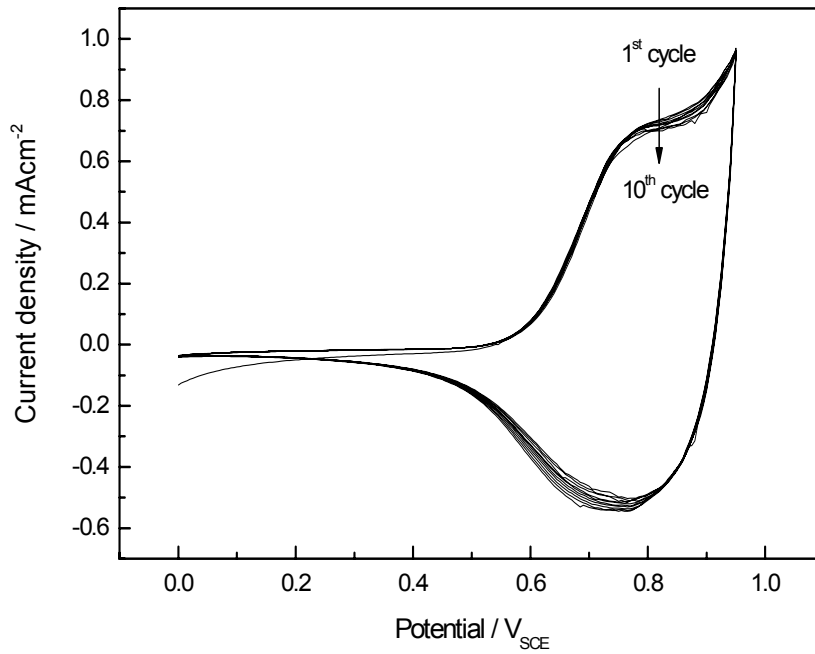


Fig.5.28 Cyclovoltammogram of PTh/TiO₂ (4.6 %) composite layer prepared by EPD on platinum (E = 100 V, 3 min)

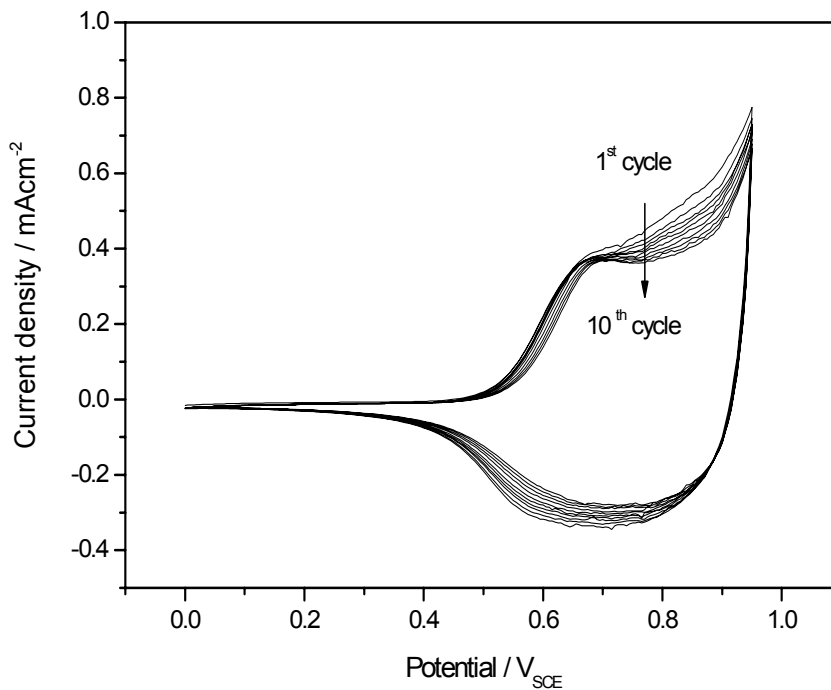


Fig.5.29 Cyclovoltammogram of PTh/TiO₂ (1.16 %) composite layer prepared by EPD on platinum (E = 100 V, 3 min)

For PTh/TiO₂ (1.16 %) composite layer deposited on platinum at 100V, CVs are shown in Fig.5.29. The observed potential of oxidation of PTh (+0.75 V_{SCE}) was lower than that of

the PTh/TiO₂ (4.6%). The onset potential of oxidation was slightly smaller (around +0.55 V_{SCE}). The anodic peak current decreased from 0.45 mA.cm² in the first cycle to 0.35 mA.cm² in the 10 th cycle.

5.3.4 Electrochemical impedance spectroscopy

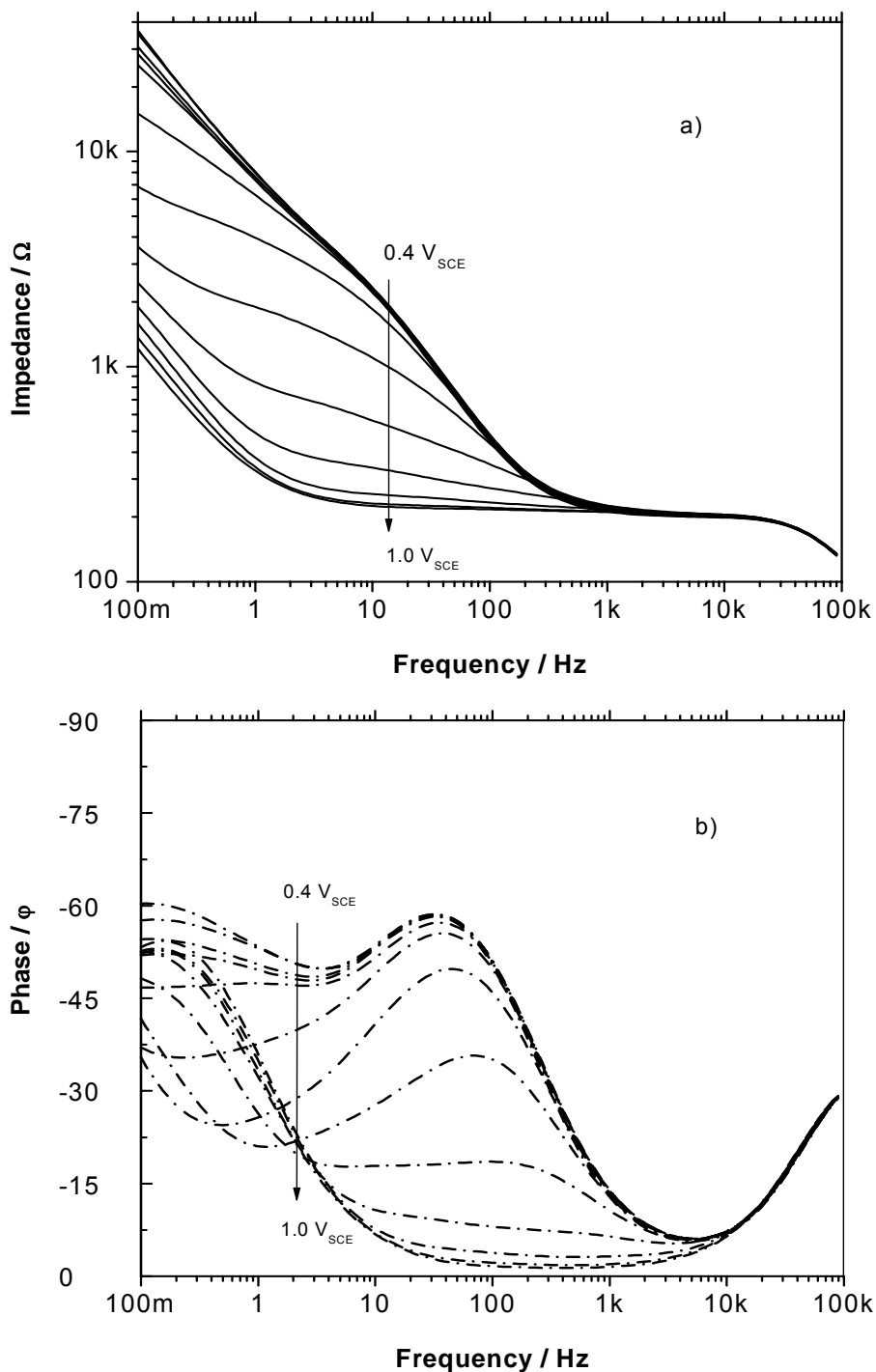


Fig.5.30 Bode plot of the impedance measurements of the PTh/TiO₂ (4.6 %) composite layer prepared by EPD on platinum (20 V, 2 min) in the potential region of 0.4-1.0V_{SCE}; a) Impedance and b) Phase

Fig.5.30 shows the electrochemical impedance spectra (EIS) of the PTh/TiO₂ (4.6 %) layer deposited on platinum. Differences with older results [45] are explained by different film thickness and film structure obtained by the different preparation methods.

The equivalent circuit shown in Fig.5.31 was used for analyzing the impedance data. It consists of the electrolyte resistance R_s and two R-C combinations, corresponding to the TiO₂ core at low frequencies (< 5 Hz) and the PTh shell at higher frequencies (5–1000 Hz). In the potential range of 0 to 0.55 V_{SCE}, the resistance of PTh/TiO₂ system did not change, indicating that in this potential regime PTh was in the reduced state. From 0.6 to 1.0 V_{SCE}, the PTh resistance reduced, supporting that PTh in the composite changed from reduced semiconducting form to oxidized conducting one. Consequently, the impedance of the whole composite layer decreased. It means that the PTh shell of the nanocomposite film was still electrochemically active after EPD at high potential (20 V).

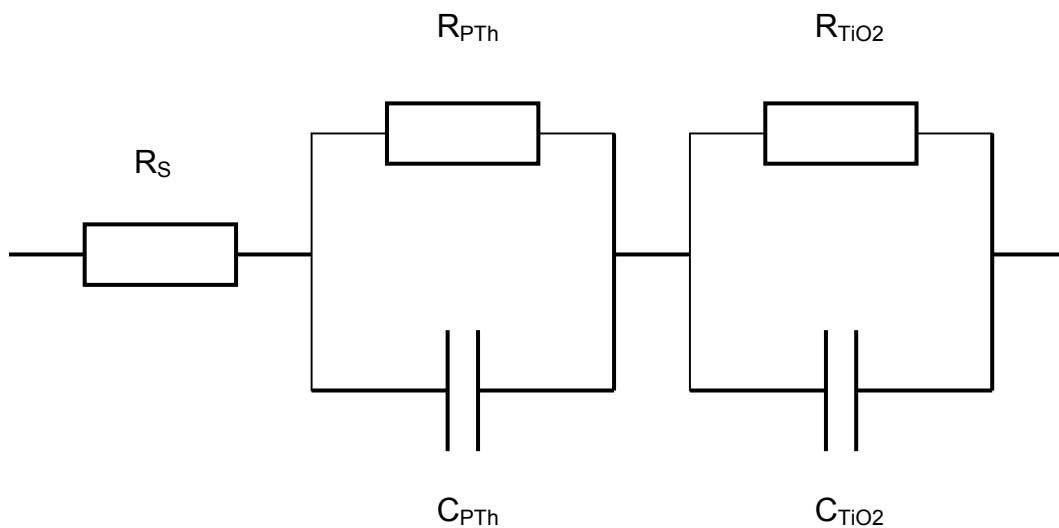


Fig.5.31 Equivalent circuit for a PTh/TiO₂ layer

However, the capacitance of PTh did not change during the oxidation of PTh shell in the potential range of 0.6 to 1.0 V_{SCE} (Fig.5.30 a and b). The reason may be that the amount of PTh was too low and the PTh shell was too thin in order to influence the total measured capacitance of the PTh/TiO₂ system.

For films of PTh/TiO₂ (1.16 %) composition, EIS curves are shown in Fig.5.32. Obviously, if the amount of PTh was low, the change of the impedance of the entire composite system was small when PTh changed from reduced state to oxidized one.

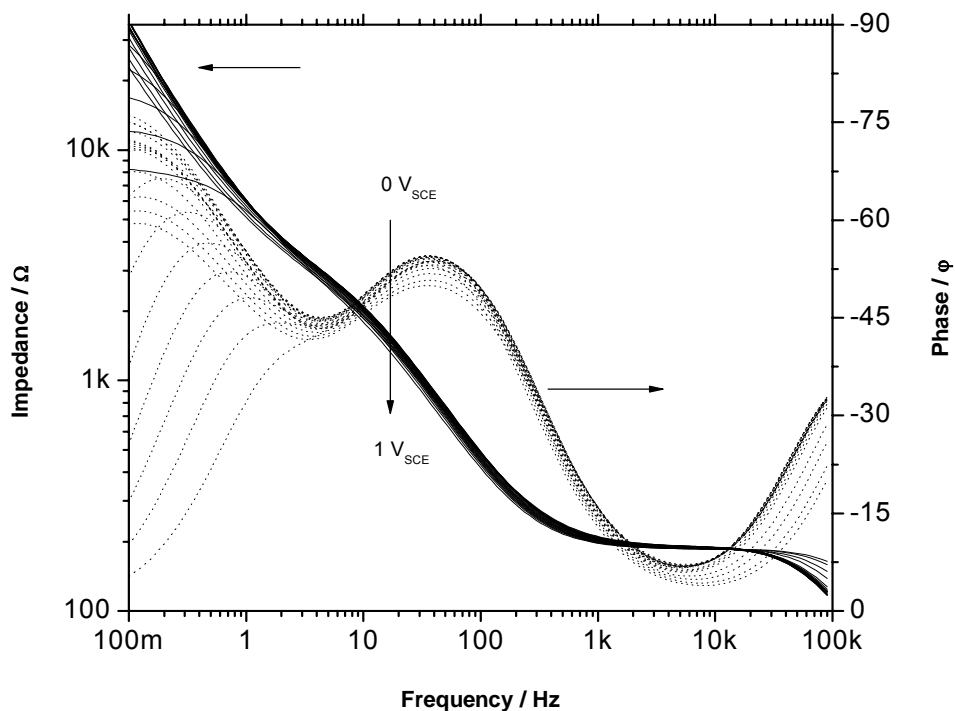


Fig.5.32 Bode plot of the impedance measurements of the PTh/TiO₂ (1.16 %) composite layer prepared by EPD on platinum (20 V, 2 min) in the potential region of 0-1.0V_{SCE}

5.4 Characterization of PMT/TiO₂ nanocomposite films prepared by electrophoretic deposition

5.4.1 Photocurrent measurements

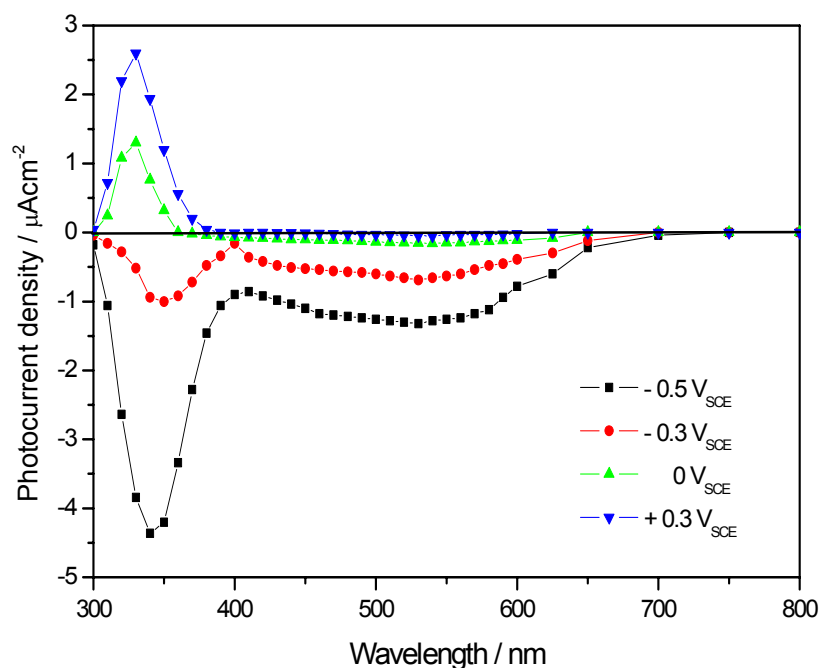


Fig.5.33 Photocurrent spectra of the PMT/TiO₂ (1.2 %) composite layers deposited on ITO at 20 V from a suspension of 5 gl⁻¹

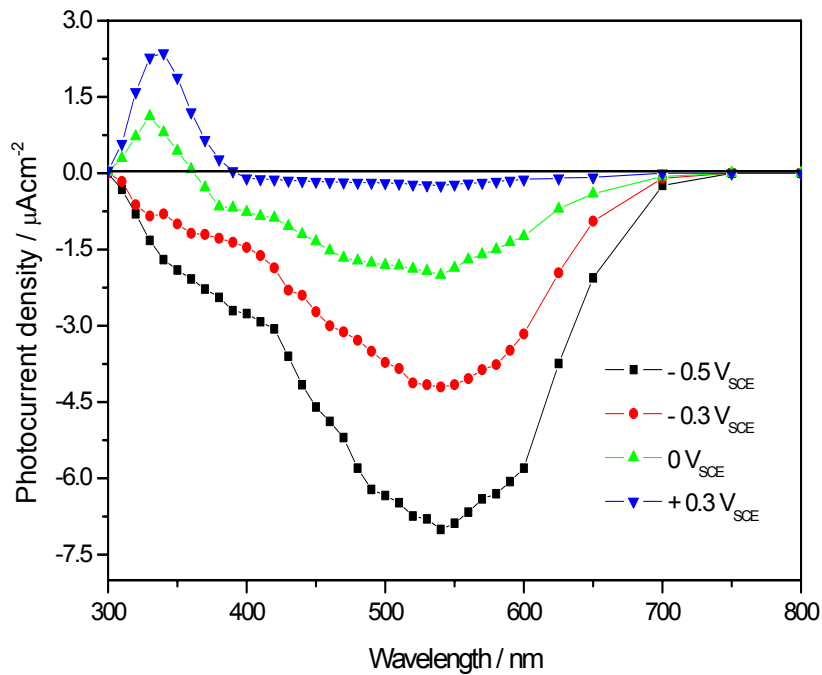


Fig.5.34 Photocurrent spectra of the PMT/TiO₂ (5.3 %) composite layers deposited on ITO at 20 V from a suspension of 5 gl⁻¹

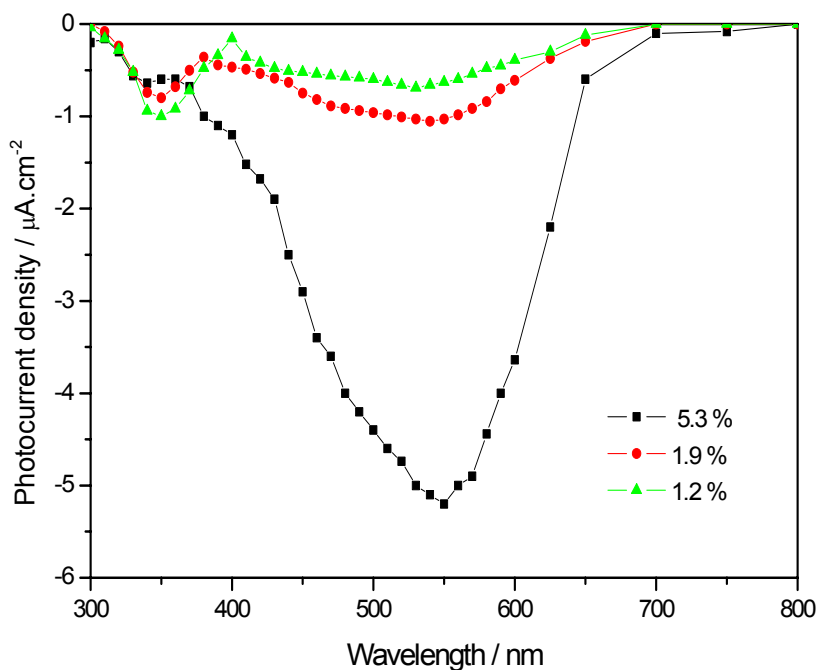


Fig.5.35 Photocurrent spectra of the PMT/TiO₂ composites at $-0.3 V_{\text{SCE}}$

The photocurrent measurements were made at the same conditions of the measurements of the PTh/TiO₂ composite layers. Anodic as well as cathodic photocurrents are shown in Fig.5.33 for PMT/TiO₂ (1.2 %) and Fig.5.34 for PMT/TiO₂ (5.3 %). It is similar to the

results obtained from the PTh/TiO₂ system. When the polarization decreased (from + 0.3 V_{SCE} to - 0.5 V_{SCE}) the cathodic photocurrents at about 530 nm increased while the anodic photocurrents at 340 nm decreased. Analogously to the interpretation of the photocurrents of the PTh/TiO₂ composites, the origin of the anodic photocurrents was the light absorption of TiO₂ and the origin of the cathodic photocurrents was the light absorption of PMT. At 500 nm and + 0.3 V_{SCE}, near the flatband potential of PMT, very weak and negative photocurrents were found. For the negative polarization potentials, cathodic photocurrents appeared at 350 nm were observed.

The photocurrent spectra of different composites were compared in Fig.5.35. With decreasing PMT content the photocurrents at 500-550 nm decreased while the cathodic photocurrents at 350 nm increased. Obviously, the origin of the photocurrents at 350 nm was TiO₂.

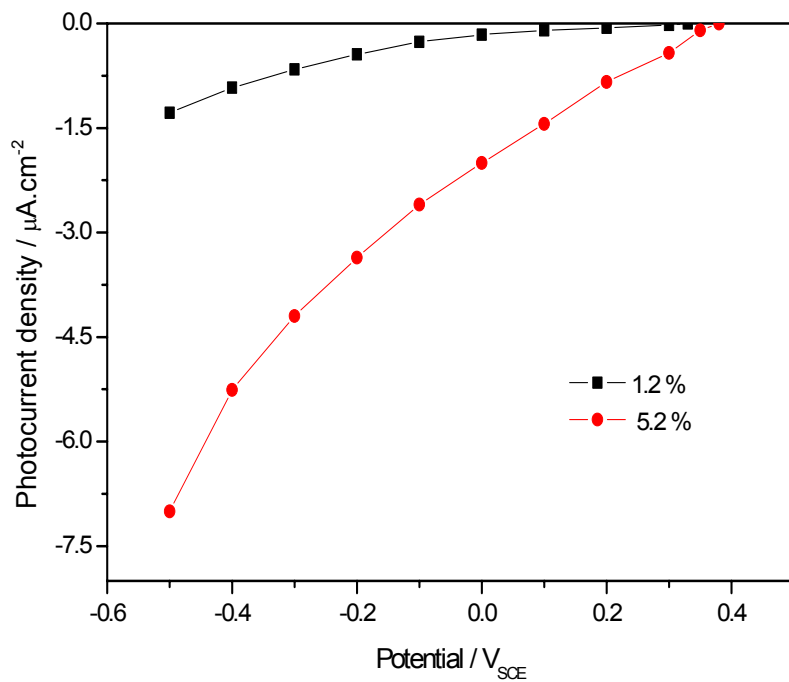


Fig.5.36 Photocurrent – potential dependence of the PMT/TiO₂ composites at 530 nm

From Eq.3.8, the flatband potential, E_{fb} , can be obtained when plotting the photocurrent as a function of applied voltage (E) as shown in Fig.5.36 for 530 nm excitation wavelength. The values $E_{fb} = 0.38 V_{SCE}$ and $E_{fb} = 0.35 V_{SCE}$ are found for PMT/TiO₂ composites with PMT contents of 5.3 % and 1.2 %, respectively. Fig.5.36 shows different slopes of the curves. It means that the photocurrents depend on the amount of PMT in the composite. When the amount of PMT was high, it fully covered the surface of the TiO₂ particles and shielded the TiO₂ core. On the contrary, when the amount of PMT was low, it did not fully

cover the surface of the oxide particles and more light was absorbed at the TiO₂ core surface.

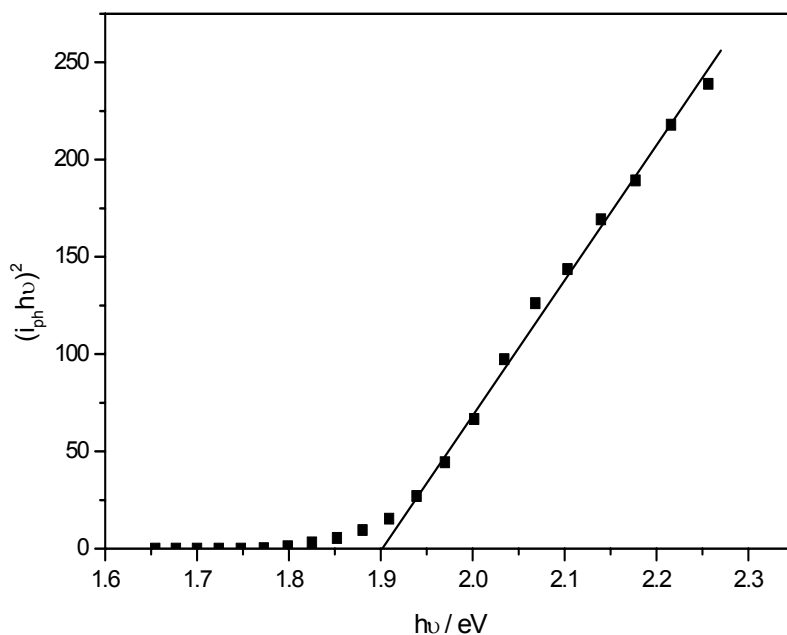


Fig.5.37 $(I_{\text{ph}} h\nu)^2$ vs. $h\nu$ plot of PMT/TiO₂ (5.3 %) for determining E_g^{di} of PMT

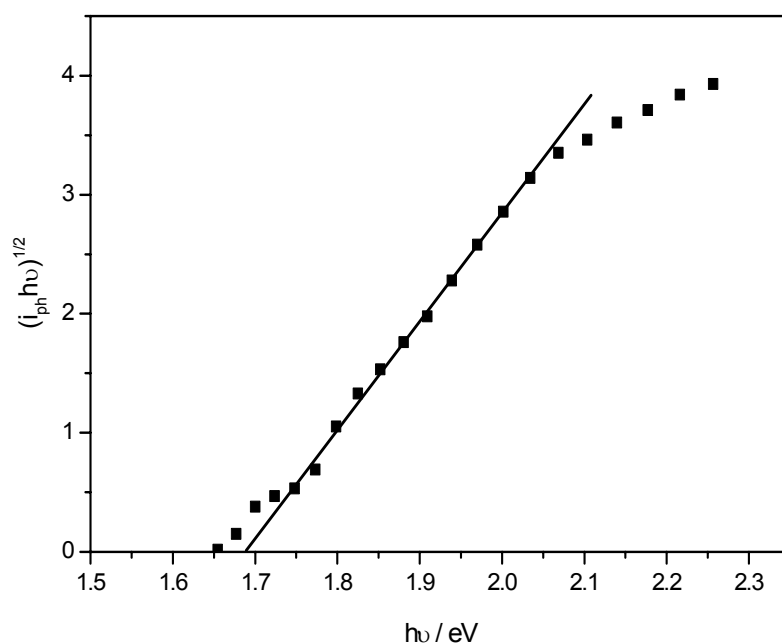


Fig.5.38 $(I_{\text{ph}} h\nu)^{1/2}$ vs. $h\nu$ plot of PMT/TiO₂ (5.3 %) for determining E_g^{indi} of PMT

As discussed in the part III, the bandgap energy, E_g can be determined from the linear part of $(i_{\text{ph}} h\nu)^2$ or $(i_{\text{ph}} h\nu)^{1/2}$ vs. $h\nu$ plots. These plots are shown in Fig.5.37 and Fig.5.38. The photocurrent spectrum was measured for PMT/TiO₂ (5.3 %) composites at $-0.5 V_{\text{SCE}}$.

The $(i_{ph}h\nu)^2$ vs. $h\nu$ plot is a better fit to the experimental data. The value for $E_g = 1.90$ eV (for the direct electron transition case) is similar as the value obtained from the absorption edge in the optical spectra [181] and is the same value previously determined for PMT ($E_g = 1.9$ eV, Ref. [183]). This behavior is in agreement with the behavior of PTh as discussed in part 5.3.

Other experiments were made with solid state cells. A PMT/TiO₂ (5.3 %) composite layer was electrophoretically deposited on an ITO electrode. Then an Al counter electrode was deposited on the composite layer to make a solid state sandwich cell. The short circuit photocurrent spectrum of such cell under vacuum, compared with the UV-VIS spectrum of the electrophoretically deposited layer, is shown in Fig.5.39. A shoulder at 600 nm belonged to the absorption of PMT and a peak in the UV region to the optical adsorption of TiO₂. A large absorption maximum at 450 nm could be explained by the p/n heterojunction between TiO₂ core and PMT shell and the mechanism presented in Fig.5.40. An excitation formed from the photon absorption in the PMT shell dissociated into holes and electrons and were separated in the field inhomogeneity of the composite electrode structure [184].

The photocurrent generation in a p/n heterojunction is shown Fig.5.41. In the prepared material, this process was complicated by the contacts within the composite particles as well as the contacts between particles and electrode.

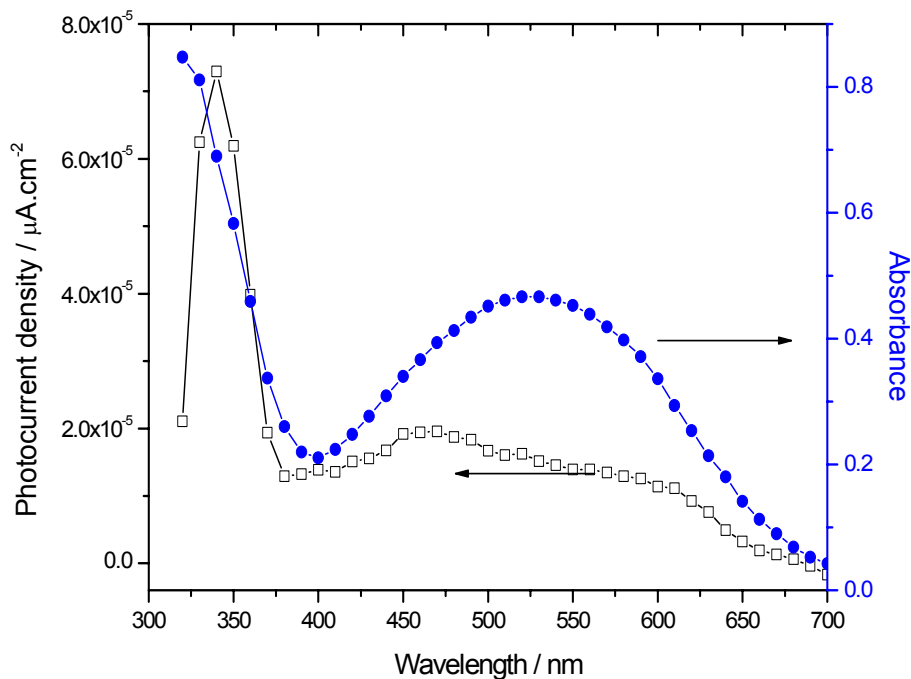


Fig.5.39 Short circuit photocurrent of an ITO // PMT/TiO₂ (5.3 %) composite // Al sandwich cell measured under vacuum, compared with UV-VIS spectra of composite layer

In comparison with the photocurrents measured in electrolyte, the strange absorption at 340 nm disappeared (Fig.5.35).

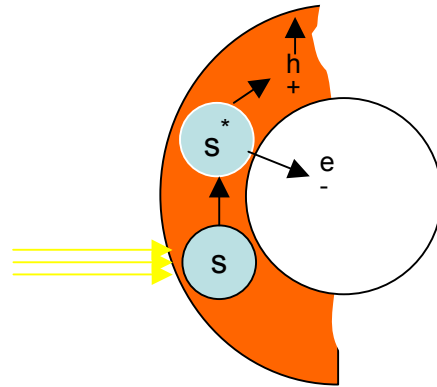


Fig.5.40 Free charge carrier photogeneration mechanism in the p/n heterojunction of the composite particle

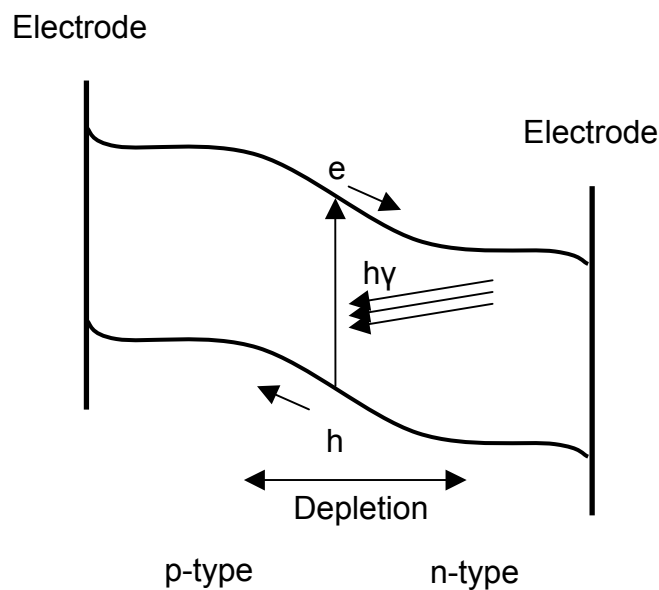


Fig.5.41 Schematic energy diagram and photocurrent generation of p/n junction [184]

The photocurrent spectra of different composites were compared in Fig.5.42. Analogously to the results obtained in electrolyte (Fig.5.24 and Fig.5.35), the photocurrents of the complete solid cells measured under vacuum depended on the amount of PMT. The values of the peaks at 340 nm and at 450 nm increased with the increase of the PMT content. For composites with low amount of PMT (1.2 % and 1.9 %), the shoulder at 600 nm disappeared. It showed that the peak at 600 nm belonged to PMT (Fig.5.39).

Short circuit photocurrents of an ITO // PMT/TiO₂ (5.3 %) composite // Al sandwich cell in the air and under vacuum are shown in Fig.5.43. The photocurrent in the air was higher than that under vacuum. It could be explained by influence of the humidity in the air.

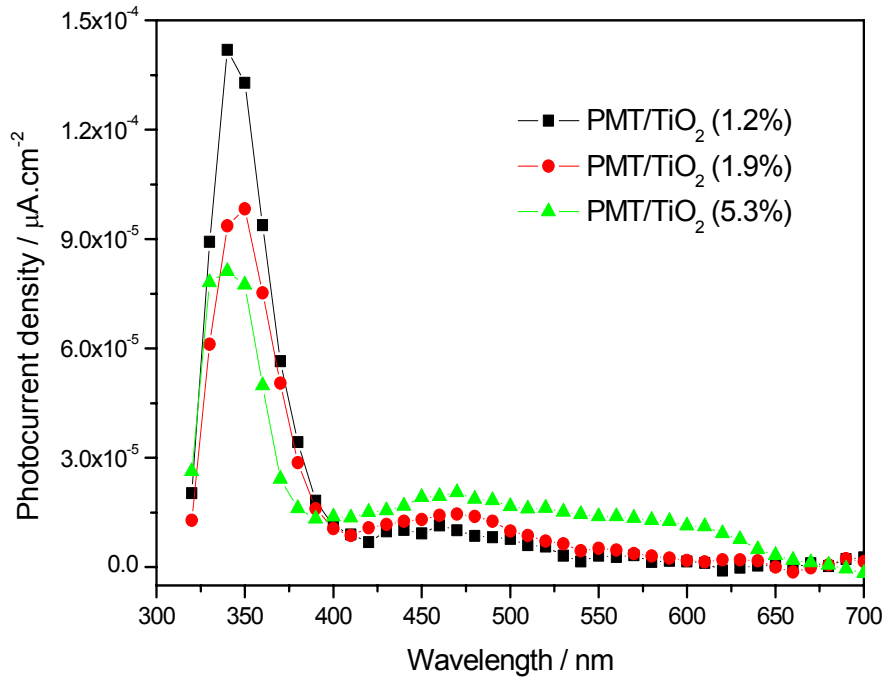


Fig.5.42 Short circuit photocurrents of ITO // PMT/TiO₂ composite // Al sandwich cells measured under vacuum

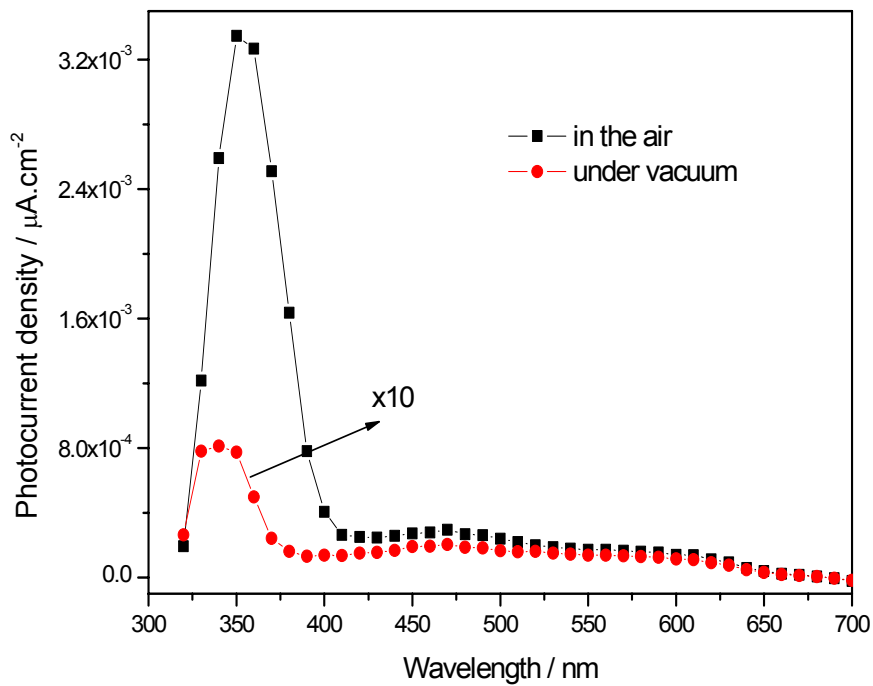


Fig.5.43 Short circuit photocurrents of an ITO // PMT/TiO₂ (5.3 %) composite // Al sandwich cell measured in the air and under vacuum

5.4.2 Current - voltage curves of solid cells

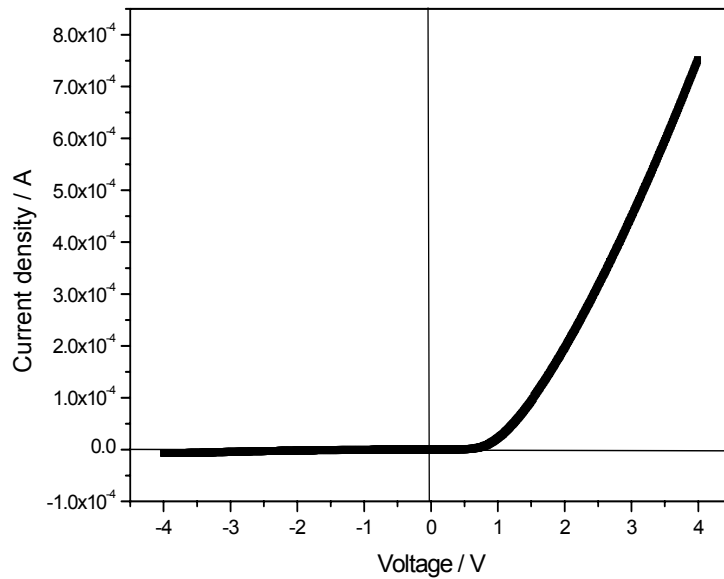


Fig.5.44 Current – voltage curve of the Au//PMT/TiO₂(5.3%)//Al cell

Current - voltage curves (in the dark) of an solid Au//PMT/TiO₂(5.3%)//Al cell in a range of ± 4 V, are shown in Fig.5.44. The typical Schottky diode behaviour is explained by the fact that gold formed an Ohmic contact while aluminium formed a blocking contact with the composite, similar to [185]. Fig.5.45 shows the I/V characteristics on a semi-logarithmic scale. The rectification ratio of 10^2 (at ± 4 V) was found.

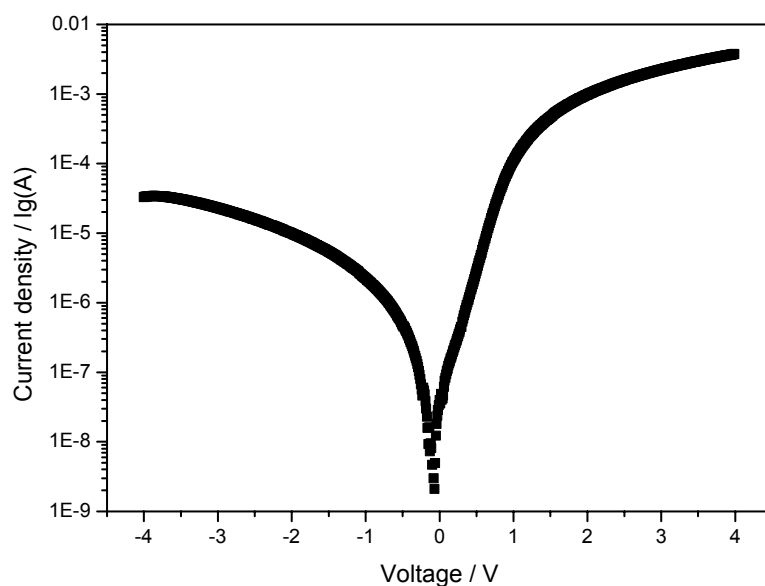


Fig.5.45 Current – voltage curve of the Au//PMT/TiO₂(5.3%)//Al cell (data from Fig.5.44)

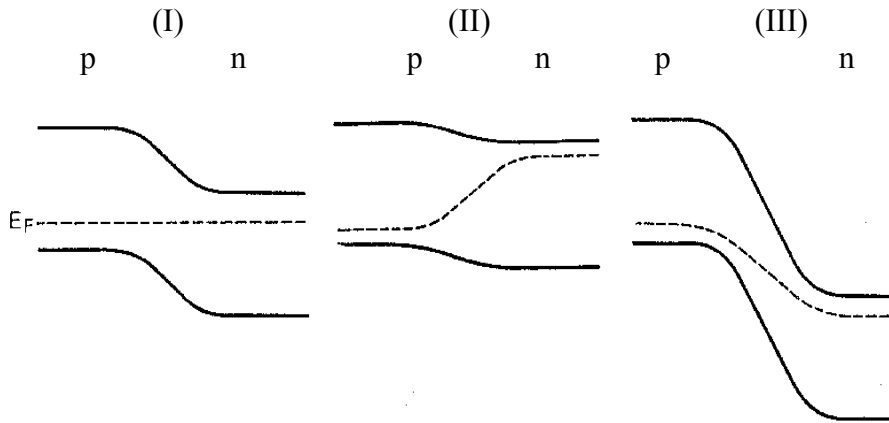


Fig.5.46 p/n junction: I) equilibrium condition II) forward bias and III) reverse bias [186]

The rectification in a p/n junction can be explained as following [186]. An n-type semiconductor material contains mobile negative charges (electrons) and an equal concentration of fixed positive charges (ionized donors). Meanwhile, a p-type semiconductor material contains mobile positive charges (holes) and fixed negative charges (ionized acceptors). With the two regions in contact, the mobile electrons and mobile holes can flow across the heterojunction to recombine together, leaving the n-type region with a net positive charge and the p-type region with a net negative charge, thus establishing a field in a direction which opposes further flow and bringing the Fermi level in the n and p region to the same level. The band bending is connected with the charging of the interface is shown in Fig.5.46 (I). If a positive potential is applied to the p region and a negative potential to the n region, the effect is as shown in Fig.5.46 (II). The potential barrier between two regions is lowered and the forward currents of both holes and electrons are greatly increased. The current arising from the generation of minority carriers remains the same and so there is a net flow of current across the junction with contributions from both holes and electrons. If the p region is made negative with respect to the n region, the potential barrier becomes much higher and the forward flow drops to a very low value for both kinds of carriers Fig.5.46 (III).

From plotting on a semi-logarithmic scale under forward bias, four different regions can be distinguished as indicated in Fig.5.47. First, there is the ideal diode region (0.3 – 0.75 V) where the diode junction quality is quantified using its ideal factor, n . The ideal factor can be obtained from the slope of the curve on a semi-logarithmic scale using [187]:

$$n = \frac{q}{2.303 \cdot B.T} \cdot \frac{1}{slope} \quad (5.6)$$

where the slope is in units of V/decade, q is the electronic charge, B is the Boltzmann's constant and T is the temperature (in degree Kelvin). For an ideal junction, $n = 1$. In the study, n of 4.4 is calculated. The larger value is obtained due to the presence of non-ideal effects. In our case it can be explained by the soft structure of the deposited composite layer as well as by the bad contact between the composite particles and the electrode surface. To the left of the ideal diode region there is the region where the current is dominated by the trap-assisted recombination in the depletion region. To the right of the ideal diode region, the current becomes limited by high injection effects and by the series resistance. High injection occurs in a forward biased p-n diode when the injected minority carrier density exceeds the doping density. High injection will therefore occur first in the lowest doped region of the diode since that region has the highest minority carrier density. For higher forward bias voltages, the current no longer increases exponentially with voltage. Instead, it increases linearly due to the series resistance of the diode. This series resistance can be due to the contact resistance between the metal and the semiconductor, due to the resistivity of the semiconductor or due to the series resistance of the connecting wires. These four regions can be observed in most p-n diodes although the high-injection region rarely occurs, as the series resistance tends to limit the current first.

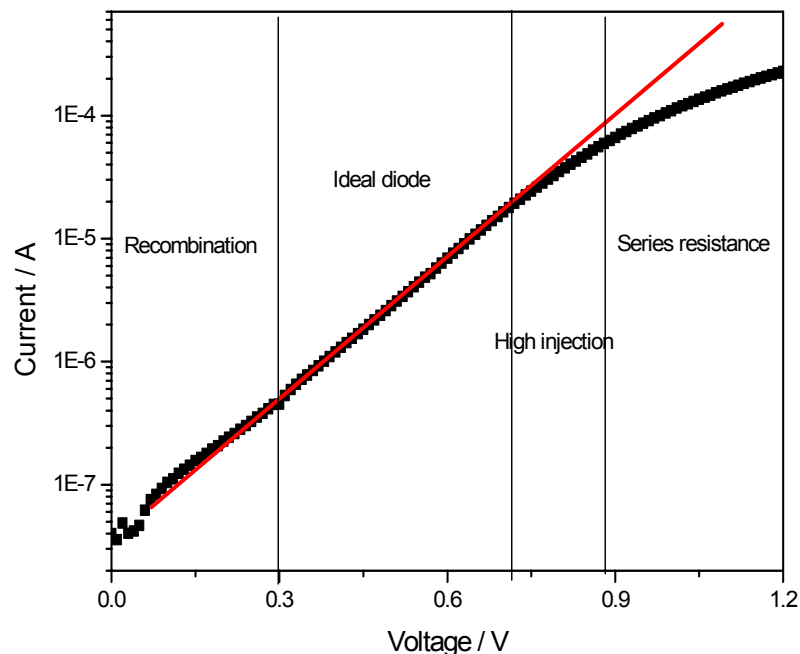


Fig.5.47 Current-voltage characteristic of a Au//PMT/TiO₂(5.3%)//Al cell under forward bias (data from Fig.5.44)

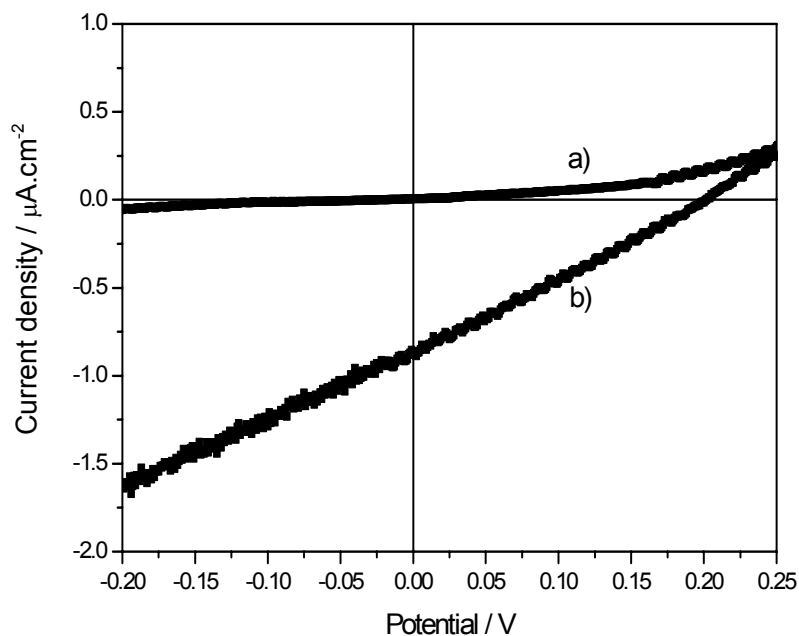


Fig.5.48 Current – voltage characteristic of the solid ITO//PMT/TiO₂(5.3%)//Al cell
a) in the dark and b) under illumination

Current – voltage characteristics for the solid state ITO//PMT/TiO₂(5.3%)//Al tested both in the dark and under illumination through ITO using a Xenon lamp (150 W) are shown in Fig.5.48. In this case, the short circuit current and the open circuit voltage were 0.87 $\mu\text{A}\cdot\text{cm}^{-2}$ and 0.2 V, respectively.

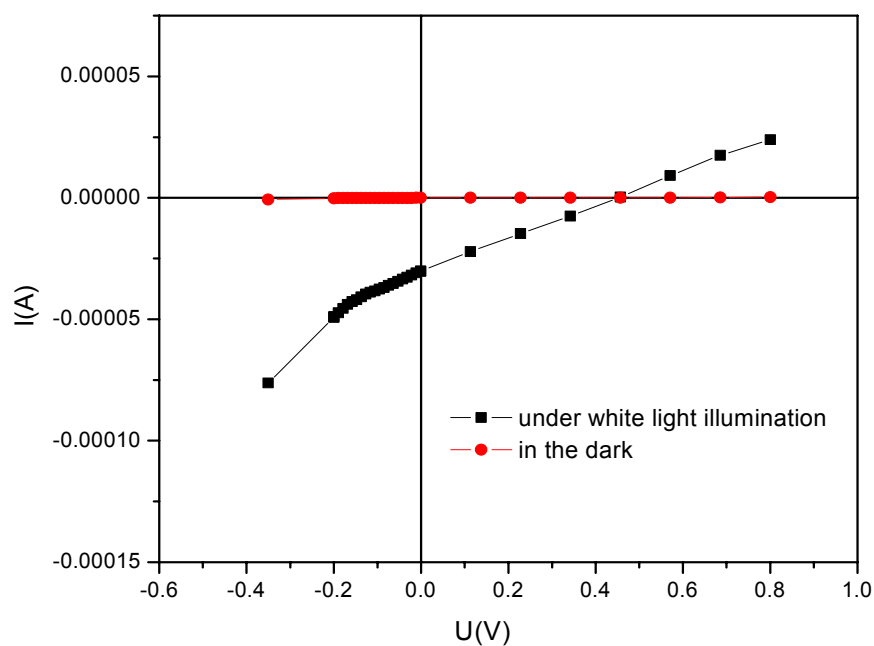


Fig.5.49 I/V characteristic of photoelectrochemical PMT/TiO₂ (5.3 %) cell deposited on ITO in I₂/I₃⁻ electrolyte

Current – voltage characteristics for the photoelectrochemical PMT/TiO₂ cell in the I₂/I₃⁻ electrolyte system recorded both in the dark and under light illumination through ITO using a Xenon lamp (75 W, 10 mW/cm²) are shown in Fig.5.49. In the dark, the current remains relatively constant for a range of - 0.4 V – + 0.8 V. During illumination, a cathodic photocurrent is observed at cathodic potentials, which indicates that the neutral PMT behaves as a p-type semiconductor. The short circuit current (J_{SC}) and the open circuit voltage (V_{OC}) are determined to be 0.06 mAcm⁻² and 0.45 V, respectively. The fill factor (FF) for the cell, which is a measure of the squareness of the out put characteristic, is calculated to be 0.5. Obviously, these values are higher than in the case discussed above (solid state cell) in spite of using the lamp with lower intensity. This indicates that the high resistance of the solid cell was leading to small photocurrents.

5.4.3 Cyclic voltammetry

Fig.5.50 shows the CV curves of PMT/TiO₂ (1.2 %) nanocomposite layers deposited on platinum at 20 V. The onset potential of oxidation was 0.35 V_{SCE}, the observed anodic peak potential of PMT was + 0.67 V_{SCE}, both in agreement with values published in the literature [188]. The anodic peak current-density decreased from 0.37 μAcm⁻² in the first cycle to 0.33 μA.cm⁻² in the 10 th cycle. The reduction potential of PMT was + 0.65 V_{SCE}. As in the case of the PTh/TiO₂ composites, the TiO₂ core showed no electrochemical activity.

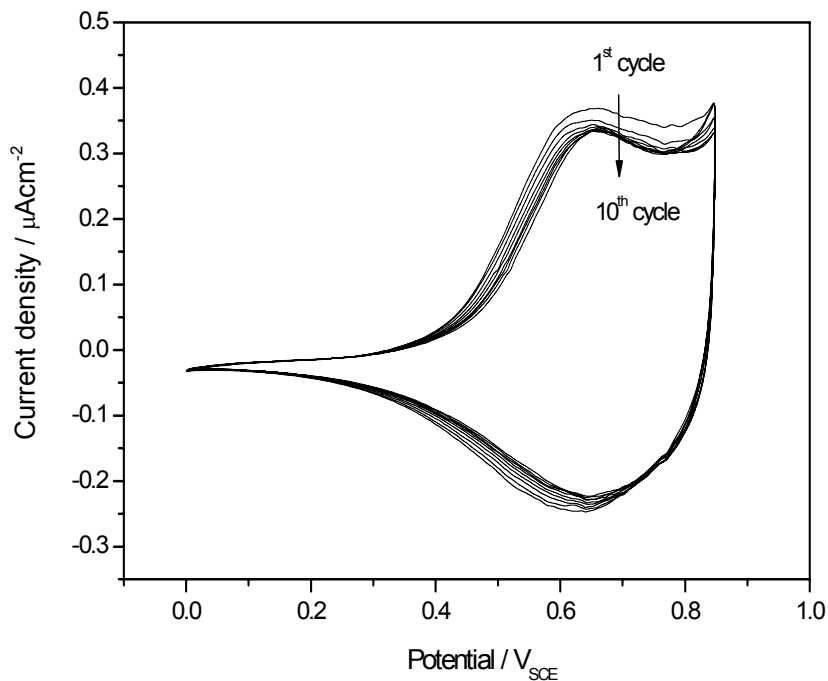


Fig.5.50 Cyclovoltammogram of PMT/TiO₂ (1.2 %) composite layer prepared by EPD on platinum (E = 20 V, 3 min)

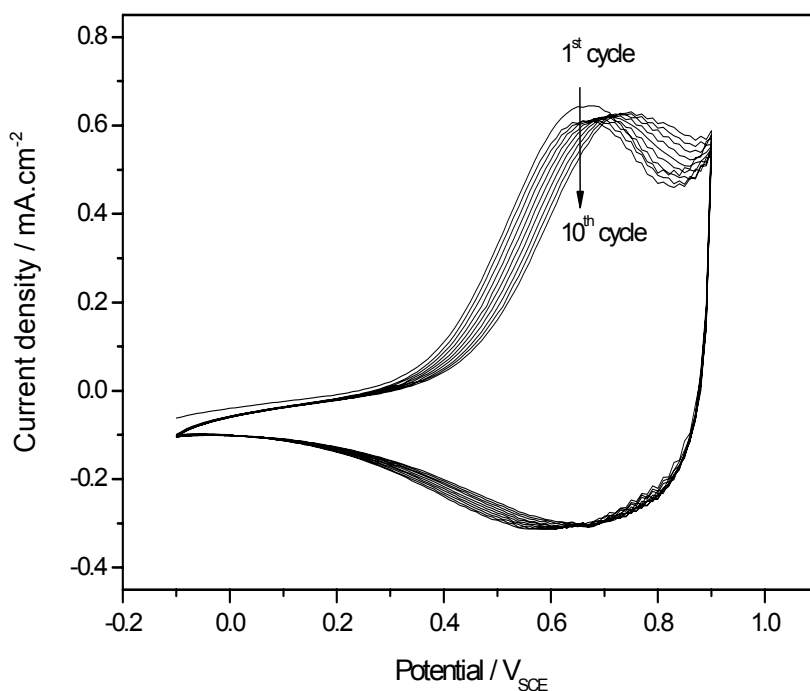


Fig.5.51 Cyclovoltammogram of PMT/TiO₂ (5.3 %) composite layer prepared by EPD on platinum (E = 20 V, 3 min)

For PMT/TiO₂ (5.3 %) composite layers on platinum, CVs are shown in Fig.5.51. The onset oxidation potential and the observed anodic peak potential of PMT were 0.4 V_{SCE} and +0.7 V_{SCE}, respectively. Both values were higher than that for the PMT in the PMT/TiO₂ (1.2 %) composites. The anodic peak current decreased from 0.65 mA.cm⁻² in the first cycle to 0.6 mA.cm⁻² in the 10 th cycle.

5.4.4 Electrochemical impedance spectroscopy

The Bode plots of PMT/TiO₂ composites can be explained with the same equivalent circuit used for PTh/TiO₂ composites (Fig.5.31). The impedance at low frequencies (<5 Hz) was attributed to the TiO₂ core, the impedance at higher frequencies (5 -1000 Hz) was attributed to the PMT shell (Fig.5.52). In the potential range of + 0.1 to + 0.3 V_{SCE}, the impedance of PMT/TiO₂ did not change, indicating that in this potential regime PMT was present in the reduced state. From + 0.35 to + 0.75 V_{SCE}, the PMT impedance was decreasing, PMT in the composite changed from the reduced semiconducting form to the oxidized conducting one. This is in agreement with the results from CV (Fig.5.51) and photocurrent-potential measurements (Fig.5.36). In the highest potential range (+ 0.8 to + 0.9 V_{SCE}) the impedance

of the PMT/TiO₂ was constant (Fig.5.52). The impedance measurements show that the PMT shell is electrochemically active as in the case of PTh shell. However, a change of capacitance of PMT during oxidation could be observed. A possible explanation was already presented for PTh/TiO₂ composite pellets [45].

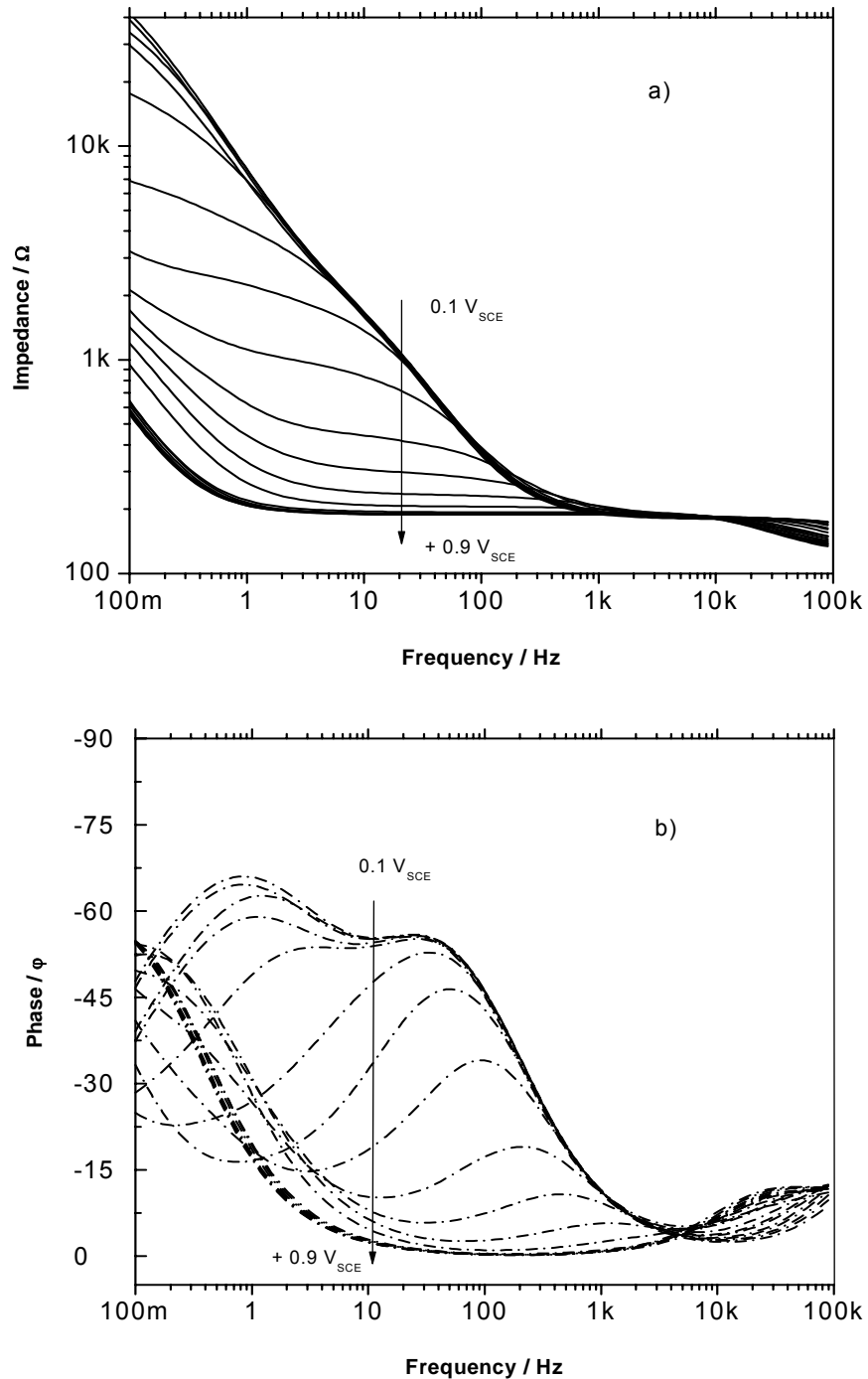


Fig.5.52 Bode plot of the impedance measurements of the PMT/TiO₂ (5.3 %) composite layer prepared by EPD on platinum (20 V, 2 min) in the potential region of -0.1 - 1.0V_{SCE};
a) Impedance and b) Phase

5.5 Characterization of PTh/ZnO nanocomposite films prepared by electrophoretic deposition

5.5.1 Morphology of composite particles

Fig.5.53 shows SEM pictures of the pure ZnO and the composite powders. The pure ZnO particles are crystalline (A) with a size range varying from several nanometers to several hundred nanometers. After reaction, the crystalline metal oxide core was covered by the amorphous PTh shell (B). As shown in Fig.5.53 (B), the coverage of the oxide particles was not complete. The coverage was limited by aggregation of the oxide particles before and during the polymerization. Moreover, granules of the pure polymer were formed in the bulk of the dispersion. However, the SEM observation gives the direct evidence for the oxidative polymerization of thiophene on ZnO particles.

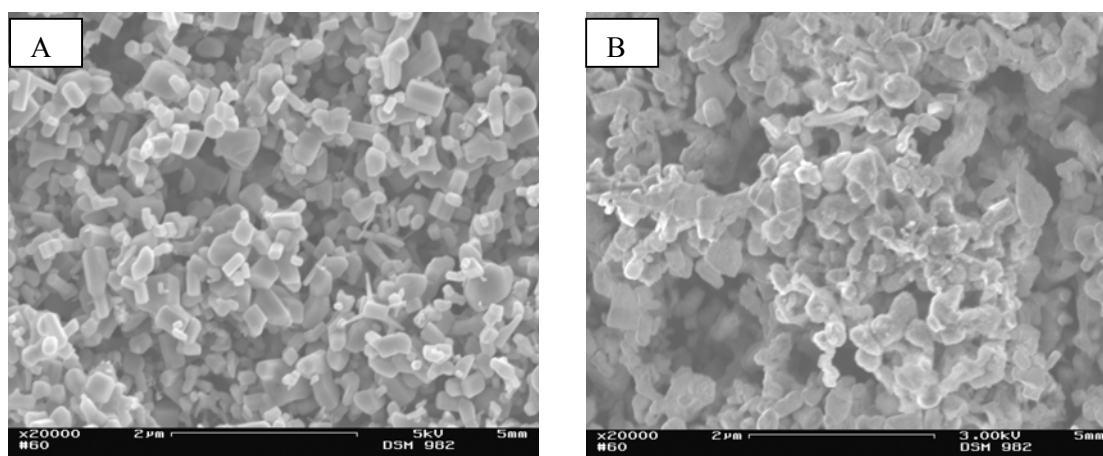


Fig.5.53 SEM micrographs of ZnO (A) and PTh/ZnO composite powder (B)

5.5.2 UV-VIS spectra

Fig.5.54 shows the optical spectra of PTh/ZnO particles in pressed pellets and deposited composite layers, respectively. A broad absorption band in the visible spectral region with the maximum around 530 nm corresponds to the absorption maximum of the reduced form of PTh. The UV absorption edge corresponds to the optical absorption of ZnO at about 380 nm. The optical spectra do not show any absorption in the near-IR region, supporting that PTh was in the reduced state. It follows from the optical absorption spectra that the electronic structure of both components of the composite does not change during the

electrophoretic deposition. Higher absorption values can be explained by a more dense structure in the case of pressed pellets.

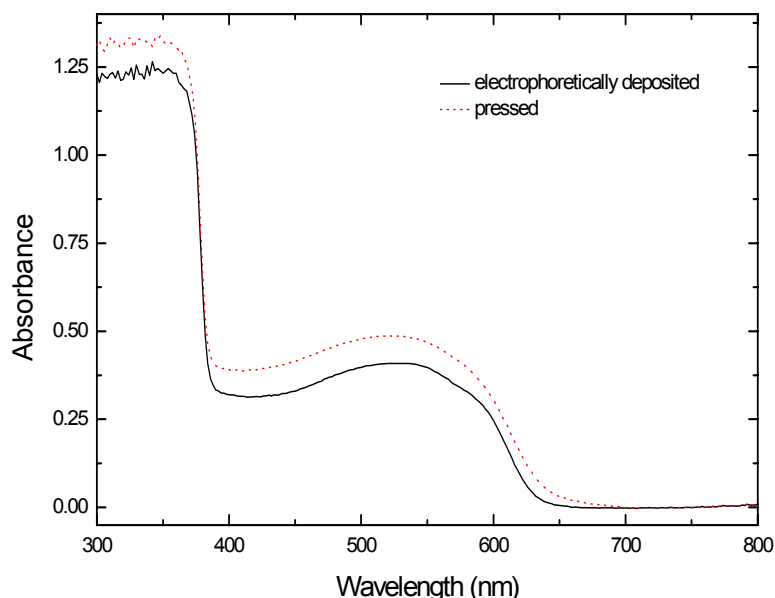


Fig.5.54 UV-VIS spectra of the electrodeposited composite layer (full line) and the pressed pellet (dashed line)

5.5.3 Photocurrent measurements

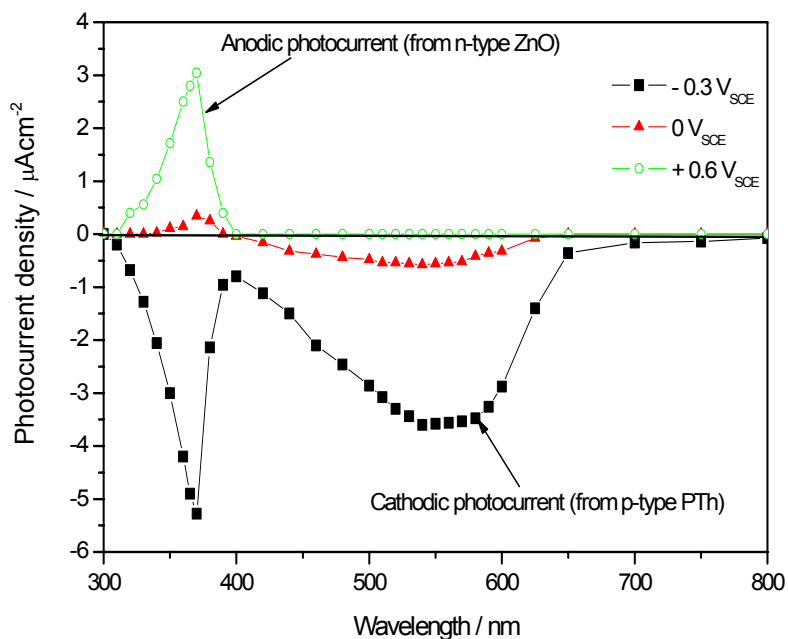


Fig.5.55 Photocurrent spectra of the PTh/ZnO composite layer deposited on ITO at various potentials vs. SCE

Photocurrents of the reduced form of PTh/ZnO composites are shown in Fig.5.55. Both anodic and cathodic photocurrents were observed depending on the applied potential, similarly to the cases of the PTh/TiO₂ and PMT/TiO₂ nanocomposites discussed before. A

large cathodic peak at 370 nm and $-0.3 \text{ V}_{\text{SCE}}$ was caused by ZnO absorption. The photocurrent maximum at 530 nm corresponds to the absorption maximum of PTh. At $+0.6 \text{ V}_{\text{SCE}}$, near the flatband potential of PTh, the cathodic photocurrent of PTh disappears. Photocurrent-potential plots at 530 nm are shown in Fig.5.56. The value of the flat-band potential of PTh was $E_{\text{fb}} = +0.53 \text{ V}_{\text{SCE}}$. Reversibility of the photocurrent-voltage dependence was observed if the potential was kept well below the flat-band potential of PTh in order to avoid over-oxidation.

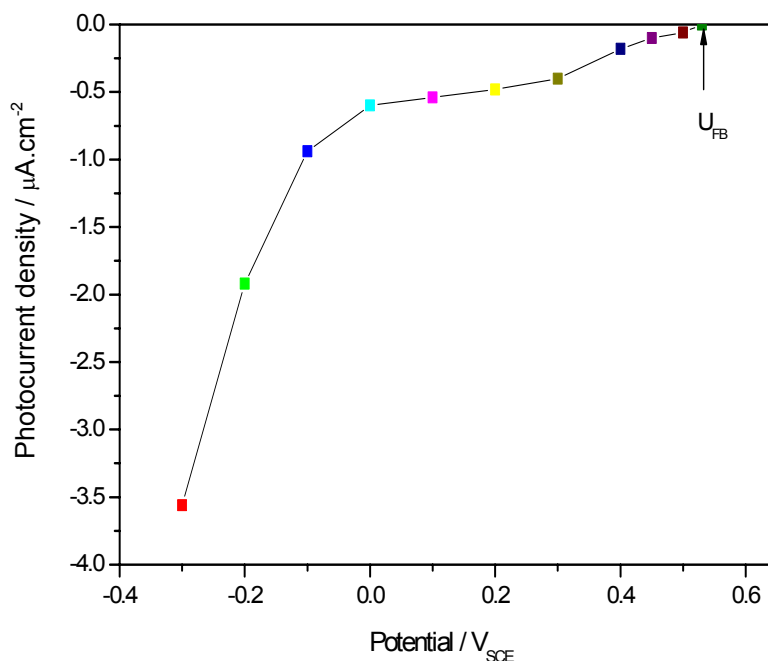


Fig.5.56 Photocurrent –potential dependence measured at 530 nm

5.5.4 Cyclic voltammetry

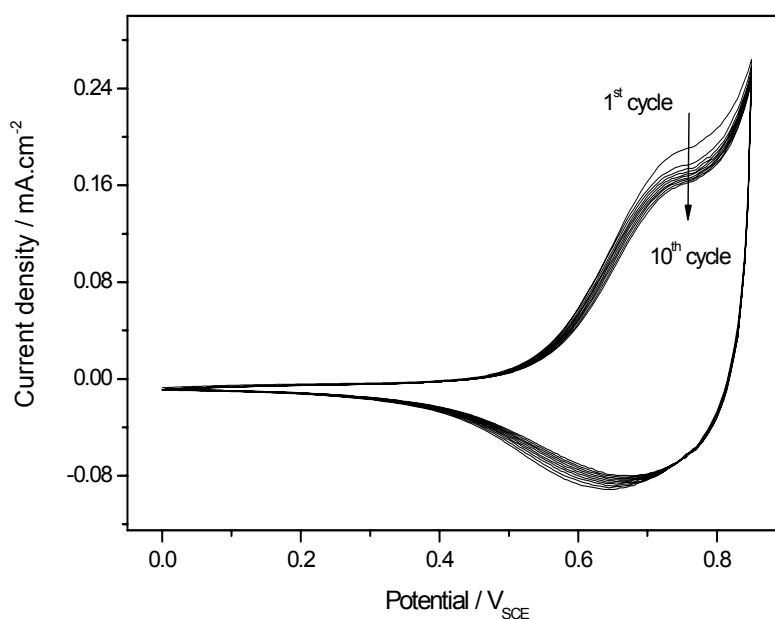


Fig.5.57 Cyclovoltammogram of the PTh/ZnO layer

Fig.5.57 shows the CV of a PTh/ZnO composite layer electrodeposited on a platinum electrode at a potential of 100V. The anodic peak potential of PTh was +0.75 V_{SCE} and was reversible. The anodic peak current decreases from 0.19 mA/cm^2 in the first cycle to 0.16 mA/cm^2 in the 10th cycle. The onset oxidation potential of PTh was approximately + 0.5 V_{SCE} . Again, the core showed no electrochemical activity.

5.5.5 Electrochemical impedance spectroscopy

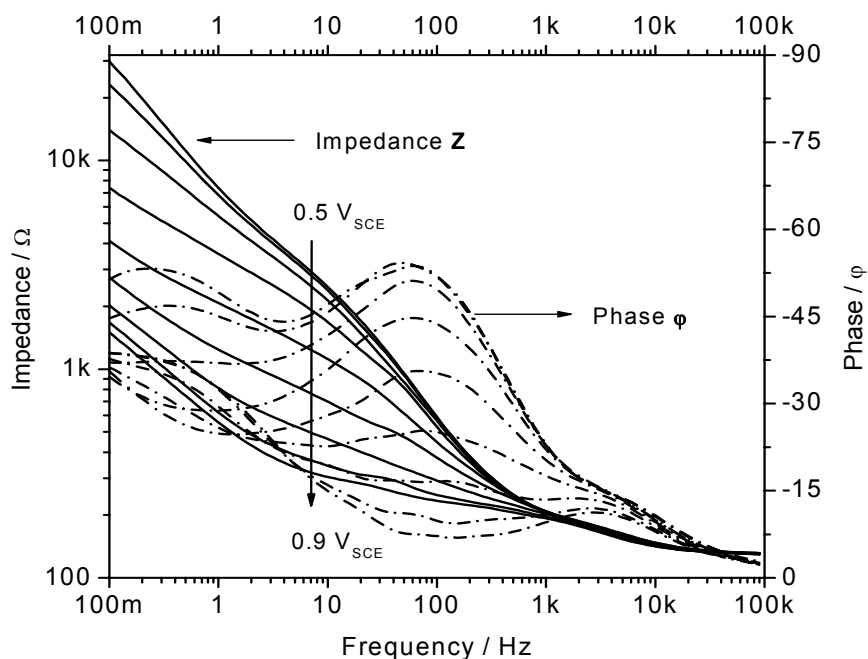


Fig.5.58 Electrochemical impedance spectra of the PTh/ZnO layer

EIS were measured at different potentials in the range of 0 - 1.0 V_{SCE} after a waiting time of 30 min at each applied potential value of 50 mV_{SCE} . Fig.5.58 shows the EIS of the PTh/ZnO layer deposited on a platinum electrode at applied 100 V. The analysis of the impedance spectra of the composite layer was made with the same equivalent circuit used for PTh/ TiO_2 composites (Fig.5.31). The impedance of the ZnO core is observed at low frequencies (<5 Hz) and the impedance of the PTh shell at higher frequencies (5-1000 Hz). The impedance of the electrolyte is shown in the frequency range of 10 - 100 kHz (Fig.5.58). In the potential range of 0 to + 0.5 V_{SCE} , the impedance of PTh/ZnO system does not change, indicating that in this potential regime PTh was still in the reduced state. From + 0.55 to + 0.9 V_{SCE} , the PTh impedance decreased, PTh in the composite was oxidized. Consequently, the impedance of the whole composite layer decreased. This is agreement with the results obtained from the CVs (Fig.5.57) and flatband potential measurements (Fig.5.56). Within this potential range, ZnO showed the electrochemical

properties of a semiconductor and it did not influence the impedance of the system. In the highest potential range tested (+ 0.9 to + 1.0 V_{SCE}) the impedance of the PTh/ZnO system was constant. The PTh shell had achieved doping saturation and its impedance did not change. Concerning the constant capacitance no Mott-Schottky could be found. Therefore, the charge carrier density (N_D) and flatband potential (E_{fb}) of PTh could not be determined via EIS measurements, similar to results reported before for other composites. The explanation was presented on page 78.

5.6 Characterization of PTh/Al₂O₃ nanocomposite films prepared by electrophoretic deposition

5.6.1 UV-VIS spectra

Fig.5.59 shows the optical spectra of pressed pellets of PTh/Al₂O₃(D) composite particles and composite layers. In the UV spectra, the absorption maxima are around 530 nm (2.3 eV) belonging to the absorption maximum of PTh. The optical spectra do not show any observable absorption in the near-IR spectral region, supporting that the PTh is in the reduced state. The results of the optical spectra are also in agreement with the spectroscopic data of the PTh film obtained by electrochemical polymerization [189].

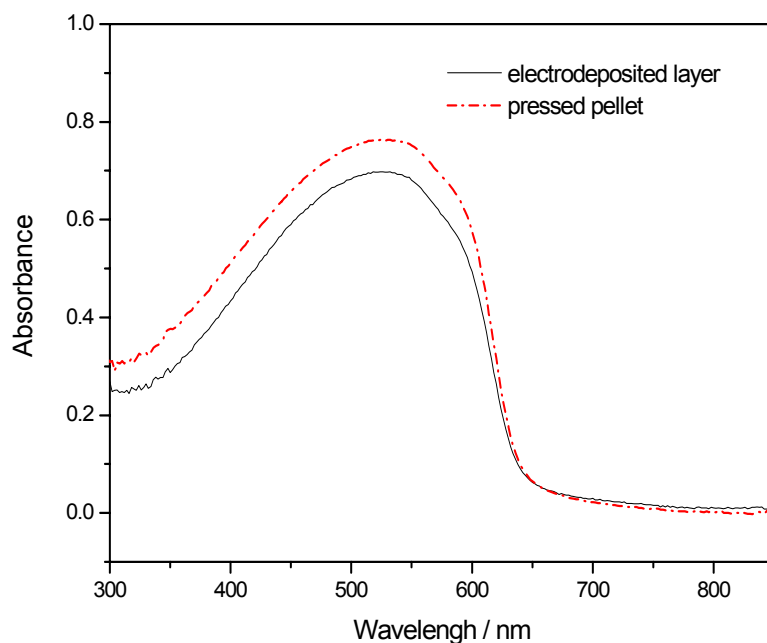


Fig.5.59 UV-VIS spectra of the deposited PTh/Al₂O₃(D) composite layer (full line) and of the pressed pellet (dashed line)

5.6.2 Photocurrent measurements

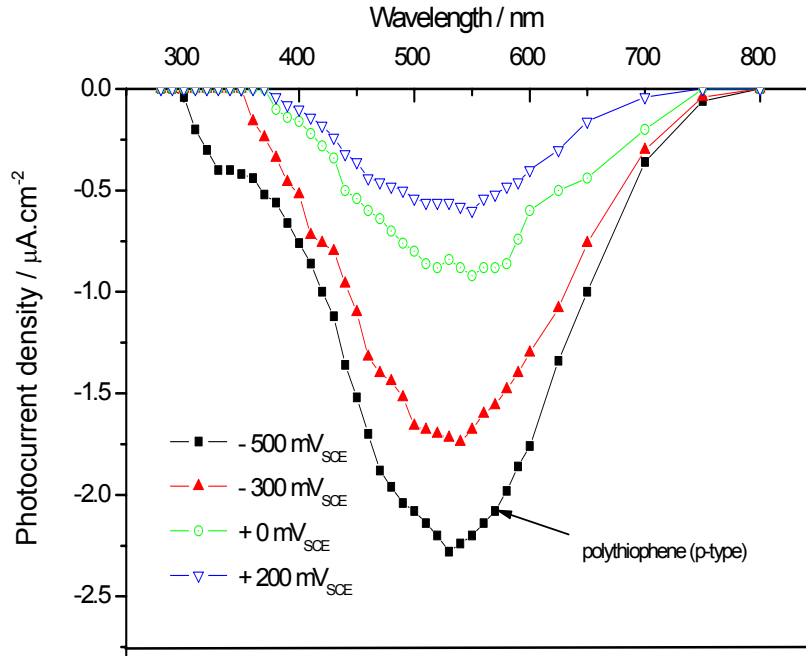


Fig.5.60 Photocurrent spectra of PTh/Al₂O₃(D) composite layers

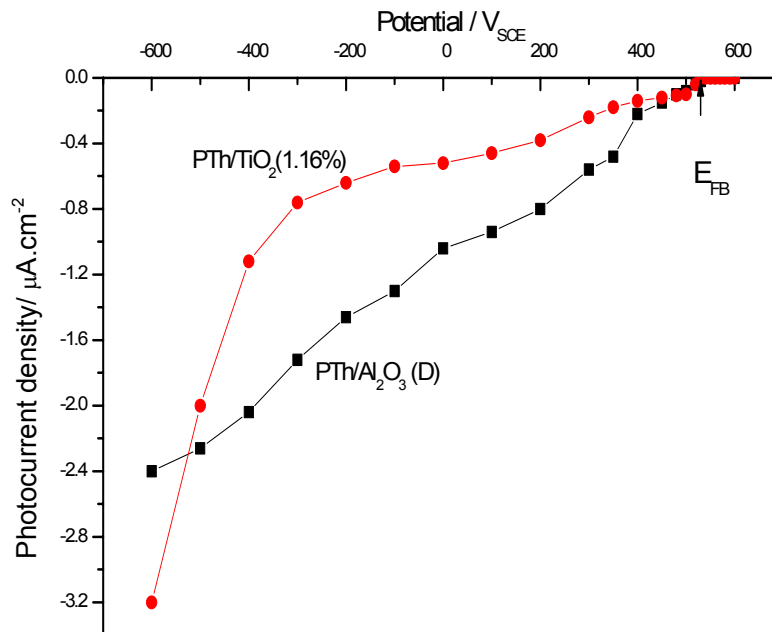


Fig.5.61 Photocurrent – potential dependence of PTh/Al₂O₃(D) composites in comparison with that of the PTh/TiO₂ composites

For inactive Al₂O₃(D) as core, only the cathodic photocurrent of PTh was found (Fig.5.60). The intensity of the photocurrent depends on the polarization potential. When the potential increases from -0.5 V to +0.2 V, the photocurrent at 500 nm decreases from $i = 1.2 \mu\text{A}$ to

0.3 μA . The maximum of the cathodic photocurrent at 500 nm was in agreement with the absorption spectrum obtained by UV-VIS spectroscopy.

The different photocurrent behaviour of TiO_2 and Al_2O_3 is explained by the different photoelectrochemical properties of the oxide core. In TiO_2 with its band gap of 3.2 eV photoelectrons and photoholes can be excited in the near UV spectral region. In Al_2O_3 as a typical insulator with a much larger bandgap photoexcitation in the experimental region is not possible (Fig.5.60).

The photocurrent-potential dependence of the PTh/ Al_2O_3 (D) composite layers at 500 nm is shown in Fig.5.61. From these results, the flat-band potential of PTh, $E_{\text{FB}} = 0.53 \text{ V}_{\text{SCE}}$ was determined. The value is similar to the onset potential of the photocurrent of PTh and agrees also with the onset oxidation potential of PTh observed with cyclic voltammetry.

The dependence of the photocurrent on the potential for the PTh/ Al_2O_3 (D) composites was different if compared with the PTh/ TiO_2 composites (Fig.5.61). The Al_2O_3 is a photoelectrically inactive material so that it is not influencing the photoelectrochemical behaviour of PTh. Otherwise; the TiO_2 core is photoelectrochemically active and obviously interacts with the polythiophene. The mechanism of this interaction is not yet clear.

5.6.3 Cyclic voltammetry

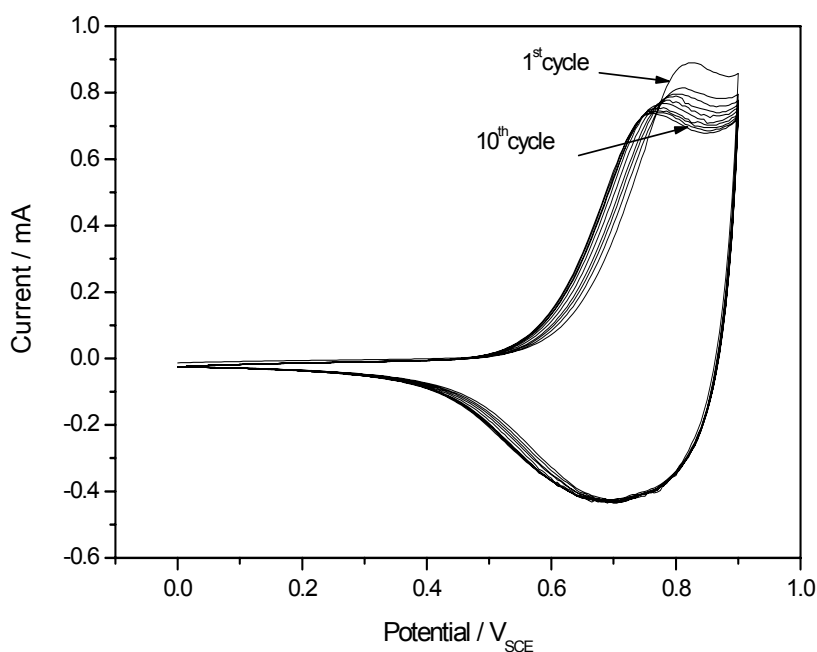


Fig.5.62 Cyclic voltammograms of a PTh/ Al_2O_3 (D) composite layer prepared by EPD on platinum ($E = 100 \text{ V}$, time = 3 min, $i = 0.2 - 0.3 \text{ mA}/\text{cm}^2$)

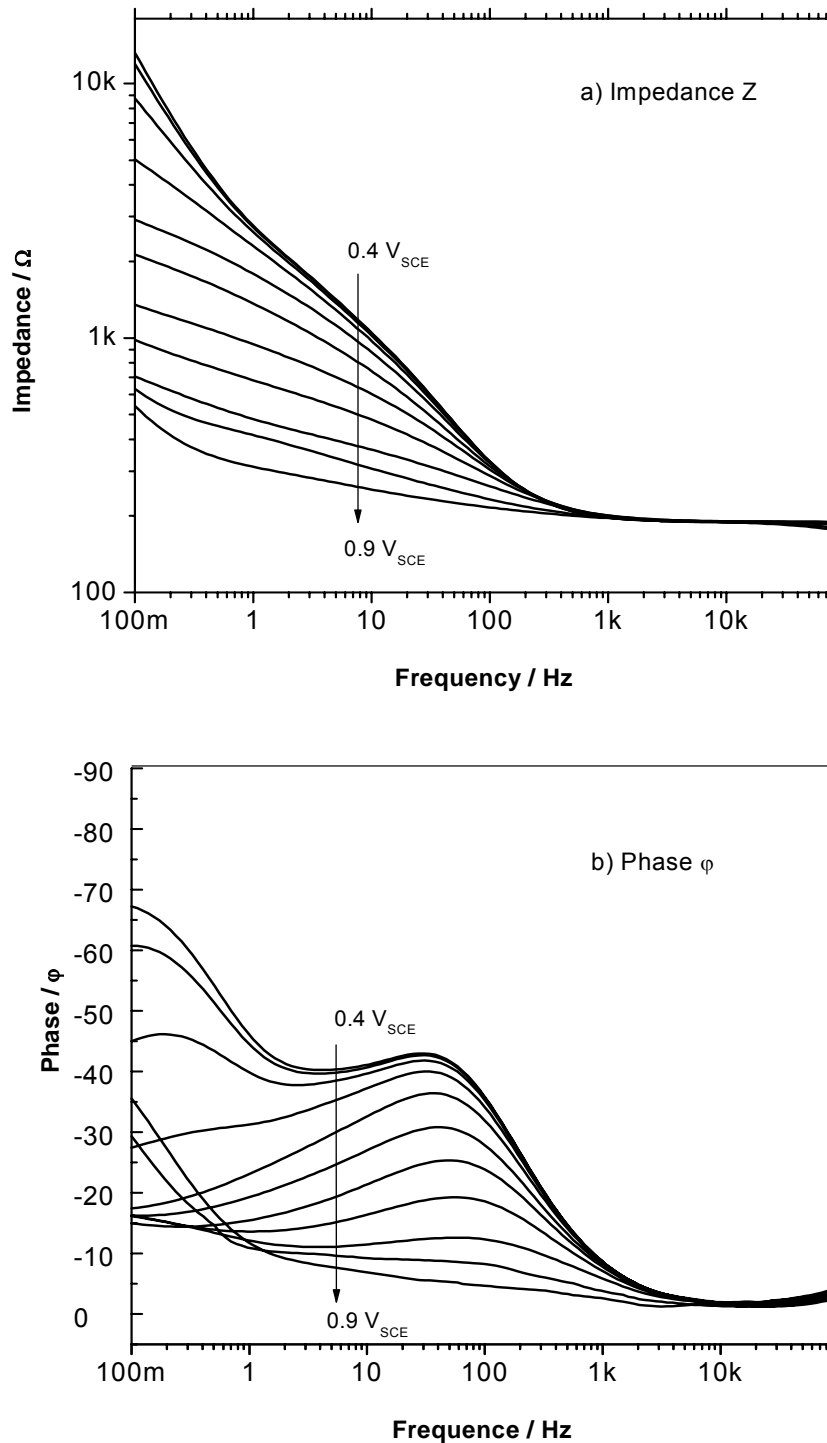


Fig.5.63 Bode plot of the impedance measurements of a PTh/Al₂O₃(D) composite layer prepared by EPD on platinum ($E = 100 \text{ V}$, $\text{time} = 3 \text{ min}$, $i = 0.2 - 0.3 \text{ mA/cm}^2$) in the potential region of $0.4 - 0.9 \text{ V}_{\text{SCE}}$; a) Impedance Z and b) Phase ϕ

Fig.5.62 shows the CV of a PTh/Al₂O₃(D) composite layer deposited on platinum at 100V. The observed onset potential of oxidation of PTh was $+0.75 \text{ V}_{\text{SCE}}$, in good agreement with

values given in the literature (+0.76 V_{SCE}) [45]. The onset oxidation potential was estimated from CVs by an extrapolation of the linear part of the CV curve to the zero current value. The anodic peak current decreased from 0.9 mA (about 0.45 mA/cm²) in the first cycle to 0.7 mA (about 0.35 mA/cm²) in the 10 th cycle.

5.6.4 Electrochemical impedance spectroscopy

Impedance spectra of a PTh/Al₂O₃(D) composite layer were measured every 30 min in the potential range between 0 and 0.9 V_{SCE} in steps of 50 mV. Each measurement took 30 min. The impedance spectra for 0.4-0.9 V_{SCE} are shown in Fig.5.63. The spectra are similar to spectra of PTh/TiO₂ composite layers (Section 5.1). Differences with older results [45] are explained by different film thickness and film structure obtained by the different preparation methods. The equivalent circuit of Fig.5.31 was used for analysing the impedance spectra. The impedance of the Al₂O₃ core dominated at low frequencies (<1 Hz) and the impedance of the PTh shell at higher frequencies (1-1000 Hz). The capacitance did not change with the potential. This behaviour could be explained in the same manner as for PTh/TiO₂ composites with the small amount of PTh in the composite (around 1%) and the small thickness of the PTh-film. Therefore, the capacitance of the composite layer is nearly constant in the whole potential range. Hence, no Mott-Schottky plot was possible and the charge carrier density (N_D) and the flatband potential (E_{FB}) of PTh in the composite could not be determined by EIS measurements. Otherwise the resistance of the film was changing with increasing potential, PTh in the composite changed from the reduced semiconducting form to the conducting oxidized form in agreement with the results from CV (Fig.5.62). This is a main result of these experiments (CV and EIS) that the electrochemical activity of the polythiophene film survived EPD despite the application of the high voltage of 100 V.

5.7 Electrophoretic deposition of poly (3-octylthiophene)

In Ref. [151, 152, 153, 154], some soluble polythiophene thin films were prepared by the EPD procedure. In this study, regiorandom poly (3-octylthiophene) (P3OT) was used. The suspension was made through a simple pouring method: 1 unit of 1 g/l chloroform solution of P3OT was poured into 9 units of acetonitrile. In acetonitrile P3OT was insoluble. Therefore, a suspension of 0.1 g/l colloidal P3OT particles in chloroform / acetonitrile (1:9) mixture was formed. The EPD was carried out at 50 V. The P3OT film was deposited on the cathode. It indicates that the P3OT colloidal particles were positively charged. Since P3OT is a p-type semiconductor and no surfactants were used in the suspension, this result

seems reasonable. However, the zeta potential of the P3OT in the suspension is very small because it could not be deposited at a potential lower than 30 V. The absorption spectrum of P3OT colloidal suspension was different from that of the chloroform solution as shown in Fig.5.64. The absorption spectrum of the suspension is almost the same as the solid polymer film.

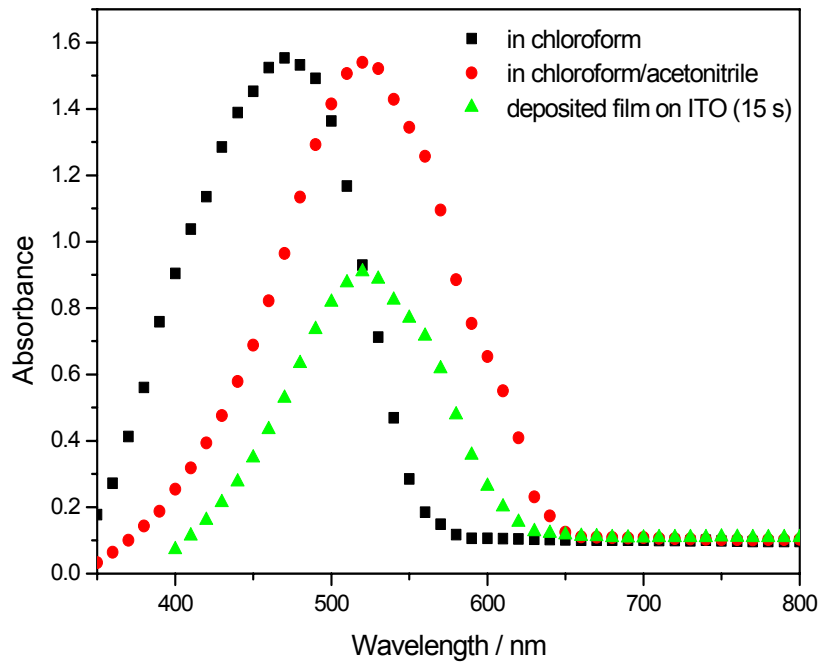


Fig.5.64 Optical absorption spectra of a P3OT solution, suspension and of a deposited layer

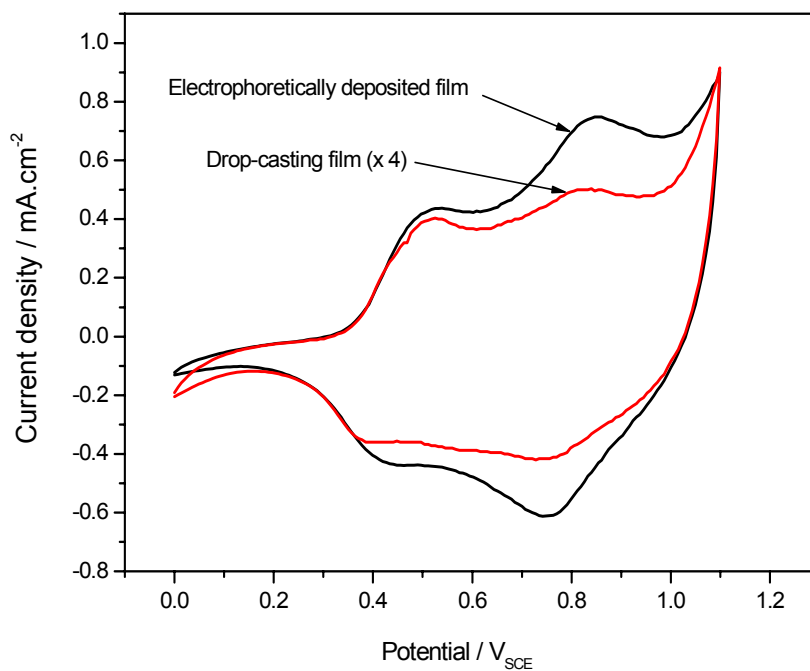


Fig.5.65 Cyclic voltammograms of the deposited and drop-casting P3OT films

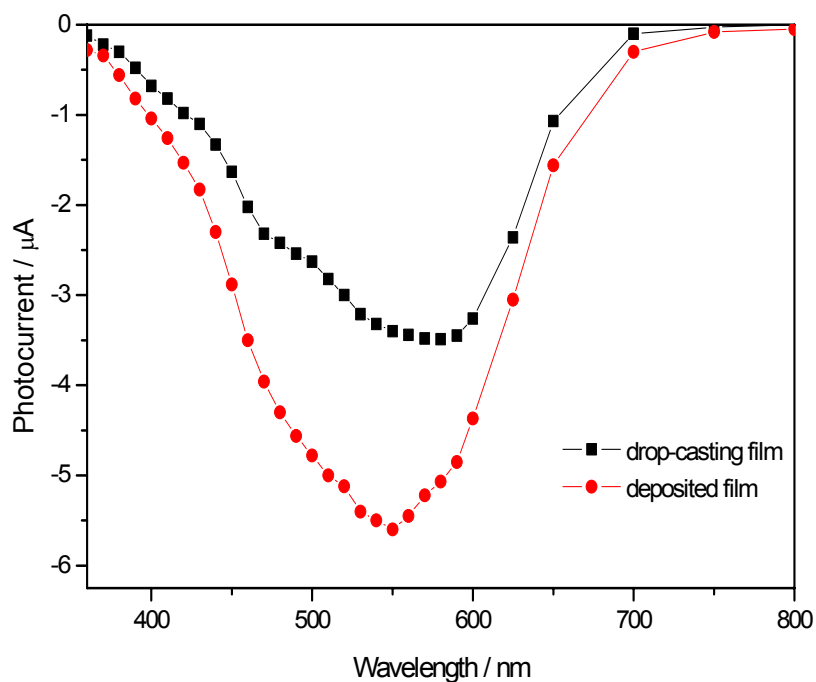


Fig.5.66 Photocurrent of the deposited and cast P3OT films at $-0.5 V_{SCE}$

CVs of the P3OT films prepared on platinum by EPD and by drop-casting are shown in Fig.5.65. The CVs of the electrodeposited film was very similar to that of the cast P3OT film. Two oxidation peaks at 0.5 and 0.8 V_{SCE} were observed, corresponding to the regioregular P3OT. The current density of the deposited film was higher because it was thicker than the film prepared by casting (see Fig.5.65). Photocurrent spectra of the deposited P3OT film prepared on ITO are shown in Fig.5.66. Its magnitude was higher than the photocurrent obtained from the film prepared by casting. The current density and photocurrent of the deposited P3OT film were always higher than that of the drop-casting P3OT film. This can be explained by the higher thickness of the deposited film. From CV curves, the flatband potential of P3OT of approximately 0.4 V_{SCE} and the bandgap energy of the P3OT of approximately 1.82 eV were determined.

Conclusion and future work

To broaden possible applications of conducting polymers, nanocomposites of conducting polymers with oxide particles are a promising solution. The chemical preparation of these composites is easy even on a large scale. In the investigation, the oxidative polymerization of monomers in suspensions of nano-sized oxide particles was used. A shell of a conducting polymer matrix was formed around a metal oxide core, generating conducting polymer composites with core shell structure.

The morphological structure of the synthesized composite particles was determined by scanning electron microscopy and electron transmission microscopy. Scanning electron microscopy shows that the coverage of the oxide particle with the conducting polymer is not complete. Transmission electron microscopy technique shows that the crystalline oxide core is covered by a 4-5 nm thick amorphous conducting polymer shell. The thickness of the p/n heterojunction was 5 nm. The chemical structure of the composites was studied by Raman spectroscopy. The dark conductivity of PTh/TiO₂ and PMT/TiO₂ composites, measured on the pressed-pellets at 300 K using the van der Pauw four-point method shows that the conducting polymers are in the semiconducting neutral form. The ratio of conducting polymer mass determined by thermogravimetric analysis gave values between 1 and 5 % polymer.

The electrophoretic deposition process was used to prepare nanocomposite layers. Suspensions of different core-shell nanoparticles in ethanol, ethanol/water, water, butanol, propanol, glycerol and ethylacetate were prepared. Composite layers with higher qualities were deposited at higher potentials (10 up to 100 V). Composites could be deposited on different substrates (platinum, gold, aluminium, ITO, mild steel) from different solvents (ethanol, ethanol/water, water, butanol, isopropanol) with a concentration between 0.5 and 5g.l⁻¹. Almost of the formed composite layers were mechanically stable. In other solvents (ethylacetate, toluene, glycerol) composites could not be deposited. No deposition of PTh/SiO₂ composites was possible.

For investigating the kinetics of EPD, a QCM was used. Although QCM is a generally used method to study the electrochemical deposition of various materials, until now it has not been applied for in-situ studies of the EPD procedure. The method is based on the frequency shift of a quartz sheet during deposition.

It was found that:

- The deposited mass was proportional to the square root of deposition time.
- The rate of deposition depends on the conductivity of the colloidal suspension.
- The rate of deposition depends on the zeta potential of the composite particles. The metal oxide (TiO_2 , Al_2O_3 , ZnO) composites possessed high and positive zeta potentials, with these composites EPD was possible. On other hand, the silicon composites had small and negative zeta potentials, no deposition occurred.
- The hydrolysis of water might be influent on the EPD process.

Many effects influence the mechanical properties of the deposited layers. Effects investigated were potential, solvent, character, substrate, the deposition time, and size of composite particles and nature of conducting polymers.

The films were investigated using the following methods:

- UV-VIS optical absorption spectra of pressed pellets and electrodeposited composite layers showed the absorption peaks of the conducting polymer shells and of the oxide cores. In the case of an Al_2O_3 core, only the absorption of the conducting polymers was observed. The deposited layers did not show optical absorption in the near-IR region, which would have been expected for the oxidized state of the polymer.
- The electrochemical behaviour of the composite layers was investigated by cyclic voltammetry and electrochemical impedance spectroscopy. The redox behaviour of the conducting polymers was reversible and stable. The oxidation potential of the conducting polymer components was determined by cyclic voltammetry. The oxidation process was studied in more detail by electrochemical impedance spectroscopy. The impedance data show that the conducting polymer shell remained electrochemically active also after electrophoretic deposition at high potentials (10 - 100 V). The core showed no electrochemical activity in the positive potential range of the investigation.
- The photoelectrochemical properties of the deposited composite layers were studied by photocurrent spectroscopy. With semiconducting cores (TiO_2 and ZnO) positive as well as negative photocurrents were observed in the oxide absorption region around 340 nm.

Negative photocurrents at 500-530 nm belonged to the conducting polymer component. Using insulating Al_2O_3 , only cathodic photocurrents were observed. From the photocurrent measurements, the flatband potential and the bandgap energy of the conducting polymers could be determined.

- A sandwich cell composed of PTh/ TiO_2 nanocomposite layers between ITO and Al (or Au) electrodes was developed. An absorption at 400 nm was found. It was contributed to the p/n junction of the composite material. The ideality factor of the diode was 4.4.

The results from electrochemical and photoelectrochemical investigations showed that the conducting polymer remained active after deposition. Therefore, the electrophoretic deposition is a suitable process to prepare stable films of conducting polymer / metal oxide composite materials. So far the composite preparation and the deposition process were not optimized. Nevertheless, the qualities of the layers were sufficient for testing photoelectrically active devices. In the future, the conditions of the composite preparation must be improved for a best performance of possible applications.

References

-
- [1] P. Chandrasekhar, *Conducting Polymers, Fundamentals and Applications*, Kluwer Academic Publishers, 1999
- [2] A. G. MacDiarmid, "Synthetic Metals": A novel role for organic polymers (Nobel lecture), *Angew. Chem. Int. Ed.*, 2001, 40, 2581 - 2590
- [3] A. J. Heeger, "Semiconducting and metallic polymers: the fourth generation of polymeric materials", *Synthetic metals*, 2002, 125, 23-42
- [4] D. Fichou, *Handbook of oligo- and polythiophene*, Wiley-VCH, Weinheim, 1999
- [5] T. A. Skotheim, R. L. Elsenbaumer, J. R. Reynolds, *Handbook of conducting polymers*, Marcel Dekker, Inc., 1998
- [6] J. Margolis, *Conductive polymers and plastics*, Chapman and Hall, 1989
- [7] U. Rammelt, P. T. Nguyen, W. Plieth, Protection of mild steel by modification with films of polymethylthiophene, *Electrochim. Acta*, 2001, 46, 4251-4257
- [8] S. P. Speakman, G. G. Rozenberg, K. J. Clay, W. I. Milne, A. Ille, I. A. Gardner, E. Bresler and J. H. G. Steinke, High performance organic semiconducting thin film: ink jet printed polythiophene [*rr*-P3HT], *Organic electronics*, 2001, 2 (2), 65-73
- [9] L. Alcacer, *Conducting polymers special applications*, D. Reidel publishing company, 1987
- [10] V. Saxena and B. D. Malhotra, Aspects of conducting polymers in molecular electronics, *Current applied physics*, 2003, 3 (2-3), 293-305
- [11] M. Kurian, M. E. Galvin, P. E. Trapa, D. R. Sadoway and A. M. Mayes, Single-ion conducting polymer-silicate nanocomposite electrolytes for lithium battery applications, *Electrochim. Acta*, 2005, 50 (10), 2125-2134
- [12] Basudam Adhikari and Sarmishtha Majumdar, Polymers in sensor applications, *Progress in Polymer Science*, 2004, 29 (7), July 2004, 699-766
- [13] C. Weidlich, K.-M. Mangold and K. Jüttner, EQCM study of the ion exchange behaviour of polypyrrole with different counterions in different electrolytes, *Electrochim. Acta*, 2005, 50 (7-8), 1547-1552
- [14] G. Han and G. Shi, High-response tri-layer electrochemical actuators based on conducting polymer films, *J. Electroanal. Chem.*, 2004, 569 (2), 169-174
- [15] A. Mirmohseni, W. E. Price and G. G. Wallace, Electrochemically controlled transport across conducting polymer composites - Basis of smart membrane materials, *Polymer Gels and Networks*, 1993, 1 (1), 61-77

-
- [16] R. Gangopadhyay and A. De, Conducting polymer nanocomposites: A brief overview, *Chem. Mater.* 2000, 12, 608-623
- [17] F. Caruso, Nanoengineering of particle surfaces, *Adv. Mater.*, 2001, 13 (1), 11-22
- [18] K. Rajeshwar, N. R. de Tacconi, and C. R. Chenthamarakshan, Semiconductor-based composite materials: preparation, properties, and performance, *Chem. Mater.*, 2001, 13, 2765-2782
- [19] S. P. Armes, S. Gottesfeld, J. G. Beery, F. Garzon and S. F. Agnew, Conducting polymer - colloidal silica composites, *Polymer*, 1991, 32 (13), 2325-2330
- [20] R. Flitton, J. Johal, S. Maeda and S. P. Armes, Synthesis of Colloidal Dispersions of Polypyrrole-Silica Nanocomposites Using "Stringy" Silica Particles, *J. Coll. Interfac. Sci.*, 1995, 173 (1), 135-142
- [21] S. Maeda and S. P. Armes, Surface area measurements on conducting polymer-inorganic oxide nanocomposites, *Synth. Met.*, 73 (2), 151-155
- [22] M. D. Butterworth, S. A. Bell, S. P. Armes and A. W. Simpson, Synthesis and Characterization of Polypyrrole – Magnetite – Silica Particles, *J. Coll. Interfac. Sci.*, 1996, 183 (1), 91-99
- [23] S. P. Lascelles, G. P. McCarthy, M. D. Butterworth, S. P. Armes, Effect of synthesis parameters on the particles size, composition and colloid stability of polypyrrole-silica nanocomposite particles, *Coll. Polym. Sci.*, 1998, 276, 893-902
- [24] C. Perruchot, M. M. Chehimi, M. Delamar, J. A. Eccles, T. A. Steele, C. D. Mair, SIMS analysis of conducting polypyrrole-silica gel composites, *Synth. Met.*, 2000, 113, 53-63
- [25] L. Hao, C. Zhu, C. Chen, Peng Kang, Y. Hu, W. Fan, Z. Chen, Fabrication of silica core-conductive polymer polypyrrole shell composite particles and polypyrrole capsule on monodispersed silica templates, *Synth. Met.*, 2003, 139, 391-396
- [26] M. G. Han and S. P. Armes, Synthesis of poly (3, 4-ethylenedioxythiophene)/silica colloidal nanocomposites, *Langmuir*, 2003, 4523-4526
- [27] R. Partch, S. G. Gangolli, E. Matijevic, W. Cal and S. Arajs, Conducting polymer composites: I. Surface-induced polymerization of pyrrole on iron (III) and cerium(IV) oxide particles, *J. Coll. Interfac. Sci.*, 1991, 144 (1), 27-35
- [28] M. Kryszewski and J. K. Jeszka, Nanostructured conducting polymer composites - superparamagnetic particles in conducting polymers, *Synth. Met.*, 1998, 94 (1), 99-104
- [29] R. Gangopadhyay and A. De, Polypyrrole–ferric oxide conducting nanocomposites: I. Synthesis and characterization, *Eur. Polym. J.*, 1999, 35 (11), 1985-1992

-
- [30] J. Deng, X. Ding, W. Zhang, Y. Peng, J. Wang, X. Long, P. Li and A. S. C. Chan, Magnetic and conducting Fe₃O₄-cross-linked polyaniline nanoparticles with core-shell structure, *Polym.*, 2002, 43 (8), April 2002, 2179-2184
- [31] K. Suri, S. Annapoorni, R. P. Tandon, C. Rath and V. K. Aggrawal, Thermal transition behaviour of iron oxide-polypyrrole nanocomposites, *Current Appl. Phys.*, 2003, 3 (2-3), 209-213
- [32] K. Sunderland, P. Brunetti, L. Spinu, J. Fang, Z. Wang and W. Lu, Synthesis of γ -Fe₂O₃/ polypyrrole nanocomposite materials, *Mater. Lett.*, 2004, 58 (25), 3136-314
- [33] M. Wan, W. Zhou, J. Li, Composite of polyaniline containing iron oxides with nanometer size, *Synth. Met.*, 1996, 78, 27-31
- [34] A. Chen, H. Wang, B. Zhao, X. Li, The preparation of polypyrrole-Fe₃O₄ nanocomposites by the use of common iron effect, *Synth. Met.*, 2003, 139, 411-415
- [35] K. Gurunathan, D. C. Trivedi, Studies on polyaniline and colloidal TiO₂ composites, *Mater. Lett.*, 2000, 45, 262-268
- [36] P. Somani, B. B. Kale, D. P. Amalnerkar, Charge transport mechanism and effect of poling on the current-voltage characteristics of conducting polyaniline-BaTiO₃ composites, *Synth. Met.*, 1999, 106, 53-58
- [37] P. R. Somani, R. Marimuthu, U. P. Mulik, S. R. Sainkar, D. P. Amalnerkar, High piezoresistivity and its origin in conducting polyaniline / TiO₂ composites, *Synth. Met.*, 1999, 45-52
- [38] S. J. Su, N. Kuramoto, Processable polyaniline-titanium dioxide nanocomposites: effect of titanium dioxide on the conductivity, *Synth. Met.*, 2000, 114, 147-153
- [39] X. Li, W. Chen, C. Bian, J. He, N. Xu, G. Xue, Surface modification of TiO₂ nanoparticles by polyaniline, *Appl. Surf. Sci.*, 2003, 217, 16-22
- [40] P. R. Somani, R. Marimuthu, A. B. Mandale, Synthesis, characterization and charge transport mechanism in conducting polyaniline/V₂O₅ composites, *Polym.*, 2001, 42, 2991-3001
- [41] S. S. Ray, Synthesis and evaluation of conducting polypyrrole/Al₂O₃ nanocomposites in aqueous and non-aqueous medium, *Mater. Res. Bull.*, 2002, 37, 813-824
- [42] B. H. Kim, J. H. Jung, J. W. Kim, H. J. Choi, J. Joo, Physical characterization of polyaniline-Na⁺-montmorillonite nanocomposite intercalated by emulsion polymerization, *Synth. Met.*, 2001, 117, 115-118

-
- [43] B. H. Kim, J. H. Jung, S. H. Hong, J. Joo, A. J. Epstein, K. Mizoguchi, J. W. Kim and H. J. Choi, Nanocomposite of polyaniline and Na⁺-montmorillonite clay, *Macromolecules*, 2002, 35, 1419-1423
- [44] K. Ramachandra and M. M. Lerner, Electrochemical characterization of a polypyrrole / montmorillonite nanocomposite, *J. Electrochem. Soc.*, 1997, 144 (11), 3739-3743
- [45] N. Hebestreit, J. Hofmann, U. Rammelt, W. Plieth, Physical and electrochemical characterization of nanocomposite formed from polythiophene and titaniumdioxide, *J. Electrochem. Acta*, 2003, 48, 1779-1788
- [46] K. Gurunatha, D. P. Amalnerka, D. C. Trivedi, Synthesis and characterization of conducting polymer composite (Pan/TiO₂) for cathode material in rechargeable battery, *Mater. Lett.*, 2003, 57, 1642-1648
- [47] U. Rammelt, N. Hebestreit, A. Fikus and W. Plieth, Investigation of polybithiophene / n-TiO₂ bilayers by electrochemical impedance spectroscopy and photoelectrochemistry, *Electrochimica Acta*, 2001, 46 (15), 2363-2371
- [48] Y. Saito, T. Kitamura, Y. Wada, S. Yanagida, Poly (3,4-ethylenedioxythiophene) as a hole conductor in solid state dye sensitized solar cells, *Synth. Met.*, 2002, 131, 185-187
- [49] Yasuteru Saito, Takahiro Azechi, Takayuki Kitamura, Yasuchika Hasegawa, Yuji Wada and Shozo Yanagida, Photo-sensitizing ruthenium complexes for solid state dye solar cells in combination with conducting polymers as hole conductors, *Coordination Chem. Reviews*, 2004, 248 (13-14), 1469-1478
- [50] K. Idla, O. Inganäs, M. Strandberg, Good adhesion between chemically oxidized titanium and electrochemically deposited polypyrrole, *Electrochim. Acta*, 2000, 45, 2121-2130
- [51] T. Ogawa, T. Kitamura, T. Shibuya, K. Hoshino, Characterization and material conditions of conducting polymer / titanium oxide hybrid systems used for dinitrogen fixation under ordinary pressure and temperature, *Electrochem. Communication*, 2004, 6, 55-60
- [52] K. Kajihara, K. Tanaka, K. Hirao and N. Soga, Photovoltaic effect in titanium dioxide / polythiophene cell, *Jpn. J. Appl. Phys.*, 1997, 36, 5537-5542
- [53] G. Wang, H. Chen, H. Zhang, C. Yuan, Z. Lu, G. Wang, W. Yang, TiO₂ / polypyrrole diodes prepared by electrochemical deposition of polypyrrole on microporous TiO₂ film, *Appl. Surf. Sci.*, 1998, 135, 97-100

-
- [54] Y. Hao, M. Yang, W. Li, X. Qiao, L. Zhang, S. Cai, A photoelectrochemical solar cell based on ZnO / dye / polypyrrole film electrode as photoanode, *Solar energy Mater. & solar cells*, 2000, 60, 349-359
- [55] H. Yoneyama, K. Kawai, N. Mihara, S. Kuwabata, Electrochemical synthesis of polypyrrole films containing TiO₂ powder particles, *J. Electrochem. Soc.*, 1990, 137 (6), 1793-1795
- [56] F. Beck, M. Dahlhaus and N. Zahedi, Anodic codeposition of polypyrrole and dispersed TiO₂, *Electrochim. Acta*, 1992 (7), 1265-1272
- [57] F. Beck, M. Dahlhaus, Anodic formation of polypyrrole / tungsten trioxide composites, *J. Appl. Electrochem.*, 1993, 23, 781-789
- [58] Y-C Liu and M-D Ger, Modification of electropolymerized polypyrrole with Na⁺ montmorillonite, *Chem. Phys. Lett.*, 2002, 362 (5-6), 491-496
- [59] B. Garcia, A. Lamzoudi, F. Pillier, H. Nguyen Thi Le, and C. Deslouis, Oxide / polypyrrole composite film for corrosion protection of iron, *J. Electrochem. Soc.*, 2002, 149 (12), 560-566
- [60] D. M. Lenz, M. Delamar, C. A. Ferreira, Application of polypyrrole / TiO₂ composite films as corrosion protection of mild steel, *J. Electroanal. Chem.*, 2003, 540, 35-44
- [61] A. C. Arango, S. A. Carter, P. J. Brock, Charge transfer in photovoltaics consisting of interpenetrating networks of conjugated polymer and TiO₂ nanocomposites, *Appl. Phys. Lett.*, 1999, 74 (12), 1698-1700
- [62] D. Gebeyehu, C. J. Brabec, F. Padinger, T. Fromherz, S. Spiekermann, N. Vlachopoulos, H. Schindler and N.S Sariciftci, Solid state dye-sensitized TiO₂ solar cells with poly(3-octylthiophene) as hole transport layer, *Synth. Met.*, 2001, 121, 1549-1550
- [63] M. Kaneko, K. Takayama, S. S. Pandey, W. Takashima, T. Endo, M. Rikukawa, and K. Kaneto, Photovoltaic cell using mobility poly(alkylthiophene)s and TiO₂, *Synth. Met.*, 2001, 121, 1537-1538
- [64] C. D. Grant, A. M. Schwartzberg, G. P. Smestad, J. Kowalik, L. M. Tolbert, J. Z. Zhang, *J. Electroanal. Chem.*, 2002, 522, 40-48
- [65] W. U. Huynh, X. Peng, and A. P. Alivisatos, CdSe nanocrystal rods/poly(3-hexylthiophene) composite photovoltaic devices, *Adv. Mater.*, 1999, 11 (11) 923-927
- [66] D. Gebeyehu, C. J. Brabec, N.S Sariciftci, D. Vangeneugden, R. Kiebooms, D. vanderzande, F. Kienberger, H. Schindler, Hybrid solar cells based on dye-sensitized nanoporous TiO₂ electrodes and conjugated polymers as hole transport materials, *Synth. Met.*, 2002, 125, 279-287

-
- [67] P. M. Sirimanne, T. Shirata, L. Damodare, Y. Hayashi, T. Sogar, T. Jimbo, An approach for utilization of organic polymer as a sensitizer in solid-state cells, *Solar Energy Mater. & Solar Cells*, 2003, 77, 15-24
- [68] C. D. Grant, A. M. Schwartzberg, G. P. Smestad, J. Kowalik, L. m. Tolbert, J. Z. Zhang, Optical and electrochemical characterization of poly(3-undecyl-2,2'-bithiophene) in thin film solid state TiO₂ photovoltaic solar cells, *Synth. Met.*, 2003, 132, 197-204
- [69] T. Akiyama, A. Miyazaki, M. Sutoh, I. Ichinose, T. Kunitake, S. Yamada, Fabrication of porphyrin-titanium oxide-fullerene, assemblies on an ITO electrode and their photocurrent response, *Colloids Surf., A*, 2000, 169, 137-141
- [70] T. J. Savenije, J. M. Warman, A. Goossens, Visible light sensitisation of titanium dioxide using a phenylene vinylene polymer, *Chem. Phys. Lett.*, 1998, 287, 148-153
- [71] J. E. Kroeze, T. J. Savenije, M. J. W. Vermeulen, and J. M. Warman, Contactless determination of the photoconductivity action spectrum, exciton diffusion length, and charge separation efficiency in polythiophene-sensitized TiO₂ bilayers, *J. Phys. Chem. B*, 2003, 107, 7696-7705
- [72] S. Spiekerman, G. Smestad, J. Kowalik, L. M. Tolbert, and M. Grätzel, Poly(4-undecyl-2,2'-bithiophene) as a hole conductor in solid state dye sensitized titanium dioxide solar cells, *synth. Met.*, 2001, 121, 1603-1604
- [73] M. P. T. Christiaans, M. M. Wienk, P. A. van Hal, J. M. Kroon and R. A. J. Janssen, Photoinduced electron transfer from conjugated polymers onto TiO₂, *Synth. Met.*, 1999, 101, 265-266
- [74] R. Memming, *Semiconductor Electrochemistry*, Wiley-CVH, 2001
- [75] C. O. Too, G. G. Wallace, A. K. Burrell, G. E. Collis, D. L. Officer, E. W. Boge, S. G. Brodie, E. J. Eavns, Photovoltaic cells based on polythiophenes and substituted polythiophenes, *Synth. Met.*, 2001, 123, 53 - 60
- [76] Y. G. Kim, J. Walker, L. A. Samuelson and J. Kumar, Efficient light harvesting polymers for nanocrystalline TiO₂ photovoltaic cells, *Nano Lett.*, 2003, 3 (4), 523-525
- [77] C. L. Huisman, A. Goossens, J. Schoonman, Preparation of a nanostructured composite of titanium dioxide and polythiophene: a new towards 3 D heterojunction solar cells, *Synth. Met.*, 2003, 138, 237-241
- [78] M. K. Nazeeruddin, A. Kay, I. Rodicio, R. Humphry-Baker, E. Mueller, P. Liska, N. Vlachopoulos, and M. Graetzel, Conversion of light to electricity by cis-X₂bis(2,2'-bipyridyl-4,4'-dicarboxylate)ruthenium(II) charge-transfer sensitizers (X = Cl-, Br-, I-, CN-

, and SCN-) on nanocrystalline titanium dioxide electrodes, *J. Am. Chem. Soc.*, 1993, 115, 6382-6390

[79] A. Galembeck and O. L. Alves, Planar heterostructures of oxide / conducting polymer (CuO/polypyrrole and CeO₂/polypyrrole), *Synth. Met.*, 1999, 102, 1238-1239

[80] R. Partch, S. G. Gangolli, E. Matijevic, W. Cai, and S. Arajs, Conducting polymer composites: I. Surface-induced polymerization of pyrrole on iron (III) and cerium (IV) oxide particles, *J. Colloid. Interfac. Sci.*, 1991, 144 (1), 27-35

[81] K. Suri, S. Annapoorni, R. P. Tandon, N. C. Mehra, Nanocomposite of polypyrrole-iron oxide by simultaneous gelation and polymerization, *Synth. Met.*, 2002, 126, 137-142

[82] K. Suri, S. Annapoorni and R. P. Tandon, Phase change induced by polypyrrole in iron-oxide polypyrrole nanocomposite, *Bull. Mater. Sci.*, 2001, 24 (6), 563-567

[83] A. D. Pasquier, F. Orsini, A. S. Gozdz, J.-M. Tarascon, Electrochemical behaviour of LiMn₂O₄-PPy composite cathodes in the 4-V region, *J. Power Sources*, 1999, 81-82, 607-611

[84] A. Yildiz, A. Sobczynski, A. J. Bard, A. Campion, M. A. Fox, T. E. Mallouk, S. E. Webber, and J. M. White, *Langmuir*, 1989, 5, 148-149

[85] M. Okano, K. Itoh, and A. Fujishima, Photoelectrochemical polymerization of pyrrole on TiO₂ and its application to conducting pattern generation, *J. Electrochem. Soc.*, 1987, 134 (4), 837-841

[86] Y. Hao, M. Yang, C. Yu, S. Cai, M. Liu, L. Fan, Y. Li, Photoelectrochemical studies on acid-doped polyaniline as sensitizer for TiO₂ nanoporous film, *Solar Energy Mater. & Solar Cells*, 1998, 56, 75-84

[87] K. Murakoshi, R. Kogure, Y. Wada, S. Yanagida, Fabrication of solid-state dye-sensitized TiO₂ solar cells combined with polypyrrole, *Solar Energy Mater. & Solar Cells*, 1998, 55, 113-125

[88] M. S. J. Gani, "Electrophoretic deposition – A review", *Industrial ceramics*, 14 (14), 1994, 164-174

[89] P. Sarkar, P. S. Nicholson, "Electrophoretic deposition (EPD): Mechanisms, Kinetics, and Application to ceramics", *J. Am. Ceram. Soc.*, 1996, 79 (8), 1987-2001

[90] A. R. Boccaccini, I. Zhitomirsky, "Application of electrophoretic and electrolytic deposition techniques in ceramic processing", *Current Opinion in solid state & materials science*, 2002, 6, 251-260

[91] O. O. Van der Biest, L. J. Vandeperre, "Electrophoretic deposition of materials", *Annu. Rev. Mater. Sci.*, 1999, 29, 327-352

-
- [92] F. Bouyer and A. Foissy, "Electrophoretic deposition of silicon carbide", *J. Am. Ceram. Soc.*, 1999, 82 (8), 2001-2010
- [93] P. Sarkar, S. Datta and P. S. Nicholson, "Functionally graded ceramic / ceramic and metal/ ceramic composites by electrophoretic deposition", *Composites Part B*, 1997, 28B, 49-56
- [94] J. Lyklema, "Principle of the stability of lyophobic colloidal dispersion in non-aqueous media", *Adv. Colloid. Interface Sci.*, 1968, 2(2), 67-114
- [95] P. C. Hiemenz, *Principles of colloidal and surface chemistry*, New York: Dekker, 1991
- [96] H. C. Hamaker and E. J. W. Vewey, "The role of the forces between the particles in electrodeposition and other phenomena", *Trans. Faraday Soc.*, 1940, 180-185
- [97] H. Koelmans and J. T. G. Overbeek, "Stability and electrophoretic deposition of suspensions in non-aqueous media", *Discuss. Faraday Soc.*, 1954, 18, 52-63
- [98] H. Koelmans, "Suspensions in non-aqueous media", *Philips Res. Rep.*, 1955, 10, 161-183
- [99] F. Grillon, D. Fayeulle and M. Jeandin, "Quantitative image analysis of electrophoretic coating", *J. Mater. Sci. Lett.*, 1992, 11, 272-275
- [100] M. Shimbo, K. Tanzawa, M. Miyakawa and T. Emoto, "Electrophoretic deposition of glass powder for passivation of high voltage transistors", *J. Electrochem. Soc.*, 1985, 132 (2), 393-398
- [101] J. Mizuguchi, K. Sumi and T. Muchi, "A highly stable nonaqueous suspension for the electrophoretic deposition of powder substances", *J. Electrochem. Soc.*, 1983, 130 (9), 1819-1825
- [102] M. Giersig and P. Mulvaney, "Formation of ordered two-dimensional gold colloid lattices by electrophoretic deposition", *J. Phys. Chem.*, 1993, 97, 6334-6336
- [103] S. Y. Zhao, S. B. Lei, S. H. Chen, H. Y. Ma, S. Y. Wang, "Assembly of two-dimensional ordered monolayers of nanoparticles by electrophoretic deposition", *Colloid. Polym. Sci.*, 2000, 278, 682-686
- [104] P. Sakar, O. Prakash and P. S. Nicholson, "Micro-laminate ceramic / ceramic composite (YSZ/Al₂O₃)", *Ceram. Eng. Sci. Proc.*, 1994, 15, 1019-1027
- [105] N. Koura, T. Tsukamoto, H. Shoji and T. Hotta, "Preparation of various oxide films by electrophoretic deposition method: A study of the mechanism", *Jpn. J. Appl. Phys.*, 1995, 34, 1643-1647

-
- [106] D. R. Brown, F. W. Salt, "The mechanism of electrophoretic deposition", *J. Appl. Chem.*, 1965, 15, 40-48
- [107] J. J. Siracuse, J. B. Talbot, E. Sluzky, K. R. Hesse, "The Adhesive Agent in Cathodically Coated Phosphor Screens", *J. Electrochem. Soc.*, 1990, 137 (1), 346-348
- [108] H. C. Hamaker, "Formation of deposition by electrophoresis", *Trans. Faraday Soc.*, 1940, 36, 279-287
- [109] A. Sussman and T. J. Ward, "Electrophoretic deposition of coatings from glass isopropanol slurries", *RCA Rev.*, 1981, 42, 178-197
- [110] Y. Hitara, A. Nishimoto and Y. Ishihara, "Forming of alumina powder by electrophoretic deposition", *J. Ceram. Soc. Jpn.*, 1991, 99, 108-113
- [111] Z. Zhang, H. Huang and Z. Jiang, "Electrophoretic deposition forming of SiC-TZP composites in nonaqueous sol media", *J. Am. Ceram. Soc.*, 1994, 77, 1946-1949
- [112] J. Will, M. K. M. Hruschka, L. Gubler and L. J. Gauckler, "Electrophoretic deposition of zirconia on porous anodic substrates", *J. Am. Ceram. Soc.*, 2001, 84(2), 328-332
- [113] Y. Fukada, N. Nagarajan, W. Mekky, Y. Bao, H. S. Kim, P. S. Nicholson, "Electrophoretic deposition – mechanisms, myths and materials", *J. Mater. Sci.*, 2004, 39, 787-801
- [114] C. Y. Chen, S. Y. Chen, D. M. Liu, "Electrophoretic deposition forming of porous alumina membranes", *Acta Mater.*, 1999, 47 (9), 2717-2726
- [115] R. Moreno, B. Ferrari, "Effect of the slurry properties on the homogeneity of alumina deposits obtained by aqueous electrophoretic deposition", *Mater. Res. Bull.*, 2000, 35, 887-897
- [116] F. Tang, T. Uchikoshi, K. Ozawa, Y. Sakka, "Electrophoretic deposition of aqueous nano- γ - Al_2O_3 suspensions", *Mater. Res. Bull.*, 2002, 37, 653-660
- [117] M. S. Lazic, K. Simovic, V. B. M. Stankovic, P. Jovanic and D. Kicevic, "The influence of the deposition parameters on the porosity", *J. Serb. Chem. Soc.*, 2004, 69 (3), 239-249
- [118] W. E. Windes, J. Zimmerman, I. E. Reimanis, "Electrophoretic deposition applied to thick metal-ceramic coatings", *Surface and Coatings Technology*, 2002, 157, 267-273
- [119] K. Simovic, V. B. Miskovic, D. Kicevic, P. Jovanic, "Electrophoretic deposition of thin alumina films from water suspension", *Colloids and surfaces A*, 2002, 209, 47-55

-
- [120] S. Put, J. Vleugels, G. Anne, O. Van der Biest, "Functionally graded ceramic and ceramic – metal composites shaped by electrophoretic deposition", *Colloids and surfaces A*, 2003, 222, 223-232
- [121] N. Dougami, T. Takada, "Modification of metal oxide semiconductor gas sensor by electrophoretic deposition", *Sensors and Actuators B*, 2003, 93, 316-320
- [122] Y. Masuda, T. Sugiyama, W. S. Seo and K. Kuomoto, "Deposition mechanism of anatase TiO₂ on shelf-assembled monolayers from an aqueous solution", *Chem. Mater.*, 2003, 15, 2469-2476
- [123] M. A. Nawi, L. C. Kean, K. Tanaka, M. S. Jab, "Fabrication of photocatalytic TiO₂-epoxidized natural rubber on Al plate via electrophoretic deposition", *Applied Catalysis B*, 2003, 46 (1), 165-174
- [124] F. Tang, T. Uchikoshi, T. S. Suzuki, Y. Sakka, "Alignment of TiO₂ particles by electrophoretic deposition", *Mater. Res. Bull.* 2004, 39, 2155-2161
- [125] F. Hosseinbabaei, B. Raissidehkordi, "Electrophoretic deposition of MgO thick films from an acetone suspension", *J. Eur. Ceram. Soc.*, 2000, 20, 2165-2168
- [126] B. Ferrari, R. Moreno, P. S. Nicholson, "Electrophoretic deposition of MgO from organic suspensions", *J. Europ. Ceram. Soc.*, 2000, 20, 99-106
- [127] F. Tang, Y. Sakka, T. Uchikoshi, "Electrophoretic deposition of aqueous nano-sized zinc oxide suspensions on a zinc electrode", *Mater. Res. Bull.*, 2003, 38, 207-212
- [128] K. Maca, H. Hadraba and J. Cihlar, "Electrophoretic deposition of alumina and zirconia. I. Single – component systems", *Ceram. Int.*, 2004, 30 (6), 843-851
- [129] N. Chandrasekhara and P. V. Kamat, "Assembling gold nanoparticles as nanostructured films using an electrophoretic approach", *Nano Lett.*, 2001, 1-2, 67-70
- [130] T. Tsubota, S. Ida, N. Okada, M. Nagata, Y. Matsumoto, N. Yatsushiro, "CVD diamond coating on WC-Co cutting tool using ECR MPCVD apparatus via electrophoretic seeding pretreatment", *Surface and Coatings Technology*, 2003, 169-170, 262-265
- [131] M. A. L. Nobre, R. H. R. Castro, D. Gouvea, "Engineering surface and electrophoretic deposition of SiC powder", *Mater. Lett.*, 2001, 50, 115-119
- [132] M. T. O. Petropoulou, A. F. Alzomailis, R. Argyropoulou, K. M. Ochsenkuehn, "Superconducting coatings of MgB₂ prepared by electrophoretic deposition", *Anal. Bioanl. Chem.*, 2004, 379, 792-795
- [133] E. W. Williams, "The electrophoresis of thin film CdS/Cu₂S solar cells", *Solar Cells*, 1980, 1 (4), 357-366

-
- [134] J. B. Talbot, E. Sluzky, S. K. Kurinec, "Electrophoretic deposition of monochrome and color phosphor screens for information displays", *J. Mater. Sci.*, 2004, 39, 771-778
- [135] E. Sluzky, K. Hesse, "Electrophoretic preparation of phosphor screen", *J. Electrochem. Soc.*, 1989, 136 (9), 2724-2727
- [136] K. Kanamura, J. Hamagami, "Innovation of novel functional material processing technique by using electrophoretic deposition process", *Solid State Ionics*, 2004, 172, 303-308
- [137] J. Li, Y. J. Wu, T. Yamamoto, M. Kuwabara, "Electrophoretic depositino and photoluminescent properties of Eu – doped BaTiO₃ thin film from a suspension of monodispersed nanocrystallites", *Sci. Tech. Adv. Mater.*, 2005, 5, 393 – 398
- [138] S. Okamura, T. Tsukamoto and N. Koura, "Fabrication of ferroelectric BaTiO₃ films by electrophoretic deposition", *Jpn. J. Appl. Phys.*, 1993, 32, 4182-4185
- [139] C. Song, G. Villemure, "Preparation of clay-modified electrodes by electrophoretic deposition of clay", *J. Electroanal. Chem.*, 1999, 462, 143-149
- [140] T. Seike, M. Matsuda, M. Miyake, "Fabrication of Y-type zeolite films by electrophoretic deposition", *Solid State Ionics*, 2002, 151, 123-127
- [141] W. G. Dorfeld and C. E. Young, "Thin glass dielectric films on anodized aluminum", *Thin Solid Films*, 1986, 143 (1), 53-61
- [142] C. Kaya, F. Kaya, A. R. Boccaccini, "Electrophoretic deposition infiltration of 2-D metal fibre-reinforced cordierite matrix composites of tubular shape", *J. Mater. Sci.*, 2002, 37, 4145-4153
- [143] J. Ma, C. Wang, K. W. Peng, "Electrophoretic deposition of porous hydroxyapatite scaffold", *Biomater.*, 2003, 24, 3505-3510
- [144] J. Ma, C. H. Liang, L. B. Kong, C. Wang, "Colloidal characterization and electrophoretic deposition of hydroxyapatite on titanium substrate", *J. Mater. Sci.*, 2003, 14, 797-801
- [145] I. Zhitomirsky, A. Petric, "Electrophoretic deposition of electrolyte materials for solid oxide fuel cells", *J. Mater. Sci.*, 2004, 39, 825-831
- [146] M. Allard, E. H. Sargent, P. C. Lewis and E. Kumacheva, "Colloidal crystals grown on patterned surfaces", *Adv. Mater.*, 2004, 16 (15), 1360-1364
- [147] C. Wang, J. Ma, W. Cheng, "Formation of polyetheretherketone polymer coating by electrophoretic deposition method", *Surface and Coatings Technology*, 2003, 173, 271-275

-
- [148] A. L. Rogach, N. A. Kotov, D. S. Koktysh, J. W. Ostrander, G. A. Ragoisha, "Electrophoretic Deposition of Latex-Based 3D Colloidal Photonic Crystals: A Technique for Rapid Production of High-Quality Opals", *Chem. Mater.*, 2000, 12 (9), 2721-2726
- [149] H. Qariouh, N. Raklaoui, R. Schue, F. Schue and C. Bailly, "Electrophoretic deposition of polyetherimide from aqueous emulsion: optimization of some deposition parameters", *Polym. Int.*, 1999, 48, 1183-1192
- [150] H. Qariouh, R. Schue, N. Raklaoui and F. Schue, "Preparation of polyetherimide / carbon fiber composites by a cataphoresis process", *Polym. Int.*, 1999, 48, 1065-1067
- [151] K. Tada and M. Onoda, "Nanostructured conjugated polymer films by electrophoretic deposition", *Adv. Funct. Mater.*, 2002, 12 (6-7), 420-424
- [152] K. Tada and M. Onoda, "Preparation and application of nanostructured conjugated polymer film by electrophoretic deposition", *Thin Solid Films*, 2003, 438 – 439, 365-368
- [153] K. Tada and M. Onoda, "Preparation of donor – acceptor nanocomposite through electrophoretic deposition", *Curr. Appl. Phys.*, 2005, 5 (1), 5-8
- [154] S. Barazzouk, S. Hotchandani and P. V. Kamat, "Nanostructured fullerene films", *Adv. Mater.*, 2001, 13 (21), 1614-1617
- [155] N. K. Shrestha, K. Sakarada, M. Masuko and T. Saji, "Composite coatings of nickel and ceramic particles prepared in two steps", *Surface and Coatings Technology*, 2001, 140 (2), 175-181
- [156] J. Zhang, B. I. Lee, "Electrophoretic deposition and characterization of micrometer-scale BaTiO₃ based X7R dielectric thick films", *J. Am. Ceram. Soc.*, 2000, 83, 2417-2422
- [157] A. R. Boccaccini, H. G. Krueger, U. Schinlder, "Ceramic coatings on carbon and metallic fibres by electrophoretic deposition", *Mater. Lett.*, 2001, 51, 225-230
- [158] I. Zhitomirsky, "Electrophoretic hydroxyapatite coatings and fibres", *Mater. Lett.*, 2000, 42, 262-271
- [159] A. R. Boccaccini, C. Kaya, K. K. Chawla, "Use of electrophoretic deposition in the processing of fibre reinforced ceramic and glass matrix composites: a review", *Composites A*, 2001, 32, 997-1006
- [160] C. Kaya, Kaya F, A. R. Boccaccini, K. K. Chawla, "Fabrication and characterisation of Ni-coated carbon fibre – reinforced alumina ceramic matrix composites using electrophoretic deposition", *Acta Mater.*, 2001, 49, 1189-1197
- [161] C. Kaya, A. R. Boccaccini, K. K. Chawla, "Electrophoretic deposition forming of Ni-coated carbon fibre-reinforced borosilicate glass matrix composites", *J. Am. Ceram. Soc.*, 2000, 83, 1885-1888

-
- [162] K. Maca, H. Hadraba and J. Cihlar, "Electrophoretic deposition of alumina and zirconia: II. Two-component systems", *Ceram. Int.*, 2004, 30 (6), 853-86
- [163] H. O. Finklea, *Semiconductor Electrodes*, Elsevier, 1988
- [164] N. Sato, *Electrochemistry at Metal and Semiconductor Electrodes*, Elsevier, 1998
- [165] R. Enderlein, N. J. M. Horing, *Fundamentals of semiconductor physics and devices*, World Scientific, 1997
- [166] S. Licht, *Encyclopedia of electrochemistry 6: Semiconductor electrodes and photoelectrochemistry*, 2002
- [167] A. J. Bard and L. R. Faulkner, *Electrochemical methods: Fundamentals and applications*, Wiley, 1980
- [168] R. Memming, *Semiconductor electrochemistry*, Wiley, 2001
- [169] W. Plieth and N. Hebestreit, German Patent Application No. 19919261.8
- [170] H. Lee, H. Yang, J. Kwak, Mass transport behaviour of polypyrrole and poly (N-methylpyrrole) films in acetonitrile solutions, *J. Electroanal. Chem.*, 468 (1999) 104-109
- [171] N. Myung, A study on the electrodeposition of NiFe alloy thin films using chronocoulometry and electrochemical quartz crystal microgravimetry, *Bull. Korean Chem. Soc.* 9 (2001) 994-998
- [172] D. A. Buttry, M. D. Ward, Measurement of interface processes at electrode surfaces with the electrochemical quartz crystal microbalance, *Chem. Rev.* 92 (1992) 1355-1379
- [173] H. Schwarze, K. Wolschendorf, Der Lock-in Verstärker in der Laborpraxis, *GIT Fachz. Lab.* 18, 1974, 968-973
- [174] I. Rubinstein, *Physical Electrochemistry*, Marcel Dekker, Inc., 1995
- [175] E. Gileadi, *Electrode kinetics for chemists, chemical engineers and materials scientists*, VCH, 1993
- [176] G. Shi, J. Xu and M. Fu, Raman spectroscopic and electrochemical studies on the doping level changes of polythiophene films during their electrochemical growth processes, *J. Phys. Chem. B*, 2002, 106 (2), 288 - 292
- [177] Axel Fikus, PhD thesis, TU Dresden 1999
- [178] P. M. Biesheuvel and H. Verweij, Theory of cast formation in electrophoretic deposition, *J. Am. Ceram. Soc.*, 82 (6) (1999) 1451-1455
- [179] J. Lyklema, Principles of the stability of lyophobic colloidal dispersions in non-aqueous media, *Adv. Colloidal Interface Sci.* 2 (2), (1968) 67-114
- [180] P. Sarkar, P. S. Nicholson, Electrophoretic deposition (EDP): Mechanism, kinetics and application to ceramics, *J. Am. Ceram. Soc.* 79 (8) (1996) 1987-2002

-
- [181] J. Pflieger, M. Pavlik, N. Hebestreit, W. Plieth, Photosensitive layers of TiO₂ / polythiophene composites prepared by electrophoretic deposition, *Macromolecular Symposia*, 2004, 212 (1), 539-548
- [182] M. Martini, M.-A. De Paoli, Photoelectrochemical response and differential capacitance of poly(3-methylthiophene), *Solar Energy Material & Solar Cells*, 2000, 60 (1), 27 - 41
- [183] M. Martini, M.-A. De Paoli, Photoelectrochemical response and differential capacitance of poly(3-methylthiophene), *Solar Energy Material & Solar Cells*, 2000, 60 (1), 27 - 41
- [184] D. Wöhrle and D. Meissner, Organic solar cells, *Adv. Mater.*, 1991, 3, 129 - 138
- [185] P. R. Somani, R. Marimuthu, U. P. Mulik, S. R. Sainkar, D. P. Amalnerkar, High piezoresistivity and its origin in conducting polyaniline / TiO₂ composites, *Synth. Met.*, 1999, 106, 45 - 52
- [186] N. B. Hannay, *Semiconductors*, Chapman & Hall, London, 1959
- [187] N. Brutscher and M. Hoheisel, Schottky diodes with high series resistance: A simple method of determining the barrier heights, *Solid state electronics*, 1988, 31 (1), 87 - 89
- [188] X. D. Dang, C. M. Intelmann, U. Rammelt, W. Plieth, Copolymer electrosynthesis of ethyl-3-thiophene acetate and 3-methylthiophene and characterization of the resulting copolymers by spectroscopic studies, *J. Solid State Electrochem.*, 2005, in press
- [189] M. A. Sato, S. Tanada and K. K. Ama, Electrochemical preparation of conducting poly (3-methylthiophene): comparison with polythiophene and poly (3-methylthiophene), *Synth. Met.*, 1986, 14, 279 – 288



Versicherung

Hiermit versichere ich, dass ich die vorliegende Arbeit ohne unzulässige Hilfe Dritter und ohne Benutzung anderer als der angegebenen Hilfsmittel angefertigt habe; die aus fremden Quellen direkt oder indirekt übernommenen Gedanken sind als solche kenntlich gemacht. Die Arbeit wurde bisher weder im Inland noch im Ausland in gleicher oder ähnlicher Form einer anderen Prüfungsbehörde vorgelegt.

Dresden, den 16.01.2006

Vu, Quoc Trung

Erklärung

Die vorliegende Arbeit wurde unter der wissenschaftlichen Betreuung von Prof. Waldfried Plieth, Dr. Ursula Rammelt und Dr. Jiri Pflieger in der Zeit von Okt. 2002 bis Jan. 2006 im Institut für Physikalische Chemie in Elektrochemie der Technischen Universität Dresden angefertigt. Es haben keine frühen erfolglosen Promotionsverfahren stattgefunden.

Ich erkenne die Promotionsordnung der Fakultät Mathematik und Naturwissenschaften der Technischen Universität Dresden vom 16.04.2003 in vollem Umfang an.

Dresden, den 16. 01. 2006

Vu, Quoc Trung